Tungsten Recrystallization Behavior Under Steady and Transient Hydrogen Plasma Loading

Jorge Andrés Rosas Saad

Thesis

submitted in partial fulfillment of the requirements for the degree of

Master of Science

in the department of

Materials Science and Engineering

at the

Faculty of Mechanical, Maritime and Materials Engineering

of

Delft University of Technology

Department of Materials Science and Engineering
Faculty of Mechanical, Maritime and Materials Engineering
Delft University of Technology
Delft, The Netherlands

Author:	Jorge Andrés Rosas Saad
Student Number:	4628071
Date:	August 30, 2018

Thesis Committee:

Chair:	Prof. Dr. Ir J. Sietsma	Faculty 3mE, TU Delft
Committee Member:	Dr. T.W. Morgan	Gp. Leader PMI, DIFFER
Committee Member:	Dr. M.H.F. Sluiter	Faculty 3mE, TU Delft
Committee Member:	Dr. A.J. Böttger	Faculty 3mE, TU Delft

Abstract

Because of its extraordinary material properties, like its high melting point and thermal stress resistance, low erosion and swelling rate, and high radiation damage resistance, highly deformed pure tungsten has been chosen as the plasma facing surface material for the ITER reactor divertor. The study of tungsten's recrystallization behavior and damage response during operation conditions is thus important because the divertor will have to withstand high heat fluxes and temperatures during service which induce recrystallization. This phenomena alters the microstructure of the material, inducing degradation in its properties, like loss in mechanical strength and embrittlement making it prone to large plastic deformation, surface roughening, crack networks formation and propagation. Understanding this behavior under the ITER reactor operation circumstances is paramount for the success of the reactor.

The aim of this project was to test regimes simulating steady state operation and high frequency and temperature transient pulses called ELMs (Edge Localized Modes) striking the divertor. Recent research has shown that the degradation and behavior of tungsten under these transient conditions does not consistently follow the expected parameters characterized in the literature. According to it, recrystallization, grain growth, and crack formation seem to be suppressed by the plasma loading under these regimes, thus a new understanding of the material behavior for these circumstances must be developed. To do this, ITER grade tungsten samples were subjected to a hydrogen plasma beam at DIFFER's Magnum-PSI with temperatures at the strike point ranging from ~1000 to ~1500 °C and high frequency pulses that increased the surface temperature by ~200 to ~300 °C above the steady state temperature. The surface thermal shock response to the plasma pulses was characterized by means of infrared and pyrometer readings at the samples' surface during exposure. Temperature and power density calculations were correlated with identified damage morphologies on the targets and a damage map for the experiments was elaborated, which showed that the most severe damage (cracks and crack networks) begin to appear in the range of the measured recrystallization temperature of the samples, which was lower than expected.

Using Vickers hardness, the recovery and recrystallization kinetics of the material were characterized by means of logarithmic decay and a modified version of JMAK recrystallization kinetics that includes an incubation time for the onset of recrystallization. Recrystallization kinetics were found to accelerate as the hydrogen exposure progresses, thus yielding lower effective activation energies for recrystallization when comparing furnace one hour exposures, plasma one hour exposures, and plasma four hour exposures. This pointed to the presence of hydrogen actively reducing the activation energy for self-diffusion. Simulations of hydrogen diffusion were performed to test this hypothesis, and even though the total concentration is low, given that the high experimental temperature does not permit trapping of the hydrogen, the diffusing atoms may still play a role in accelerating the recrystallization kinetics.

Based on the results of this research, it is proposed that interstitially diffusing hydrogen segregating to voids or grain boundaries is modifying the behavior of surrounding tungsten crystal lattice. Specifically, the mobility of the grain boundaries may be increasing because the hydrogen's presence would be promoting the creation of ledges in the grain boundary resulting in an overall free energy reduction for grain boundary diffusion. This localized defect formation would require a lower concentration of hydrogen than that required for solute drag or other suppression mechanisms, and might be mechanism behind the behavior observed in this work's experiments.

Acknowledgements

This thesis marks the culmination of the past two year studies fulfilling the requirements for my degree in Materials Science and Engineering at Delft University of Technology. It was an extraordinary experience that would not have been possible without the aid of so many people.

I would specially like to thank my supervisor Jilt Sietsma at TU Delft, who provided immeasurable assistance every step of the way. Your lectures were a vital stepping stone during my studies to become a material scientist, and as mentor during my thesis, your guidance and academic support helped shape this work which marks this milestone. I cannot be grateful enough for believing in my competencies and providing me with the opportunity to begin my internship as a researcher at DIFFER in Eindhoven.

In the same vein, I want to extend my gratitude to Thomas Morgan and Marco de Baar at DIFFER, who trusted in my capabilities and sponsored my research project as part of a year-long internship at the institute. I am particularly grateful for Tom's guidance and patience as the project progressed, for his keen guidance on the science when needed, and for his practical and on point advice on performing as scientist. I cannot apologize enough for taking too long to get to the point in our conversations.

I am grateful to all the researchers, students and staff at DIFFER, who supported me in my day to day over the past year, and bore with me as I learned the inner workings of plasma physics research and always had a spare moment to provide a helping hand. A special mention goes to my colleague Jun Wang, who provided so many fruitful insights as well as candid conversations during our stint sharing and office. Thank you so much for sparing some time helping me run my hydrogen concentration simulations on TMAP7 even though you had your hands full on your own research. I wish you nothing but success in your promising career.

So many people across different places were vital for me to be able to fully conduct my research. Special thanks to Thorsten Loewenhoff for providing the framework for this thesis's work, as well as for welcoming me with his team at FZJ in Germany and supporting in taking all the necessary measurements I requested at their institute. A special mention needs to rightly go to Sander van Asperen and Elise Reinton at TU Delft who provided so much assistance during the data gathering at the university lab, even if I gave such a short notice on my requests. I must also express my gratitude towards Jesús Ortiz and Miguel Panizo at UPM Madrid, whose disposition to aid a struggling and unknown colleague should be a standard for professional interaction in any field.

Finally, would like to thank my parents, Lizette and Jorge, and my sister Valentina for their support in all my academic, professional and personal endeavors, and my girlfriend Alethia, who has been my ground to stand on and my support throughout this adventure.

Siti, Tata, Yido, this one is for you.

Table of Contents

1. Introduction

As fusion energy research matures, and the construction of the largest experimental reactor to date (ITER) comes to fruition, the scientific and engineering challenges posed by this endeavor need to be addressed and resolved. Fusion as an energy source holds the promise of virtually limitless and environmentally responsible power generation, but this is subordinated to all technical challenges along the way being successfully cleared. Since the reactor environment is teeming with extreme conditions where most materials have not been extensively tested, there exist gaps in the collective scientific and engineering knowledge on how these materials, tasked with enduring high magnetic fields, temperature gradients and energetic plasma discharges, will behave under these regimes. Understanding and characterizing these behaviors is of paramount importance for the successful deployment of the reactor.

The scope of this research was to address the issue of the material behavior of one specific component, the Divertor, specifically the recrystallization and damage response of the strike zone built out of tungsten (W). For this aim, samples representative of the material to be used in the ITER reactor were subjected to regimes simulating instances where the reactor's plasma strikes the Divertor transiently at high temperatures and frequencies called Edge Localized Modes (ELMs). Previous research has shown that the degradation and behavior of the tungsten under these conditions does not consistently follow the expected metrics characterized in the literature, and thus a new understanding of the material properties for these circumstances must be developed. In order to fully capture and identify the effects of the plasma on the material, samples were tested under plasma loading at DIFFER and used to extend the current body of knowledge.

Early research by Loewenhoff et al. [1] has shown that recrystallization and grain growth seem to be suppressed by the plasma loading under these simulated ELMs regimes, when compared to equivalent loadings that did not involve plasma exposure (laser, neutrals, electrons, etc.…). The objective of this project thus focused on explaining this behavior from a materials science point of view, and to provide insight into why and how the components will fare under ITER operational conditions. This was done by mapping the subjected temperature and energy inputs on the samples, and comparing the thermal response of the material over time, as well as characterizing the material damage morphologies and material properties changes that arise during the exposures. When compared to the equivalent non-plasma loaded samples, the effect of hydrogen plasma particles on tungsten is made evident, and conclusions on the nature of this shift in recrystallization behavior are made.

2. Background

2.1 Societal Context

Per capita electricity consumption around the world is steadily growing, with global electricity demand expected to double between the 2020's and 2030's and to triple between the 2050's and 2100's [2][3]. Fossil fuels have been the planet's major source of energy for the past century, but in spite of the global developments that this increased use in energy has fostered, the use of these non-renewable sources has also led to important environmental challenges like significant global warming due to greenhouse gas emissions, deforestation and acid rain, increased air pollution (both in pollutants' concentration and toxicity), among others [3]. In addition to this, the world's coal, oil and gas reserves, are estimated to have a remaining capacity of less than two hundred years [2][3].

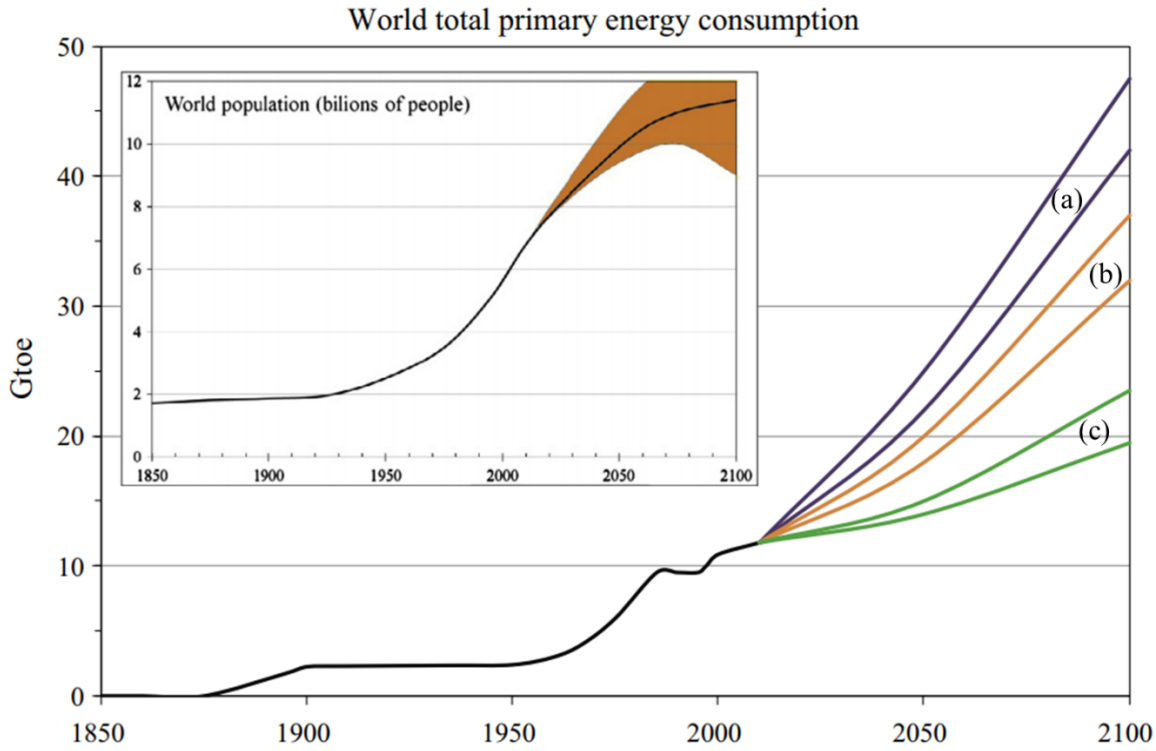

Figure 1. Global energy consumption in gigatonnes of oil equivalent (Gtoe) with upper and lower bounds projected for a) rapid economic growth and high technological development, b) economic growth and intermediate technological development and c) environmental constrains. Inset: Global population growth projection [3].

A cog in the most recent generation of energy production, fission based nuclear power, has faced opposition since its inception in the mid-20th century due to concerns of weaponization and proliferation of its raw fuel and subsequent radioactive hazardous waste disposal and the potential for catastrophic disasters and meltdowns. This has moved the current trend of energy generation research towards alternative clean energy sources, with wind and solar power being the most widely studied. These renewable sources are the fastest growing energy sources today [4], but both still face challenges to meet the energy demand that is currently being fulfilled by

oil, gas and coal. Renewables still lack a significant technological level in terms of energy density, storage, efficiency and production costs, which makes them unsuitable as viable alternative for complete energy dependency. Furthermore, with increased decarbonization of the energy sector it becomes progressively harder for renewables to continue increasing their share in the energy capacity mix [4][5]. The above hurdles have made nuclear fusion energy production a promising alternative candidate for solving the next generation's energy needs. Fusion energy is arguably the source with the highest energy density available with our current technological understanding; energy storage is a non-issue for it, as a fusion reactor would be connected to the grid and energy would be produced and supplied on demand in a similar fashion as current fossil fuel or nuclear fission plants. Moreover, safety concerns that plague the fission generation technologies do not apply to fusion reactors, since due to their nature, they cannot undergo a meltdown reaction, and cannot be feasibly weaponized by hostile entities [2]. Based on progress over more than five decades in the nuclear fusion field, ITER, the first experimental nuclear fusion reactor expected to produce net energy [6], is currently under construction. Its aim is to provide proof of concept for a full sized nuclear fusion power plant that would provide clean energy controllably and reliably, thus leading the path of energy generation away from fossil fuels and into a future dominated by renewable and efficient energy production [2].

2.2 Magnetically Confined Fusion

Nuclear fusion is the physical process that leads to energy release within stars. In the sun, for instance, the nuclei of the elements hydrogen (H) and to a lesser extent helium (He) are brought into enough proximity due to the star's enormous gravitational pull, which also leads to a high pressure inside the star. Because of this, through quantum tunneling the nuclei overcome the electrostatic repulsive force between them in favor of the attractive strong nuclear force, which fuses them. This fusion of two light nuclei yields a heavier nucleus with slightly less mass than the parent one, with this "missing" mass being released as energy through the mass-energy equivalence. As an example, during the fusion of a deuterium (D) and tritium (T) pair (H isotopes) into He, the energy release of the reaction is of 17.6 MeV, but to achieve this D-T fusion, temperatures in the order of ~10 keV (~100 million °C) are generally needed efficiently produce the desired reaction [2]. To achieve fusion in a reactor the following conditions must be met: very high temperatures (on the order of 150 million °C for magnetic confinement fusion), high plasma particle density that increases the likelihood that collisions and thus fusion, occur, and an extended confinement and burning time holding the plasma within the containment volume [2][7].

Reaching the conditions mentioned above ensures that the fuel intended for fusion reaches a plasma state. Under these conditions, due to the high energy involved, a sizable fraction of the atoms are stripped of their electrons, becoming ionized. In this state of matter, the sum of the electron and ion charges is zero, so charge neutrality is conserved at a macroscopic scale. Inside the plasma, as charged particles move forming an electric current, they interact through the Coulomb force, and magnetic fields form due to the Lorentz interaction. This complex system results in collective long range interactions among the plasma particles which lead to instabilities and wave phenomena that are characteristic of this type of high energy, ionized and charge neutral plasma. [8]

Uncontrolled nuclear fusion reactions, in the form of thermonuclear explosions have been achieved artificially since the 1950s; nevertheless research to obtain controlled nuclear fusion for electricity or otherwise useful energy production remains ongoing. Although several

approaches are under different stages of investigation, the most widely developed is the magnetic confinement of plasma in a tokamak configuration reactor. Magnetic confinement takes advantage of the electromagnetic properties of the charged particles that make up the plasma and attempts to force them to flow along specific magnetic field lines, confining them inside a "magnetic bottle" [2].

2.3 Tokamak

Inside a tokamak (a Russian acronym meaning a toroidal chamber with magnetic coils) the plasma is forced into a toroidal or doughnut-like shape inside a vacuum chamber. This is accomplished by a series of magnetic coils circling around a central axis forming a torus. This toroidal magnetic field is, however, not enough to confine the plasma, as it encourages electrons and ions to drift apart, thus ending the plasma. To prevent this charge separation, a central solenoid is installed. This induces an electric current through the torus by means of transformer action, which in turn creates a magnetic field component around the minor cross-section of the torus (the poloidal direction). The resultant combination of these magnetic fields is a spiraling magnetic field around the torus which confines the plasma as it flows along these magnetic force lines. Additionally, this configuration still allows radial expansion of the plasma, so a last set of poloidal field coils is needed to achieve radial equilibrium of the plasma [2]. These configurations and the magnetic and electric interactions of a typical tokamak are depicted in Figure 1.

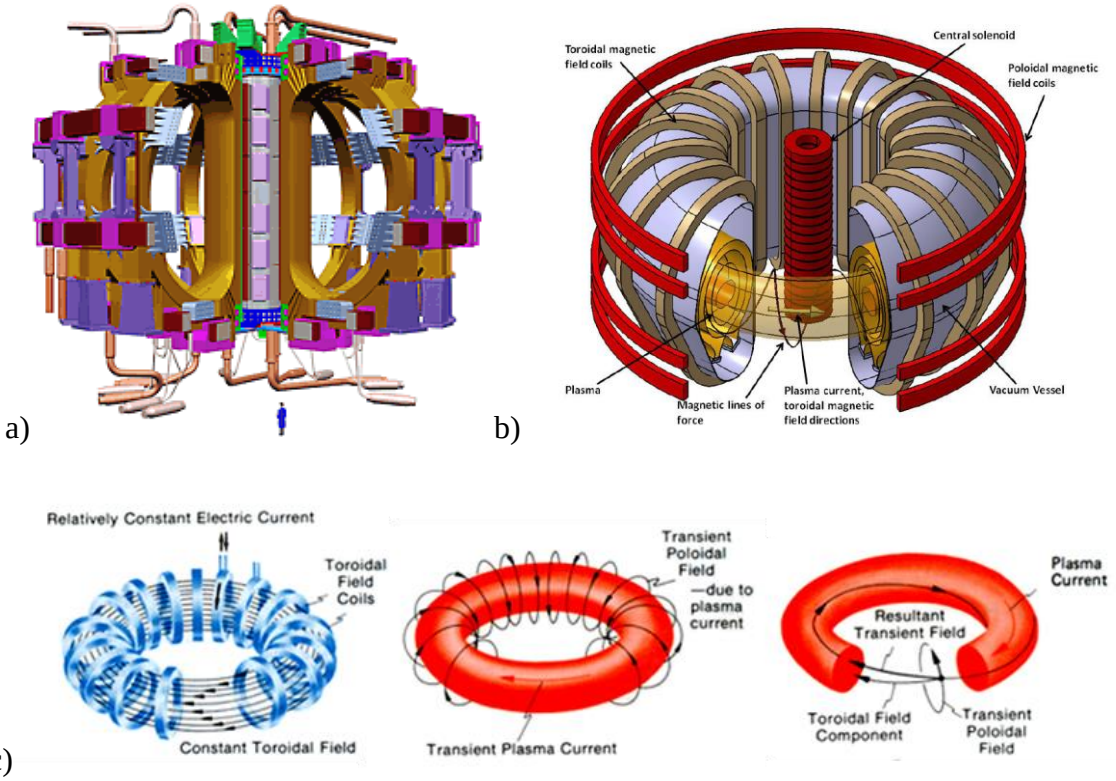

Figure 2. a) ITER Tokamak representation with accompanying human figure for scale, b) schematics of solenoids inside a tokamak configuration [2]*, and b) resultant of toroidal and poloidal magnetic field components of a tokamak* [9].

2.4 ITER

The ITER Organization (IO) is currently constructing the first experimental facility for an operational D-T fusion power generating reactor. The ITER reactor is currently under construction in Cadarache, France as a joint endeavor between the European Union, the United States, Russia, Japan, India, South Korea and China [10]. Its aim is to demonstrate the technical feasibility of fusion as energy source. The ITER reactor will also test the integration and implementation of experimental technologies (heating, control, diagnostics, cryogenics, etc...) for fusion devices looking towards future fusion power plant implementations [7].

The reactor is predicted to have an output of 10 times (Q = 10) the design energy input of 50 MW. This would be achieved during a sustained plasma burn, meaning a plasma where the heat from the fusion reaction is confined within the plasma efficiently enough for it to contribute significantly in sustaining the fusion reaction for 300 – 500 seconds. Even though ITER's goal is to demonstrate the use of nuclear fusion as a mean to produce useful energy, it will not use the energy produced to generate electricity. The heat produced will be absorbed by water-cooled walls, and the data obtained from the reactor's operation will be used to design the systems that would ultimately generate electricity by means of turbines and alternators in future fusion power plants with the DEMO reactor being the first one scheduled in the future. The ITER reactor facility is expected to be finished by 2025; with the first plasma being reached the following year and full D-T fusion operation is expected by 2035 [7].

2.5 Dutch Institute for Fundamental Energy Research

The Dutch Institute for Fundamental Energy Research (DIFFER), as part of NWO (Dutch acronym for Netherlands Organization for Scientific Research) champions fundamental scientific research into new and improved energy technology. Its research centers in fusion energy and solar fuels, with the aim of accelerating the transition to sustainable energy sourcing and consumption. DIFFER, as part of Eurofusion and Euratom, is the leading Dutch research center for nuclear fusion and the main contact point in The Netherlands for involvement in worldwide research into nuclear fusion.

To test plasma facing components intended for ITER, plasma linear devices able to produce ITER relevant plasma regimes are needed. For this purpose, the Magnum-PSI (MAgnetized plasma Generator and NUMerical modeling for Plasma Surface Interactions) was designed and built at DIFFER. Figure 2 shows the Magnum-PSI device with its building components [11].

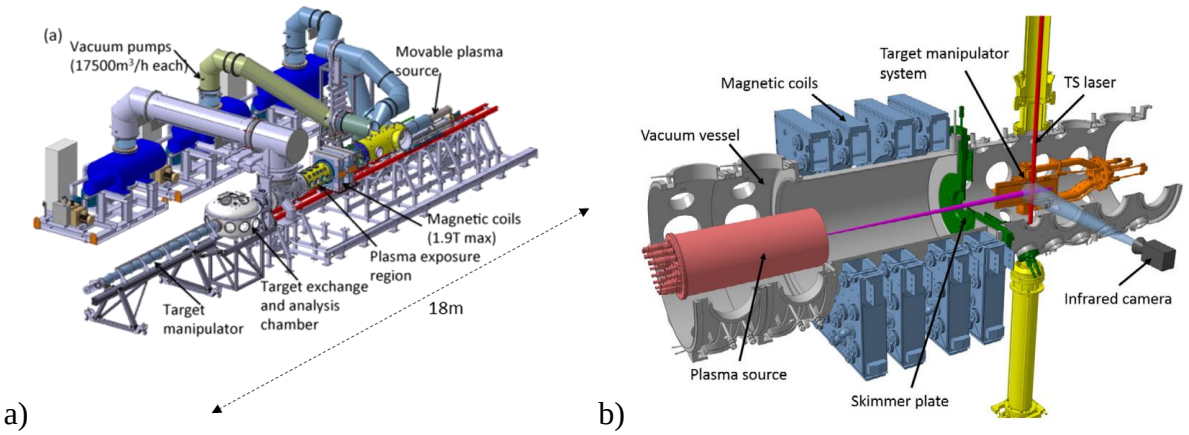

Figure 3. a) Schematic of Magnum-PSI and b) cross-section of plasma exposed region [11]

Magnum-PSI can produce a quasi-steady-state axial magnetic field up to 2.5 T to confine a high density plasma beam and direct it on a target which can be rotated to vary the angle of incidence of the plasma. Magnum-PSI can produce and sustain argon, hydrogen, helium, deuterium, tritium and neon plasmas that strike the target with a Gaussian heat and particle distribution profile typically 1-3 cm wide, enabling the study of different temperature and energy regimes around the strike zone [11].

2.6 Forschungszentrum Jülich

Forschungszentrum Jülich (FZJ) is one of Germany's main interdisciplinary research institutes. Like DIFFER, it is part of EURATOM, and carries out part of Germany's fusion research through its Nuclear Physics Institute; only one of many research facilities diversifying along different disciplines like biological sciences, climate research, neutron science, among others. FZJ prides itself in being experts on plasma-wall interactions, with their expertise lying on developing measuring techniques for ITER and DEMO relevant parameters such as temperatures, densities and magnetic fields as well as on impurities inside the plasma, with their main areas of focus being the vacuum vessel lining and the divertor. Located in the Nordrhein-Westfalen region, less than 120 km from DIFFER in Eindhoven; both institutes collaborate in fusion research due to their intersecting objectives, mainly those regarding ITER's divertor [12].

2.7 Plasma Wall Interactions

The generation of power through fusion results in high heat loads on the walls of the vacuum and plasma containing device. Aside from issues of wear, reliability and maintenance, if erosion from the wall enters the hot plasma in the reactor, it will decrease the fusion power output (cool the plasma). Moreover, the plasma can damage the first wall components, making them structurally unstable and unusable, as well as creating a safety hazard [13]. For these reasons it is critical that the plasma facing materials should be damage resistant under operational conditions.

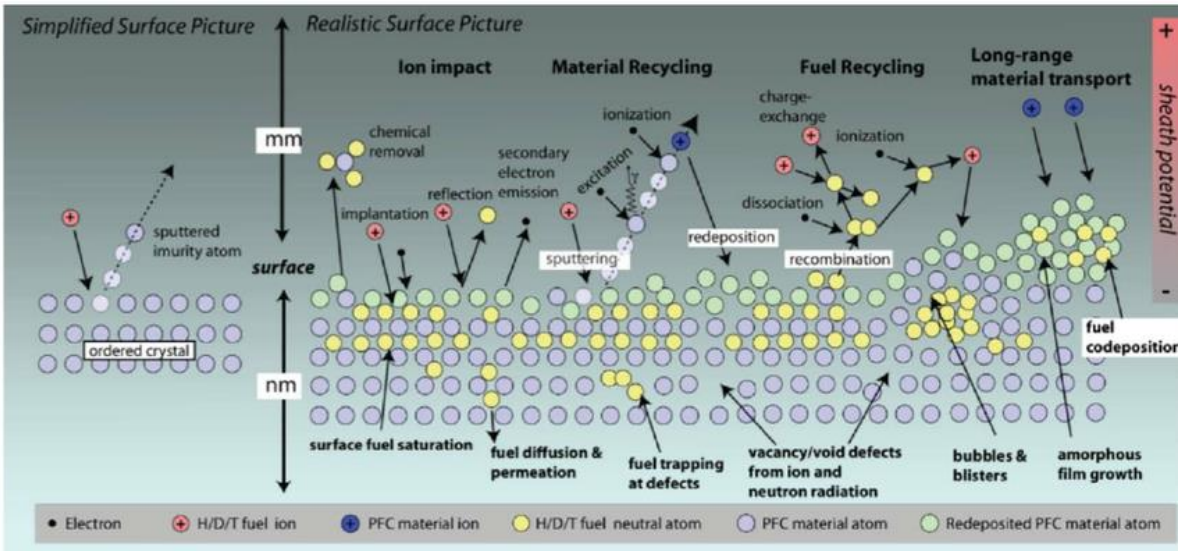

Figure 4. Selection of possible processes in plasma-material interactions. Through several different mechanisms, ions from the plasma (termed fuel in the figure) can penetrate the first wall surface and interact with the bulk. These interactions can release neutral atoms or ions from the surface into the plasma, cooling it down. [14]

Inside the confined plasma the heat generated by the fusion reaction diffuses out radially. Then, when it crosses the outermost closed flux magnetic surface it starts to flow along open field lines in a thin layer, called the scrape-off layer (SOL) as seen in Figure 5a. One of the plasma facing components (PFCs), the tokamak's divertor, is located across these open magnetic field lines, in the path created by the SOL (Figure 5b) [13].

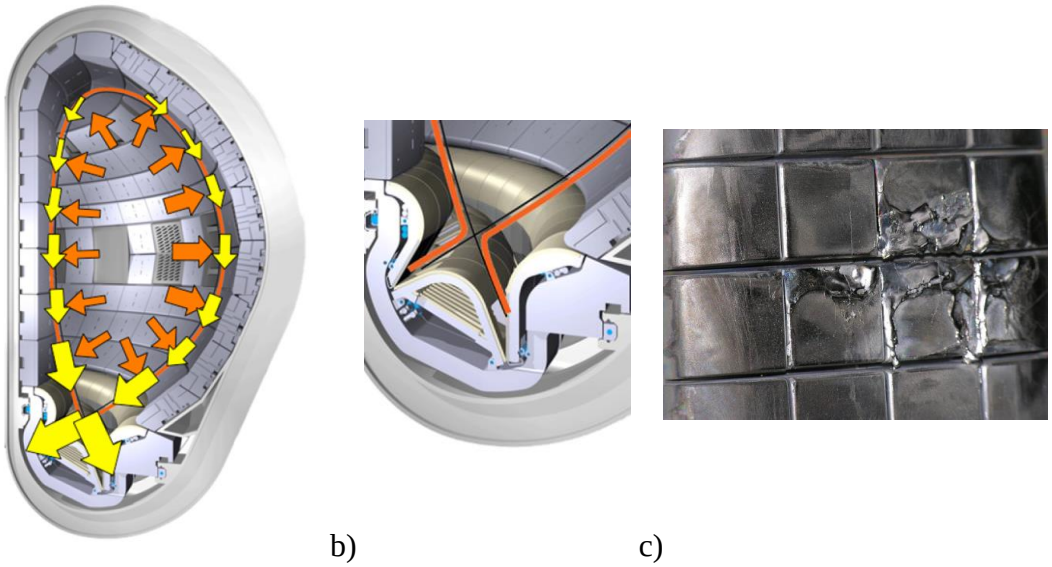

a) b) c)

Figure 5. a) Radial heat diffusion path (orange arrows) and flow along the SOL (yellow arrows). b) Strike point of SOL on divertor plates. c) Plasma induced damage on the divertor plate of the Alcator C-Mod tokamak (square tiles shown have an 80 mm side length). [13]

2.8 Divertor

The reactor divertor's purpose is to intercept the ionized impurities that flow along the SOL, and prevent them from re-entering and cooling and diluting the plasma, and to remove the waste heat from the reaction given by the alpha-particles as well as from the input from the heating sources [15]. These particles include erosion debris from the wall components and helium nuclei (ash), among other fusion products. When they hit the divertor plates, the heat is transferred to the fluid that cools the component, and the particles themselves are pumped out of the system, acting as an exhaust channel to prevent plasma contamination [13].

The parallel heat flux density entering upstream in the SOL is around 1 GW m^{-2}, which would then be deposited on a small section of the target. These are conditions that no material can reasonably withstand (refer to Figure 5c) without an effective reduction of energy influx, which is achieved mainly by means of tilting the target to expand the strike zone area, magnetic flux expansion, and by inducing line radiation along the SOL before it reaches the target. Additionally a process called detachment is induced which starts to recombine the plasma and leads to further power reductions to the surface [13]. As a result of these reductions, the perpendicular heat flux density at the divertor surface ends up being up to ~10 MW m^{-2} with an electron temperature of 1 – 5 eV and an electron density of ~10^{20} – 10^{21} m^{-3}. These are still very challenging conditions. Furthermore, instabilities in the plasma edge called edge localized modes (ELMs), can deposit ~2 – 4 GW m^{-2} for 0.5 – 1 ms on the divertor strike zones, as well as increasing the flux density hundred-fold [11].

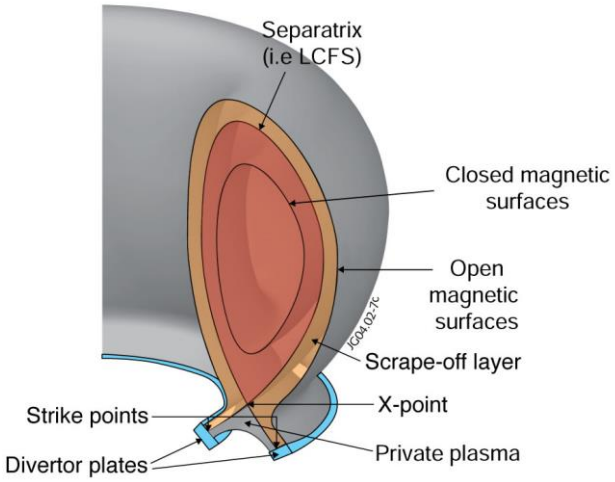

Figure 6. Schematic of the magnetic field surfaces and the divertor area [6]

The superposition of these ELM loads, with the steady state loading of the plasma hitting the divertor target, leads to intense and extremely localized heat spike zones which the material it is made of must withstand [1].

3. Materials Science Considerations

3.1 Tungsten as Divertor Material

Based on the mentioned conditions that the divertor will be subjected to, the requirements that the construction material must meet are very strict. It must have high thermal conductivity to dissipate the heat towards the cooling fluid [10], low sputtering yield to prevent plasma contamination, good thermo-mechanical properties (especially strength and ductility) to resist the thermal and mechanical stresses associated with operating at fusion inducing temperatures, resilience to thermal shock because of the high thermal gradients and cyclical loading expected, and resistance to radiation damage and neutron bombardment from the fusion products [16].

Taking into account the material requirements for the ITER reactor divertor, tungsten (W) has been chosen as the material for the plasma facing surface of the component. This is because of W's unique properties, mainly its high melting point, high energy threshold for sputtering yielding a low erosion rate, high thermal stress resistance, high thermal conductivity, low swelling, relative chemical inertness, low tritium retention and high radiation damage resistance [16]. These and other material properties are summarized in Table 1.

W Properties	
Atomic Number	74
Atomic Weight [amu]	183.85
Crystal Structure	bcc
Density [kg m^{-3}]	1925
Thermal Conductivity [W m^{-1} K^{-1}]	183
Thermal Expansion Coefficient [K-1]	4.6×10^{-6}
Melting Point [K]	3680
Boiling Point [K]	6000
Vapor Pressure at Melting Point [GPa]	13
Hardness [HV30]	>410
Melting Point [°C]	3422
Young's Modulus [GPa]	411
Stacking Fault Energy [J m^{-2}]	3.68
Dislocation Density [m^{-2}]	4.6×10^{16}

Table 1. ITER grade tungsten material properties at room temperature [16]

The use of tungsten does not come without issues. Pure tungsten (99.94%wt at least) is needed to retain the stated properties, since tungsten alloys are not a feasible option to use because diffusion kinetics at high temperature may induce diluted impurities to segregate to grain boundaries, creating new phases and weakening the structure [10]. Oxide and carbide dispersion is also undesirable, since they embrittle the tungsten. However, pure tungsten has its own disadvantages that need to be dealt with for the operation of the divertor, including its high atomic number, which increase the plasmas density if it enters it and thus cools it more easily than lighter elements, a poor machinability and high ductile-to-brittle transition temperature (DBTT). The divertor target area is built with small tiles because of the high mismatch between its coefficient of thermal expansion with the ones of heat sink's materials,

and the high thermal gradients expected which can cause uneven thermal stresses and expansion between regions of the component [10].

The study of tungsten's recrystallization behavior is important since this process alters its material properties. As tungsten recrystallizes, there is an accumulation of internal stresses at the grain boundaries that result from recrystallization and grain growth processes, which coupled with the decrease in yield strength inherent to recrystallization make recrystallized tungsten more prone to large plastic deformation [16]. These internal stresses, coupled with the induced thermal stresses from the loading plasma can lead to increased surface roughening, crack networks formation and propagation [10]. There is also the concern that even though tungsten has a high melting temperature, high energy ELMs that add to the burden of the material (which is already handling ~10 MW m^{-2} of heat flux via active cooling during steady-state operation) may melt the surface of the material, causing additional damage [13]. This is because tungsten's thermal conductivity decreases with increasing temperature [1]. As the base temperature of operation increases, this property leads to the of energy influx needed from an ELM to reach and surpass the tungsten's melting temperature being reduced.

3.2 Deformation Microstructures

During hot deformation, tungsten, like most metals, finds dislocations appearing throughout the deformed structure, a process known as work hardening. This is convenient, as the change in hardness is a suitable and accessible characteristic to measure the evolution of the deformed microstructure further on [17]. For highly deformed ITER grade tungsten the dislocation density falls between 10^{12} m^{-2} and 10^{16} m^{-2} [18] which causes the already mentioned strengthening of the material. This is because the accumulation of these dislocations trap other mobile dislocations, and thus act as barriers for their motion inside the material, producing a higher energy barrier for this process. Additionally, the deformation increases grain boundary area, which traps the newly created dislocations. This new surface area creation accounts for a significant portion of the added internal energy, although its ratio depends on the type and extent of the deformation being carried out and the grain size of the sample [19].

Tungsten is a body centered cubic (bcc) metal with a high stacking fault energy (γ_{SFE} = 3.68 J m^{-2}), and as such deforms preferentially by slip and cross-slip along the plane families in its most densely packed directions ({110} / {122} / {123} <111> with slip along {110} being slightly more prevalent under expected ITER conditions, which lie between tungsten's T_m / 4 and T_m / 2) in contrast to twinning, which is more prevalent in low stacking fault energy metals (nevertheless twinning does sometimes occur in tungsten on the {112} <111> system) [17]. The planes associated with the described slip systems are aligned at different orientations from grain to grain, and in general are confined to their grain of origin. Thus, to maintain continuity inside the material, the grains are constrained by their neighbors, a situation which adds opposition to the deformation of the material [19].

3.3 Restoration Processes

The deformed structures described above store strain energy (free energy inside the material is raised) due to the accumulation of lattice defects, especially the increased density of dislocations and interface area [20]. This stored energy serves as driving force for the non-equilibrium transformations that take place during restoration [19]. Heating the material to high temperature (annealing) triggers thermally activated processes like solid state diffusion which provide paths to release this stored energy and leads to restoring the material to a state before

the creation of the deformed structures (dislocations, elongated grains, etc.…). The main restoration processes that occur during annealing are recovery, recrystallization and grain growth [19][21].

3.3.1 Recovery

The recovery process encompasses the initial changes in the material which start restoring the pre-deformation properties before recrystallization takes place. These first changes occur without a thermally activated incubation period and without largely modifying grain topologies in the material [19]. Recovery is incited by thermally activated motion, condensation, and annihilation of point defects, such as quenched in vacancies, and by rearrangement of the dislocation structure and concentration. During annealing, atomic diffusion leads to dislocation motion and relaxation, as well as partial annihilation of the dislocations and the point defects present which in turn results in relief of some of the internal stored energy [21]. Point defects created by plastic deformation are mostly absorbed at grain boundaries or are annihilated by dislocation climb. For the recovery stage, the dislocation motion during plastic deformation ends in the rearrangement of dislocations into dense clusters of dislocation "walls" with lower energy configurations lower stored energy configurations than the surrounding disordered dislocation structure enclosing lower dislocation density areas also called cells. This process results in lower lattice distortions and thus lower internal stresses in the matrix. Additionally these changes do not involve any long range motion of grain boundaries [19].

As recovery progresses, dislocations inside the cells annihilate while the cell walls evolve into more defined low angle boundaries forming subgrains [19]. Later on, subgrains will grow, this way decreasing their grain boundary areas and thus their boundary energy. These subgrains can also, if the low angle grain boundary is suitable, rotate and coalesce into a larger subgrain structure with a decreased boundary area and energy [21]. This process is illustrated in Figure 7. The microstructural changes mentioned are often subtle and hard to observe directly, so recovery is usually measured indirectly using calorimetry, electrical resistivity and / or hardness [21].

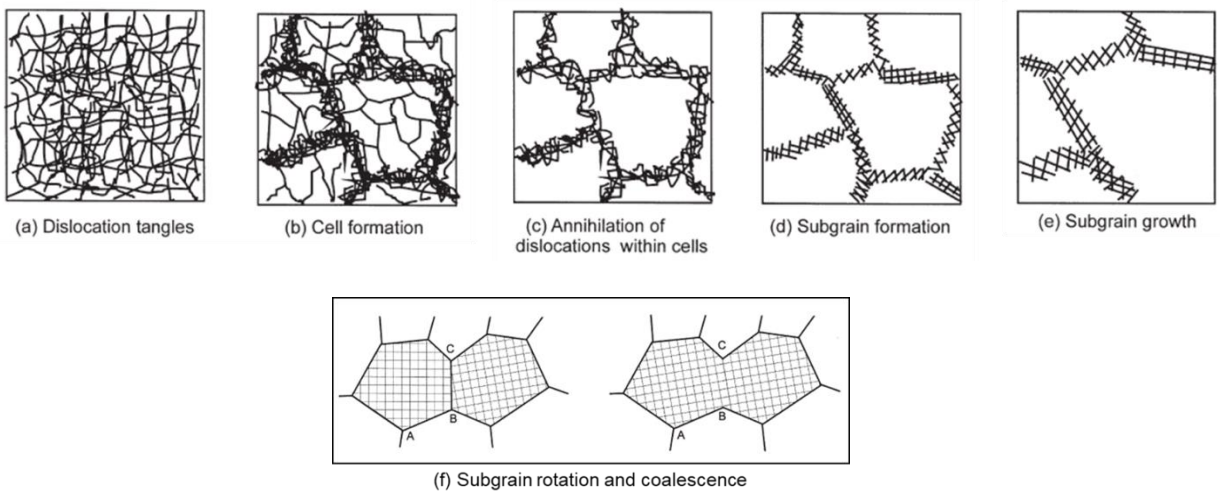

Figure 7. a - f) Typical stages of recovery in a plastically deformed material [19]

Stacking fault energy also plays a pivotal role in recovery, as it affects the extent to which dislocations dissociate, climb and cross slip. Low stacking fault energy metals have very little recovery and subgrain formation before recrystallization, in contrast with high stacking fault energy ones like tungsten, where dislocation climb is rapid and recovery effects are significant before recrystallization begins [19]. Recovery plays a paramount role in nucleating recrystallization since both processes are driven by the stored energy of deformation, to the point that the frontier between both processes is not clearly defined. Also, it is worth noting that recovery does not only occur during heat treatment and not only in plastically deformed materials [19], but for the purpose of this research we will concentrate on the aforementioned effects only.

3.3.2 Recrystallization

Recrystallization starts when new stress-free equiaxed grains begin to grow from nucleated crystals in the material, and as they grow they consume the already deformed or recovered microstructures. This consumption progresses by the creation and motion of high angle grain boundaries (HAGBs). This occurs due to the internal energy difference between the deformed structures with dislocations and defects, in contrast to the recrystallized grains, virtually free of them (strained versus unstrained part of the material) [19]. During recrystallization, the mechanical properties of the material that were changed during deformation tend to revert to those of the pre-worked state, most notably hardness, strength and ductility [20]. Figure 8 exemplifies the evolution of material properties with increasing recrystallization.

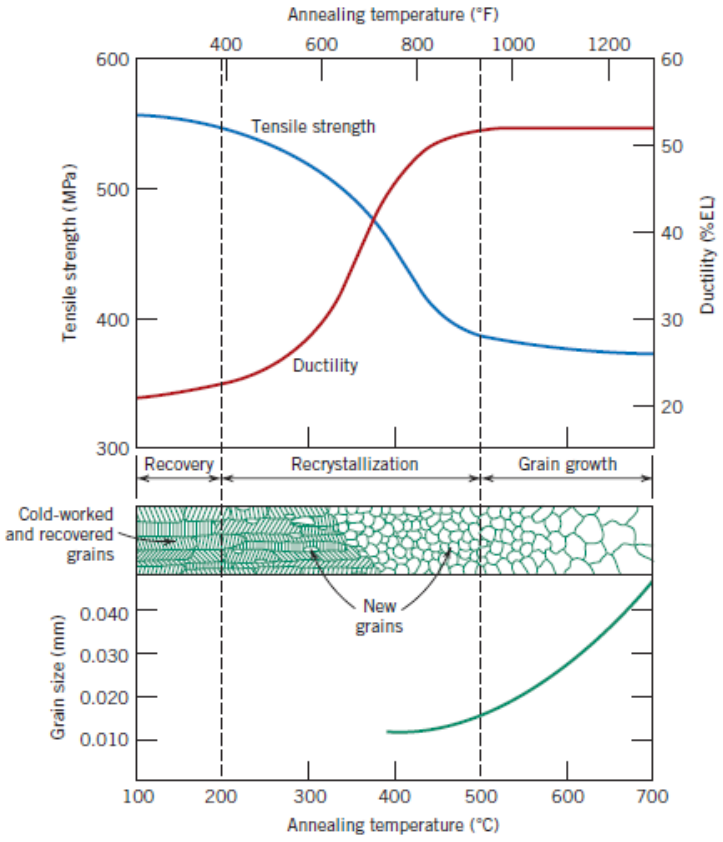

Figure 8. Example of the effect of temperature and degree of recrystallization on mechanical properties (ductility and tensile strength) and grain size of brass [20]

Recrystallization behavior is dominated by two regimes, nucleation and then growth. Nucleation refers to the formation of new stress-free grains, and growth to the progression of these grains consuming the deformed and recovered structures through short range diffusion. Growth continues until newly formed grains impinge [19]. The full process is shown schematically in Figure 9. The degree of recrystallization is commonly described by the fraction of the specimen being recrystallized (X_V). Recrystallization experiments and measurements are usually done under isothermal or isochronal conditions, and determine the conditions when 50% ($X_V = 0.5$) of the sample has recrystallized. For the former, the recrystallization time ($t_{0.5}$) is recorded, and the recrystallization temperature ($T_{0.5}$) for the latter [20].

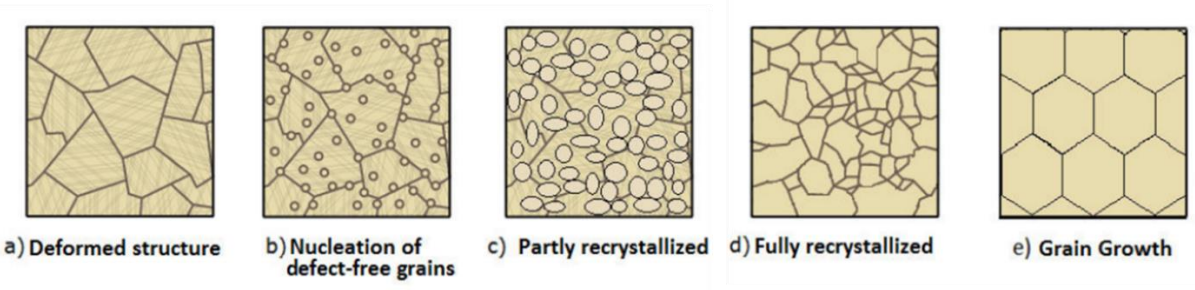

Figure 9. a - e) Schematic representation of recrystallization process [17]

Even though recrystallization is a very complex process, dependent on both time and temperature in engineering literature, typically a recrystallization temperature is specified, with the underlying assumption that it refers to the temperature where, after one hour of isothermal annealing, half of the volume has recrystallized. This approach is very sensitive to the purity and material concentration since this affects the high angle grain boundaries' mobility, so it is generally insufficient to characterize fully the recrystallization behavior. Some initial generalizations can be made for high purity materials. These are the so called laws of recrystallization formulated by Mehl, Burke and Turnbul from 1948 to 1952 [19]:

- A minimum deformation is needed to initiate recrystallization by providing nuclei and enough driving force to sustain growth.

- Recrystallization time decreases with increasing recrystallization temperature due to the Arrhenius relationship of recrystallization rate and the thermally activated mechanisms driving it.

- Recrystallization temperature decreases as strain increases due to the increased stored energy, which provides the driving force for recrystallization, i.e. nucleation and growth occur faster and / or at lower temperatures in more deformed materials.

- Recrystallized grain size decreases with an increased degree of deformation. A higher strain will provide more nuclei per unit volume leading to a final smaller grain size.

- Larger starting grain sizes and higher original deformation temperature will increase the recrystallization temperature, as grain boundaries are favorable sites for nucleation (leading to fewer sites on larger grains) and having already recovered grains during deformation lowers the available stored energy for recrystallization.

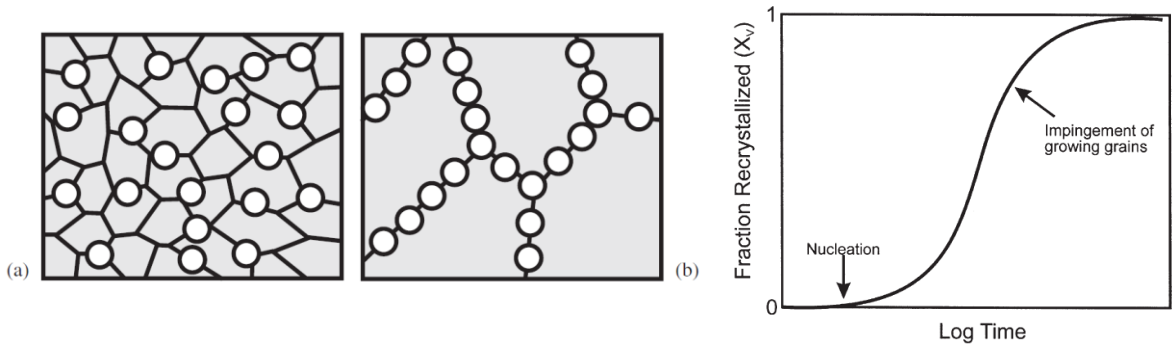

Figure 10. a - b) Effect of grain size on nucleation and c) typical recrystallization behavior during isothermal annealing [19]

High purity materials tend to recrystallize more easily than alloyed metals or metals containing impurities. Solute atoms induce drag on the moving grain boundaries and thus effectively modify their activation energy. Other parameters such as degree of cold work, initial grain size, and the degree of recovery before the activation of recrystallization affect the latter's behavior. Some other broader generalizations can be made: [21]

- A minimum degree of previous cold work is required, usually around 35% reduction; for high stacking fault alloys this value rises to around 45%.

- A minimum density of inhomogeneities in the deformed microstructure need to be present to provide a high local deformation energy that translates into a driving force inducing the accumulation of local lattice curvatures.

- These may include high dislocation density near grain boundaries, the existence of shear, transition and micro bands and precipitates / particles inducing grain boundary curvatures.

The aforementioned features provide the high local deformation energy gradient required for nucleation. Nucleation occurs when defect free regions of low internal energy, separated from the matrix by high angle boundaries, regions with a drastic orientation change (see Figure 11), with high boundary energy appear [21]. This in turns means that grain boundaries, triple junctions, and deformation bands that meet these high angle grain boundaries favor the appearance of nucleation sites on these locations [17].

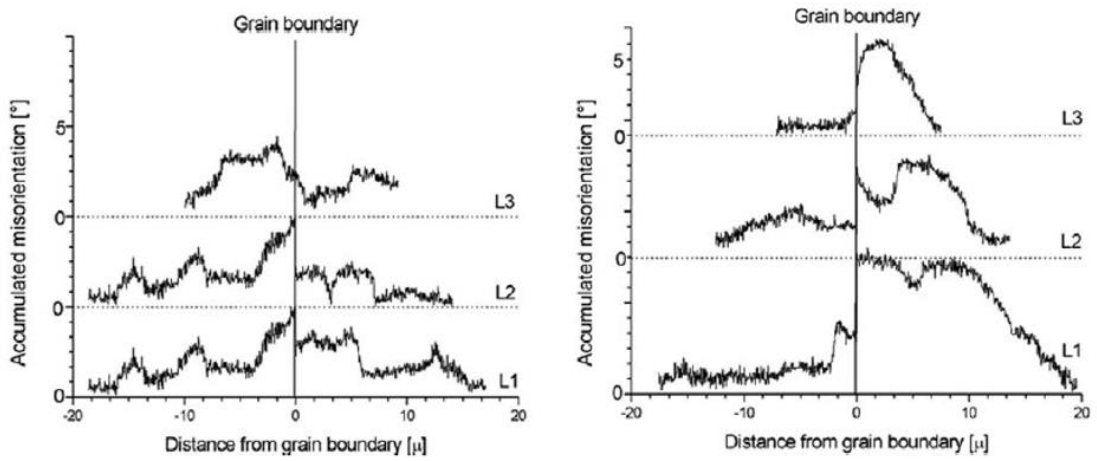

Figure 11. Example of a) low vs. b) high angle grain boundary misorientation profiles taken from EBSD measurements from aluminum bi-crystals [21]

High angle grain boundaries have a high local driving force with a strong grain boundary curvature. They are the main mechanism that "consume" the deformed microstructure, and thus are crucial for the recrystallization progression. Grain boundaries move upon the action of a driving force, but this mobility is reliant on the grain's crystal and plane orientation. Aside from this "external" driving force, a reduction in the total grain boundary area and density is enough to drive recrystallization and grain growth processes [21].

Crystal nucleation for recrystallization is a microstructural transformation process that is not in thermodynamic equilibrium (although the system can have local mechanical equilibrium). These defect free crystals are surrounded by the high angle grain boundaries described above (if not they do not contribute to nucleation ad growth and would be later consumed by the growing microstructure). Nucleation, even if considered continuous, is a non-homogenous phenomenon since the cold work deformation processes do not give a homogeneous distribution of defects from where, upon annealing, recrystallization will nucleate. At the core of it, nucleation is a consequence of microstructural inhomogeneity at the site of major stored energy gradients [21].

The coupled nucleation and growth mechanisms characteristic of recrystallization, can be described by studying the transformed volume fraction over time into a homogeneous matrix i.e. from cold work to recrystallized state. This process describes a sigmoid curve that has been characterized by the JMAK (Johnson, Mehl, Avrami and Kolmogorov) equation. This approach can consider a continuous nucleation rate of the recrystallization crystals or having a fixed number in the material prior to recrystallization which grow until they impinge. The recrystallization over time is thus generally characterized by equation 3.1, where X is the recrystallized volume fraction over time t, B is a material dependent constant and n is the Avrami kinetic exponent [22]:

$$X(t) = 1 - \exp(-B \cdot t^n) \tag{3.1}$$

As mentioned earlier this approach assumes homogenous nucleation and thus in its simplicity lacks a true description of heterogeneous recrystallization and growth processes with non-constant growth rate, but it is nevertheless a reasonable place to begin an approach towards recrystallization calculations. More complex simulation approaches would make use of statistical analysis and spatially discrete models to better describe reality.

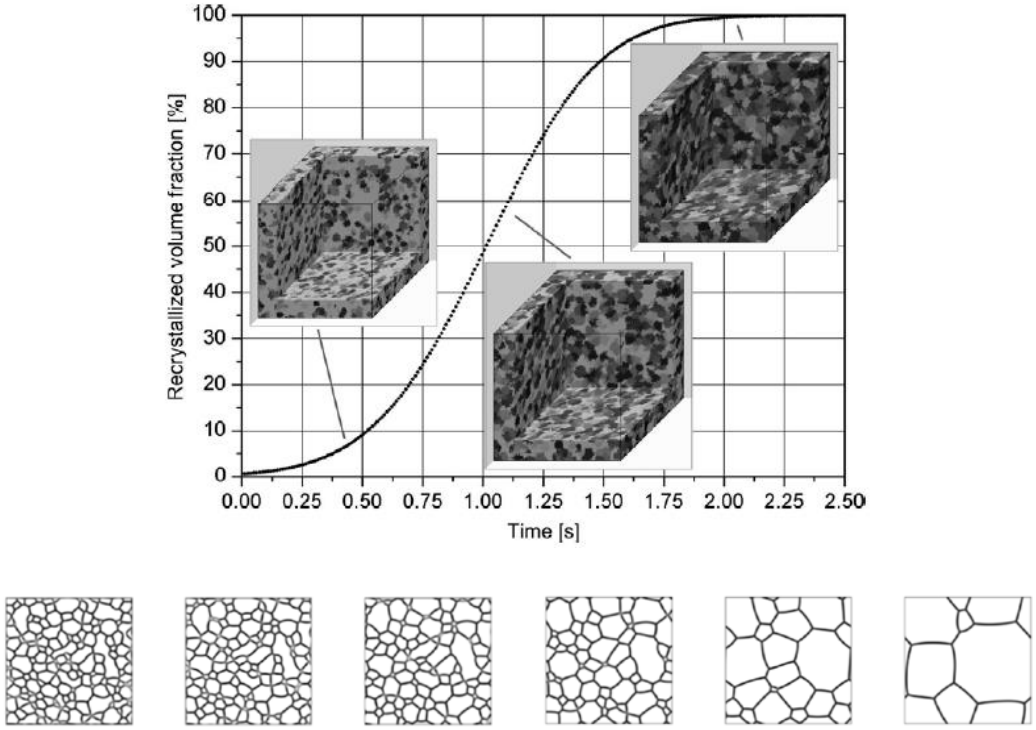

Figure 12. Sigmoid curve and simulation showing recrystallization progression over time[21]

The grain boundary motion itself can be modeled after the Turnbull rate equation for interface migration for calculating how fast grain boundaries move during annealing, and thus the recrystallization rate. [21]:

$$\dot{x} = nmp = nm_0 \exp\left(-\frac{Q_{gb}}{k_B T}\right) p \tag{3.2}$$

Here, $\dot{x}$ is the grain boundary's velocity, n is the normal of the grain boundary segment (measure of misorientation), m is the grain boundary mobility, with m_0 being the material dependent statistical pre-exponential factor, Q_{gb} is the grain boundary motion activation energy, T is the temperature and p is the Gibbs free transformation energy difference across the interface (the driving force). Literature in the field shows that the grain boundary mobility is strongly coupled with the crystal misorientation (n above) up to 32° – 40°, with the activation energy for grain boundary motion decreasing steadily as the misorientation reaches this range. These grains show lower solute impurities between them, which in part explains high the mobility as well. [22]

The aforementioned solute atoms reduce the thermodynamical instability of the grain boundaries by reducing the boundary's self-energy, and changing the grain boundary's structure which also modifies its mobility. These changes explain why grain boundaries have a higher impurity equilibrium concentration, and why the solute effects are more pronounced in these areas. These solute atoms tend to slow the grain boundary motion by means of a drag force p_i defined by the Detert model [21]:

$$p_i = nC_0 f \tag{3.3}$$

Where f is the force on the boundary per solute atom, and C_0 is the atomic fraction of the equilibrium concentration. The equilibrium concentration is defined in terms of C_∞, the mean bulk impurity concentration and E, the boundary impurity interaction energy [21]:

$$C_0 = C_\infty \exp\left(-\frac{E}{k_B T}\right) \tag{3.4}$$

When the grain boundaries begin their motion and reach steady state, the drag force f helps define their velocity v in terms of the solute's grain boundary diffusion coefficient D as [21]:

$$v = \left(\frac{D}{k_B T}\right) f = \left(\frac{D}{k_B T}\right) \frac{p}{nC_\infty \exp\left(-\frac{E}{k_B T}\right)} \tag{3.5}$$

Other more complex models reach the same overall conclusion from their analysis that solute atoms act with a drag force on the grain boundary motion. Mobilities have been observed to vary depending on the grain boundaries' misorientation but overall, the impurity content is the main driving factor for the grain boundary drag force [22].

3.3.3 Grain Growth

After recrystallization ends, if the high temperatures are maintained the newly formed grains will continue to coarsen and compete to achieve a lower free energy state by reducing the total grain boundary area per volume. Smaller grains will be consumed by larger grains as their grain boundaries migrate, with the net result being a smaller boundary area and thus a lower total energy in the system [19]. This grain growth is also associated with the degradation of mechanical properties compared to those of fine-grained metals such as ductility and strength [17].

3.4 Damage Formation

As mentioned earlier, ITER grade tungsten is heavily deformed, with elongated grains in a consistent orientation parallel to the loading direction of the surface which is also the heat transfer direction. Even using the ITER grade guidelines for material properties and orientation, under specific loading conditions damages and cracking do occur [23][24]. The crack resistance of the material depends on its strength, toughness, thermal diffusivity and thermal

expansion coefficient [25]. Of special concern is the growth and propagation of crack networks, and the understanding of how this is influenced by both the internal (microstructure and material) properties, as well as the external ones (loading conditions) [23][24].

Under ITER-like loading conditions, the tungsten of the divertor will experience high heat flux loads under steady and transient regimes. As power density increases, damage begins to be induced in the material. According to Wirtz et al. [23], five main damage responses of tungsten to these loading conditions can be observed with increased power density application (see Figure 13). 1. No damage, referring to no surface change in the material's morphology. 2. Surface modified, referring to identifiable roughening, swelling, grain size and other morphology changes. 3. Microcracks which have a length in the order of ~10μm. This damage classification was not in the original literature, but was added in this work to provide a more refined categorization of the cracking behavior. 4. Small or isolated cracks, which are arbitrarily distributed in the affected area, and show no correlation among each other. And finally, 5. crack networks, which show continuous interconnected cracks of comparatively larger size.

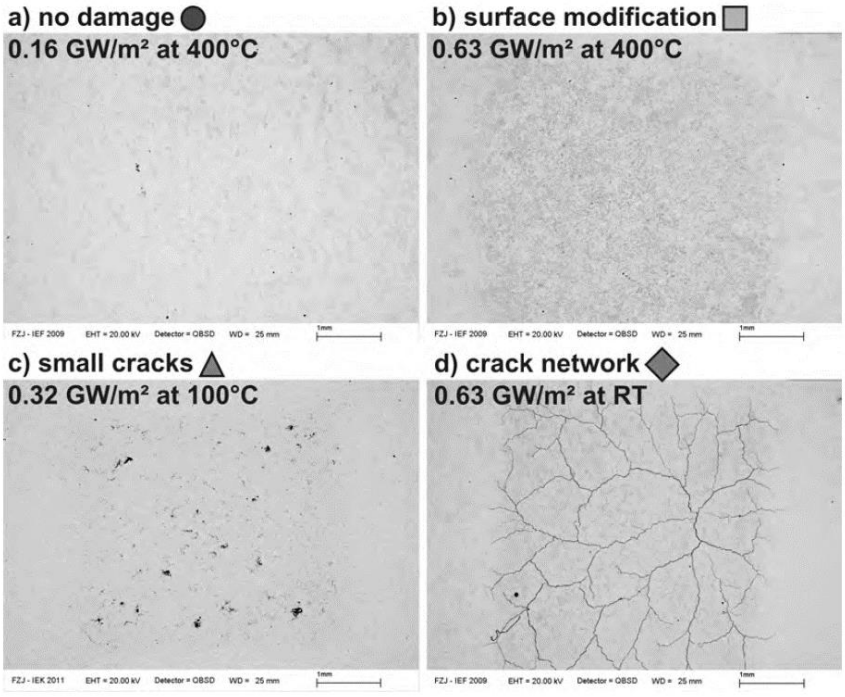

Figure 13. Tungsten damage responses [23]

The damaging process tends to proceed as shown in figure 14: first, roughening is observed on previously smoothed and polished samples. This is caused by the exposed material experiencing thermoplastic deformation due to the grains with higher temperature being prevented to expand by the surrounding lower temperature grains that exert a compressive stress on them. When the metal cools, these compressive stresses become tensile stresses which ultimately cause the deformation that is observed. If these tensile stresses become higher than the tensile strength of tungsten, cracks will start to appear to relieve the stress. If heat flux becomes even higher, parts of the material will experience melting and re-solidification pools will appear in the exposed samples [1].

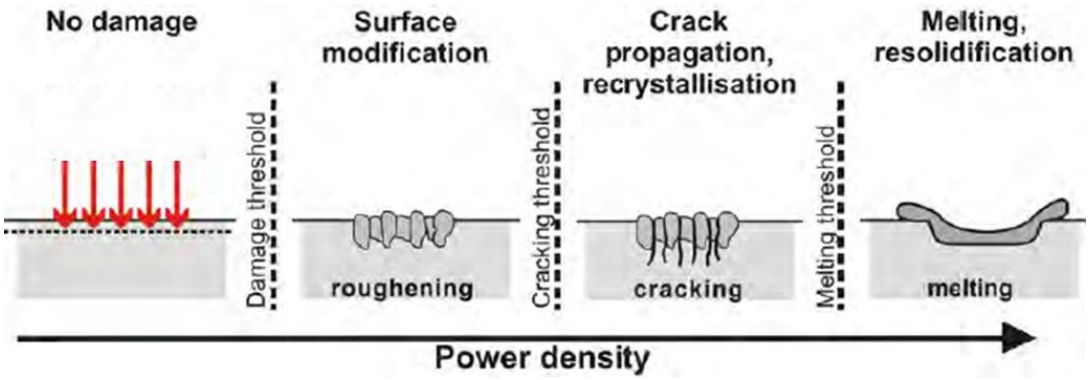

Figure 14. Schematics of possible induced damages on tungsten after irradiation [1]

Under the expected heat flux conditions, the gravest identified failure mode is brittle failure due to crack formation and propagation [26]. Previous experiments show that in general crack formation and propagation (length) increases with applied power density, and crack propagation has been identified to be primarily intergranular, along the weak grain boundaries in the direction of deformation / elongation. This has supported the decision of using grains oriented parallel to the loading direction for the divertor's material, since cracking of perpendicular sections leads to delamination-like effects (see Figure 15b) which promote surface melting and sputtering since they effectively become thermally isolated from the actively cooled bulk. These effects can jeopardize the plasma through contamination cooling as they detach [1].

Grain orientation and recrystallization play also a significant role in damage formation, as recrystallized tungsten has a lower tensile strength than deformed one [23], and also larger grains promote longer cracks through the material [1]. High angle grain boundaries promoted during recrystallization lead to grain boundary embrittlement and weakening, with brittle impurities segregating to the grain boundaries. This leads to intergranular cracking behavior when the stress reaches the tensile strength of the matrix. When grain growth is also taking place, transgranular cleavage starting at the high angle grain boundaries starts to dominate [17].

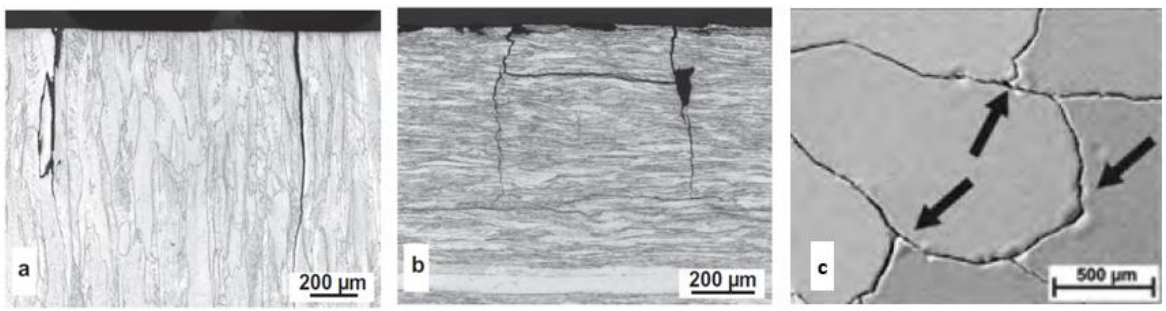

Figure 15. Crack propagation on tungsten samples loaded a) parallel and b) perpendicular to the grain orientation, and c) melting sites on grain boundaries [1]

These past experiments also reveal that high heat flux fatigue testing on ITER divertor prototypes, show deep cracking due to thermal fatigue, with transient thermal loads of over 300 cycles at 20 MW m^{-2} being the critical boundary (it should be noted that these loads were of ~10 seconds, and thus do not properly represent thermal shock of shorter pulse lengths like the ELMS studied in this work). Thermal shock and fatigue are originated by stresses caused by temperature gradients self-equilibrating during thermal cycling without an applied external mechanical load [26]. Ideally, while characterizing thermal fatigue, mechanical constraints are reduced enough to not cause transformation of thermal strain into mechanical strain in the material. This prevents shakedown (elastic and plastic) effects to accumulate. This is not the case on a scale of the grains, where the thermal gradients between grains result in mechanical constraints leading to the compression and tension responsible for the cracking as described earlier [25].

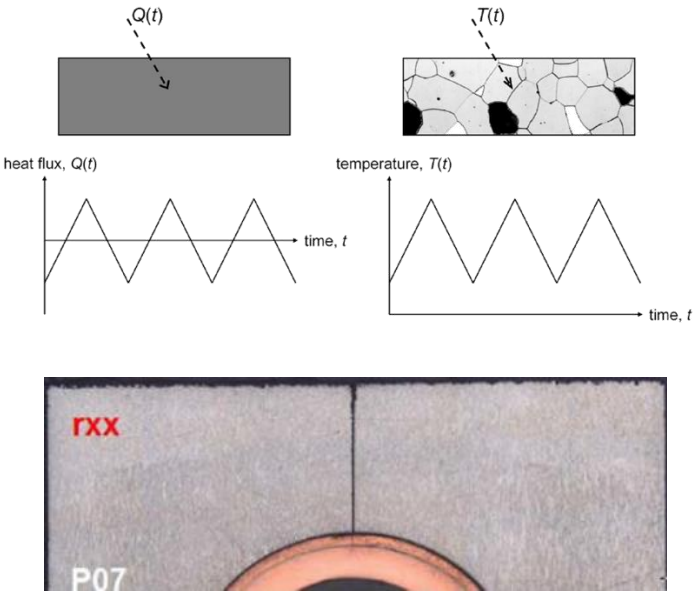

Figure 16. a) Schematic of possible thermal fatigue conditions [25] *and b) thermal fatigue macroscopic crack on ITER-like tungsten prototype* [26].

During transient pulse testing of previous experiments, the prototype's surface (Figure 13.b) show increased plastic deformation on the grains, with crack growth being consistent with brittle failure. This has led to the understanding that the cracks under these conditions are initiated under a Low Cycle Fatigue (LCF) regime. Plastic LCF failure is dominated by the magnitude of strain amplitude and the increment of accumulated plastic strains during cyclic loading, in this case in the near surface of the material. Li et al., assuming the material to be linearly elastic and ideal-plastic and ignoring kinematic hardening, propose the following cracking mechanisms for this scenario [26]:

1. During transient loads, the temperature rises in such a strong manner that the surface layer of tungsten loses most of its yield strength due to recrystallization-induced thermal softening.

2. Concurrently, thermal stresses in the near-surface region cause plastic yield as described in the literature.

3. During cooling, plastic yield continues due to residual stress.

4. Plastic strain accumulates with increasing number of cycles producing fatigue cracks (which may also be formed at preexisting defects).

5. Cracks with preferred crack tip stress intensity grow.

6. Crack growth is promoted by the brittleness of recrystallized tungsten.

Since the recrystallized material will accumulate a high degree of plastic deformation, it has higher risk to suffer from plastic LCF than the surrounding not recrystallized one, which means that fatigue cracks are more likely to appear and grow in this area of exposure. During thermal cycling, cracks appear to grow during surface cooling, as this type of strain acts by opening the crack. Simulations at high temperature and heat flux suggest that if recrystallization is suppressed cracks would not form or propagate to the cooling tube area [26].

3.5 Hydrogen Plasma and tungsten Interactions

Since as a plasma facing material, tungsten will be subject to a substantial particle flux, hydrogen atoms may penetrate the surface and diffuse through the bulk affecting its original material properties. Hydrogen retention has been observed to assist vacancy formation and bubble, and induce embrittlement in tungsten [27], reason for which it has generally been seen as undesirable, and is one of the concerns in ITER oriented research [28]. This leads to a need of understanding diffusion and solution of hydrogen in tungsten.

In general, when H ions encounter the wall, an electron is captured from the surface and the hydrogen becomes neutral. The incident energy from the plasma will determine how far the fraction of H atoms that are implanted in the tungsten wall will travel (implant zone). This plasma intensity is determined by its electron temperature (T_e) and electron density (n_e). These two parameters, mainly the energy of the charged particles, and how many are there, control the particle flux (Γ) that is received by the target. Not all hydrogen atoms from the plasma go into the tungsten. Most atoms, (>99%) are actually reflected, meaning that when encountering the wall, they pick an electron from the tungsten, and reenter the plasma as a neutral particle [29].

H ions which do enter the material get neutralized and form an implant zone several nanometers below the exposed surface. H atoms from this implant zone will occupy interstitial positions in the tungsten's bcc lattice before starting to diffuse into the bulk due to the concentration gradient. As hydrogen diffuses it is retained by different "traps" in the material, mostly crystallographic defects, such as vacancies, dislocations and grain boundaries. Hydrogen atoms may also encounter each other in suitable locations to form H_2 and form bubbles which will either stay trapped in the defects or degas out of the system. This process is schematically shown in Figure 17, along with the energy diagram for the W – dissolved H system [30].

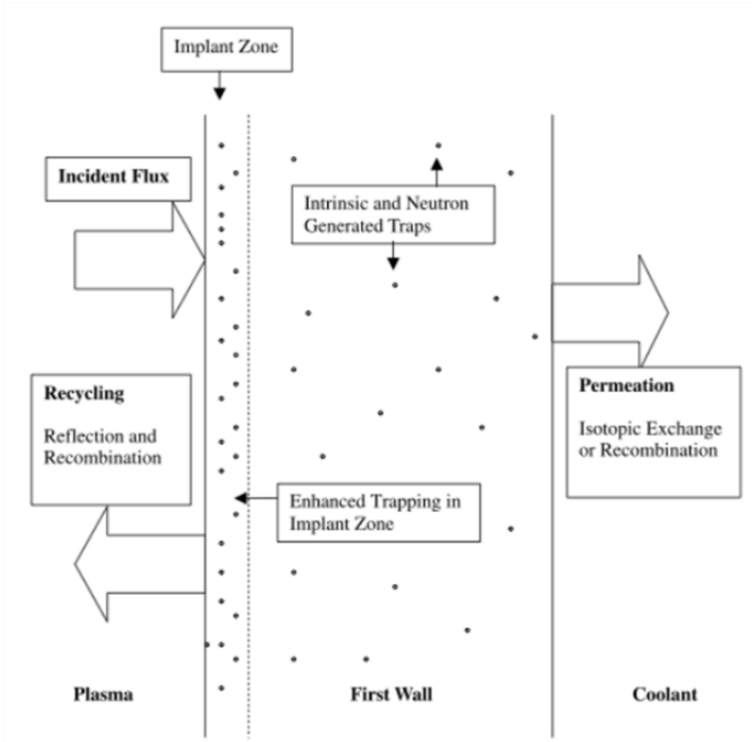

a)

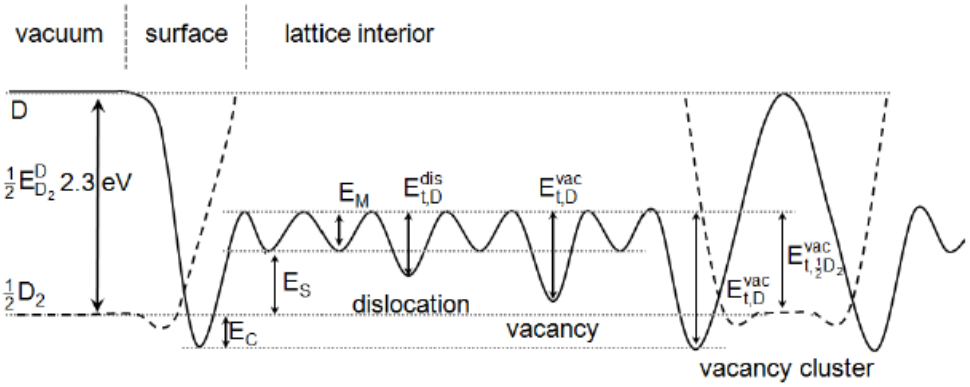

b)

Figure 17. a) Schematic of H implantation process in the Divertor [30] *and b) energy diagram of dissolved H in W showing the trapping energies of common defects as well as the migration energy E_M, the surface chemisorption energy E_C and enthalpy of solution E_S* [31]

3.5.1 Diffusivity

Hydrogen diffuses through tungsten's bcc crystal structure in solid solution through interstitial sites between the lattice planes due to their significant atomic radius difference (25 vs. 135 picometers) [27]. During interstitial diffusion, atoms of the solute penetrate in the direction of highest to lowest concentration C (defined by the number of atoms n over jumping distance α) by means of "random jumps" with a frequency Γ of jumps per time unit across α. The atomic flux of a solute atom B in a matrix A from one plane to another (i.e. 1 to 2) is given by [32]:

$$J_B = \frac{1}{6}\Gamma_B(n_1 - n_2) = -\left(\frac{1}{6}\Gamma_B\alpha^2\right)\frac{\partial C_B}{\partial x} \tag{3.6}$$

We can group the temperature dependent term away from the concentration term into the diffusivity *D* yielding what is known as Fick's first law of diffusion [32]:

$$D_B = \frac{1}{6}\Gamma_B\alpha^2 \therefore \; J_B = -D_B\frac{\partial C_B}{\partial x} \tag{3.7}$$

The *Γ* "jump" process of diffusing atoms is a thermally activated one. At higher temperatures, thermal vibrations will facilitate these jumps and increase the jumping frequency Γ. To move to another interstitial site, the solute atoms need to force the matrix lattice atoms into higher energy positions to let the solute atom pass through. This work requires an increase in the free energy of the local atoms. This increase is known as the activation energy E_{act}. On average a fraction of the atoms will vibrate with an E_{act} higher than the mean of the system and will be able to jump. If an atom makes υ attempts per unit time to jump to any of *z* available interstitial sites, the jumping frequency can be defined as [32]:

$$\Gamma_B = z\upsilon \exp\left(-\frac{E_{act}}{k_B T}\right) \tag{3.8}$$

Adding this to the diffusivity equation incorporates the material dependent diffusion coefficient D_0 into the full thermally dependent equation [32]:

$$D_B = \frac{1}{6}\alpha^2 z\upsilon \exp\left(-\frac{E_{act}}{k_B T}\right) = D_{B0}\exp\left(-\frac{E_{act}}{k_B T}\right) \tag{3.9}$$

Propagation of hydrogen inside the tungsten bulk is then governed by the time (*t*) and depth (*x*) dependent Fick's second equation (equation 3.10) [32] that when solved for the 1D case assuming constant surface concentration over time gives the time and depth dependent concentration function *C(x,t)* (equation 3.11) [30] where C_0 is the initial surface concentration and *erfc* is the complementary error function:

$$\frac{\partial C_B}{\partial t} = D_B\frac{\partial^2 C_B}{\partial x^2} \tag{3.10}$$

$$C(x,t) = C_0 \cdot \mathrm{erfc}\left[\frac{x}{2\sqrt{D_B \cdot t}}\right] \tag{3.11}$$

3.5.2 Hydrogen Penetration in Tungsten

For the case of hydrogen loaded tungsten, several milestone experimental relationships are established in the literature. Frauenfelder, Zakharov and Benamati among others determined

the diffusivity of tungsten at different temperature regimes shown in Figure 18 [27]. These diffusivities and solubilities fit well with an Arrhenius type equation as can be seen from the results below [33]:

- $D = 4.1 \times 10^{-7} \exp\left(-0.39 \frac{eV}{k_B T}\right)$ in $\left[\frac{m^2}{s}\right]$ at 1200 – 2400 K (Frauenfelder)
- $D = 6.0 \times 10^{-4} \exp\left(-1.07 \frac{eV}{k_B T}\right)$ in $\left[\frac{m^2}{s}\right]$ at 850 – 1060 K (Zakharov / Benamati)

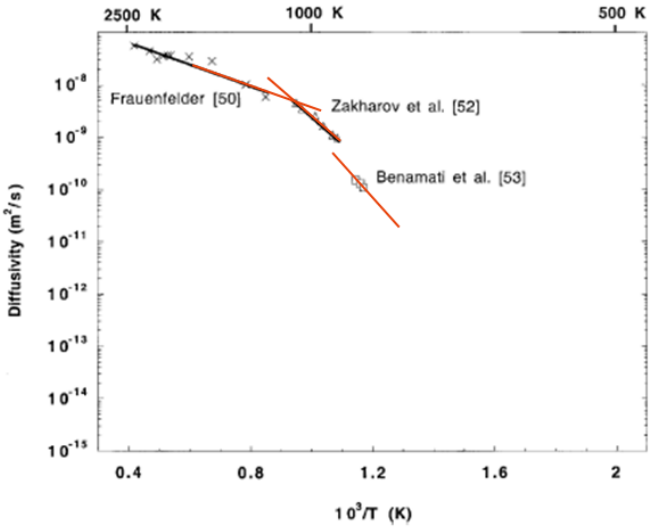

Figure 18. Experimentally determined hydrogen diffusivity on tungsten with this project's operation range highlighted [27]

Further testing outside the scope of this research has shown lack of agreement in the observed behavior as the temperature lowers, which has prompted a reexamination of the measured data, and a proposed new relationship based on understanding the penetration mechanisms at play. Kong, [24] Heinola, [25] Fernandez [26] and others, have proposed a first-principles simulation approach to determine a relationship that agrees with observations. First-principles or ab initio calculations, attempt to simulate and predict material behavior based on quantum mechanical theory, without introducing higher scale factors like material properties.

3.5.3 Hydrogen Defect Trapping

As mentioned earlier, crystallographic defects effectively capture the hydrogen dissolving through the barrier, forcing it to overcome an energy barrier of the respective trap to leave the site (see Figure 18). This increases the time to desorb any H atom caught, and raises the apparent activation energy for diffusion. This can be modeled by the Mac-Nabb and Forester formula where D_{perf} is the diffusivity of the perfect system (calculated above), c_{trap} is the trap concentration and E_{trap} is the trapping energy of hydrogen inside one trap [27]:

$$D_{eff} = \frac{D_{perf}}{1 + c_{trap} \exp\left(\frac{E_{trap}}{k_B T}\right)} \tag{3.12}$$

The referred studies distinguish two typical ranges of trap regimes, “mobile” traps which are interstitial sites through which solute atoms diffuse, and “intrinsic” traps which encompass the previously mentioned crystallographic defects. The latter group accounts for the dominating effect at higher temperatures, and exist at an atomic concentration of 10^{-4} at. % in the unirradiated tungsten bulk. Mobile trapping calculations account consistently for the behavior observed at low temperatures (30 – 350 ºC) while defects seem to be the dominant trapping mechanism at higher temperatures (500 – 1000 ºC). This is explained that during exposure, hydrogen falls easily trapped in the lattice interstitials since they are abundant in the matrix, but, as temperature rises these atoms can be activated and desorbed from these lower energy traps, while the higher energy traps lock the hydrogen atoms in place due to their higher trapping energy as previously shown. If on the other hand, hydrogen atoms are trapped in defects near the surface, they have been found to form a high pressure near surface area that leads to micro cracks and blistering formation. This process might release tungsten atoms into the plasma cooling it down. A schematic of the induced defects due to near surface trapping is shown in Figure 19 [34]:

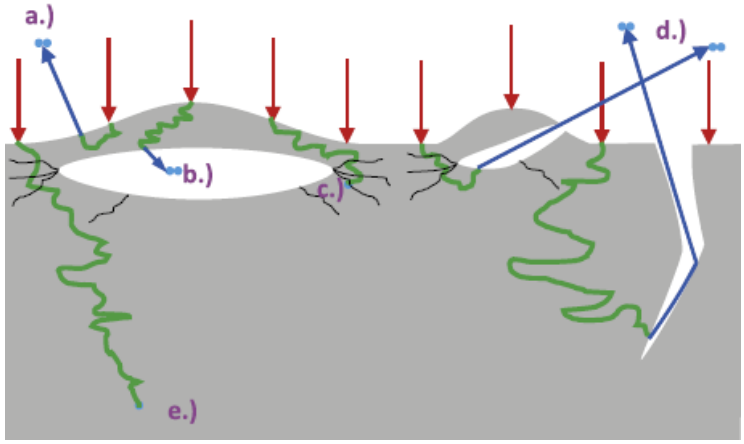

Figure 19. Surface trapped hydrogen and induced defects and behaviors: a) degassing of implanted H, b) H trapping in blisters, c) trapping of H in the dislocation network d) degassing from open cavities and cracks and e) trapping of H in the bulk. [34]

4. Project Motivation

4.1 Background

Since tungsten is the chosen armor material in the divertor of the ITER tokamak, understanding its behavior under ITER reactor operator conditions is paramount for the success of the reactor. If after steady state operation, and subsequently being subjected to ELMs as part of the expected behavior of the reactor, the tungsten crosses the recrystallization threshold, its thermo-mechanical properties, especially its thermal shock resistance, yield and tensile strength, are expected to degrade leading to cracking and component failure as has been previously described.

Previous testing of ITER grade tungsten samples by Loewenhoff et al. [35] showed no recrystallization or cracking when exposed to simulated hydrogen plasma ELMs in Magnum-PSI. This behavior deviates from established literature on tungsten recrystallization performance, but is in agreement with simulations suggesting that if no recrystallization occurs, fatigue cracks and their associated brittle failure do not occur [26]. This phenomenon was not observed when companion samples were exposed to similar conditions under electron beam loading (See Figure 20 comparison) [35] and it is at odds with established literature on furnace heating of tungsten to similar temperatures [17].

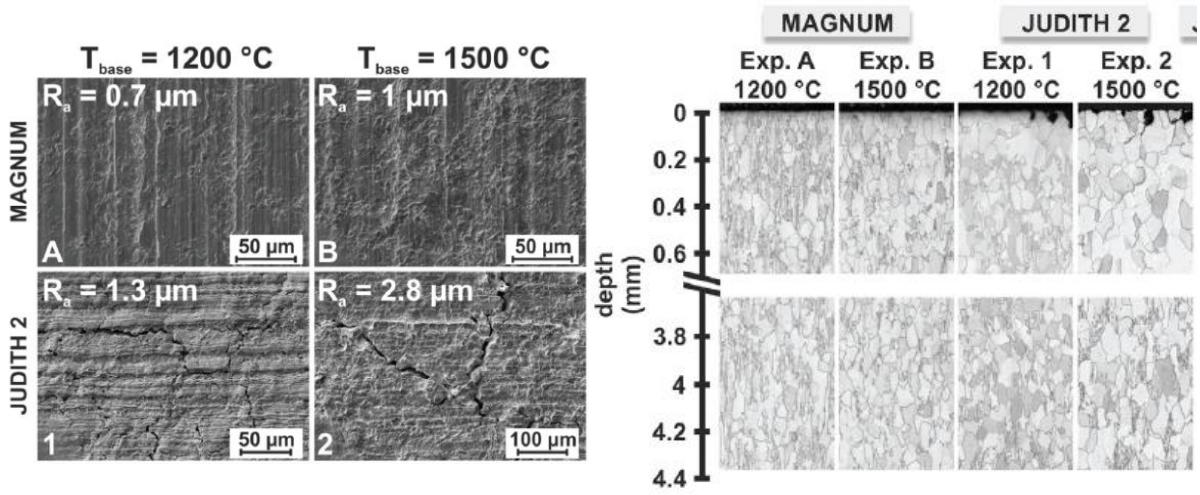

Figure 20. a) Surface SEM and b) cross-section metallography of W samples exposed to H-plasma and equivalent e-beam loading. Cracks and recrystallization are evident on the samples exposed to the e-beam but not on plasma loaded ones [35].

Understanding how and why these behaviors are being observed is critical to fully validate the environmental ranges in which the divertor can appropriately operate. An in-depth understanding of the material interactions at high temperatures and fluxes is key to predict the behavior expected during ITER full scale operation.

4.2 Hypothesis

It is hypothesized that during the hydrogen plasma loading, plasma ions may have a suppression effect on W's recrystallization / recovery processes leading to an enhanced mechanical performance, specifically resistance to crack formation and propagation during operation under ITER reactor conditions. Experimental data on hydrogen plasma exposure on tungsten samples show significantly less surface roughening, and a reduced average crack width than equivalently electron-beam exposed samples, suggesting a better performance against thermoplastic deformation. If true, this enhanced resistance to plastic deformation under loading would delay the onset of crack formation in the material [1].

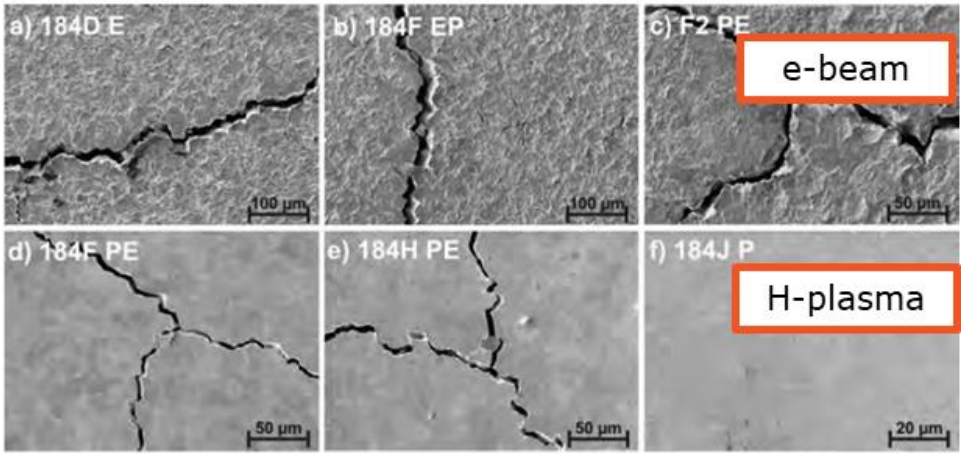

Figure 21. Roughening comparison between a – c) e-beam and d – f) H plasma exposures [1]

The observed effects during H plasma loading may be the result of hydrogen diffusion into the tungsten lattice and forming hydrogen molecules which are later trapped in lattice defects such as vacancies, dislocations and grain boundaries, inducing internal stresses in the lattice. This process typically induces hydrogen embrittlement in the material, as the internal stresses induced in the lattice can reduce its fracture toughness [36].

Taking the above into account, there might then be two competing mechanisms, one resulting in a delay in the onset of crack formation due to better performance against thermoplastic deformation, and one resulting in a lower fracture toughness leading to classic hydrogen embrittlement and the reduced fracture toughness associated with it. The observed suppressed recrystallization in H plasma exposed samples seems to suggest that at least under certain conditions, the first effect dominates. Understanding how then hydrogen diffusion during plasma loading affects tungsten recrystallization may lead to determining an "enhanced performance" threshold for tungsten under these conditions.

The correlation between base temperature, temperature gradients, heat flux and particle flux and the induced damage on the divertor tiles still needs to be fully expanded under the relevant working conditions. The trend of heat flux being the determining factor on this matter explored in current body of research is expected to still dominate under the ELMs regimes. There is also evidence that prolonged exposure to these conditions, especially transient events like ELMs, may degrade the properties of tungsten over time as illustrated in Figure 15 [37][38]. Identifying the mechanisms underlying the behavior of the mechanical properties of tungsten

under the relevant regimes for ITER operation, particularly under conditions where recrystallization may take place, is thus the main research question of this work.

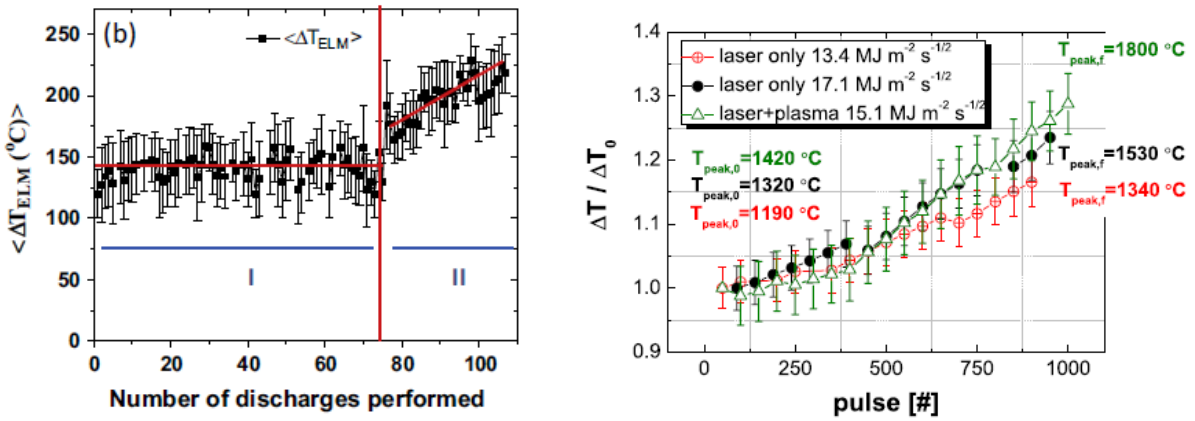

Figure 22. Change in thermal response after prolonged exposure of ITER grade W samples to H-plasma discharges [37] *and combined plasma and laser discharges* [38]

4.3 Scope

For this project's realization, ITER-grade tungsten samples were exposed to hydrogen plasma in Magnum-PSI under varying conditions to simulate steady state and ELMs relevant settings in the divertor. Based on the temperature response analysis of the samples exposed to the H plasma, correlations and data mapping of the effects of temperature and heat/particle flux on ITER grade tungsten is devised, as well as analytical rationale for the observed behaviors.

First, thermal response to ELMs over time is analyzed and compared to existing experiments by Bardin and Eden et al. (refer to Figure 22 [37][38]) to determine the thermal conductivity evolution over prolonged exposure to create a baseline for the analysis of the material's behavior.

Surface damage mappings correlating the observed damage features with the surface temperature and the applied pulse heat flux (akin to those by Wirtz, Hirai and others in Figure 23 [23][24]) are then elaborated, to incorporate the simulated ELMs. This analysis is performed at relevant points along an exposed sample's radius, and classifying the identified damages as described in section 3.4. At these points, equivalent temperatures, fluxes, mechanical properties and observed morphologies under the different pulse regimes (mainly different sized ELMs) can be compared, thus creating a more comprehensive mapping of tungsten's behavior under plasma loading.

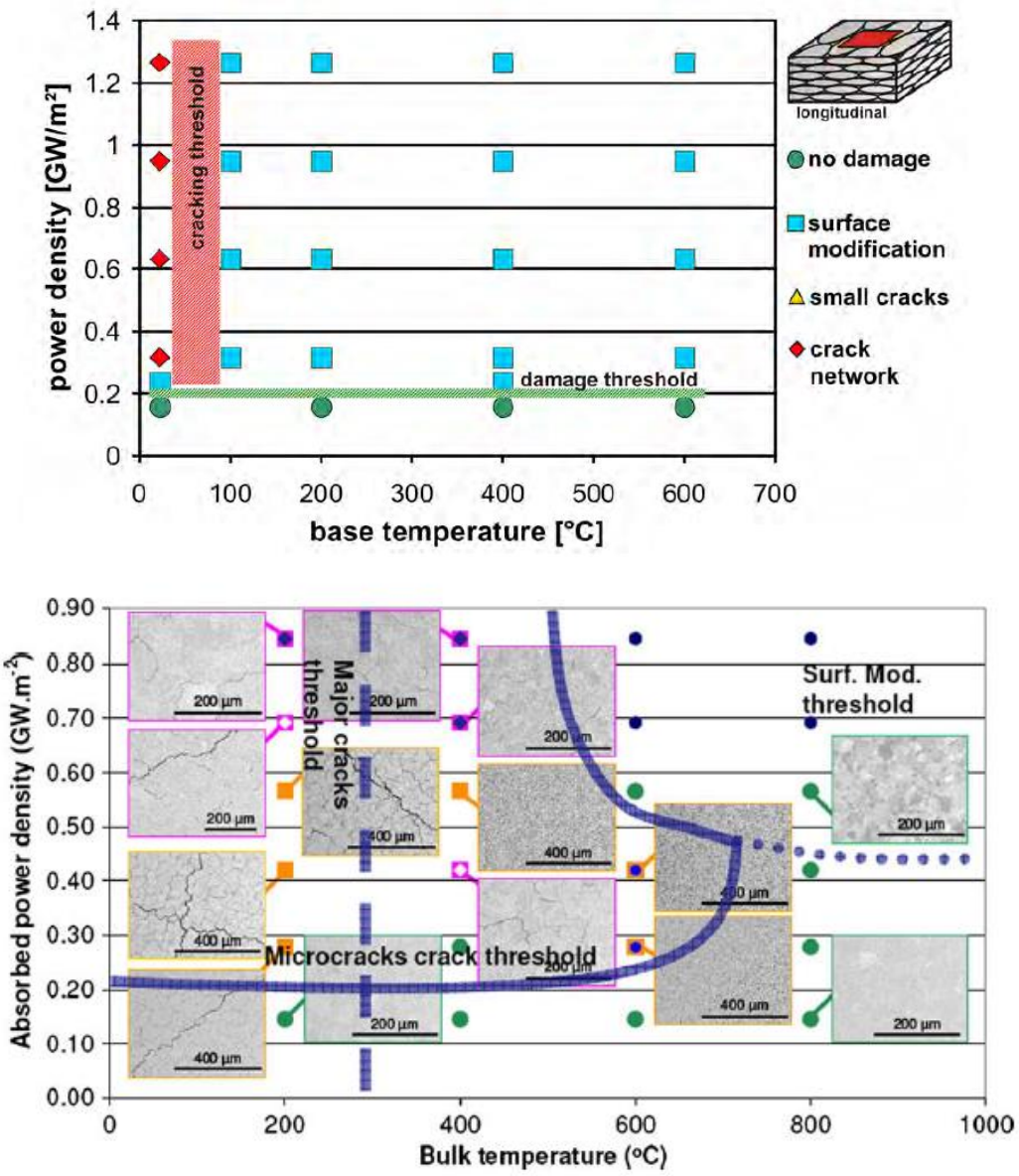

Figure 23. Tungsten damage mapping under different loading conditions [23][24]

Microhardness and imaging (Light microscopy (LM), scanning electron microscopy (SEM), and electron backscatter diffraction (EBSD)) data from surface and cross-section of samples is processed and correlated with temperature and heat/particle flux profiles (measured and simulated) to determine the extent of recovery and recrystallization. Comparisons with established literature and analytical models are made to characterize the behavior of tungsten's restoration processes under H plasma loading. With the aid of Thomson Scattering data from the plasma exposure, implantation of H is calculated and simulated through the material bulk and used to account for the possibility of solute drag due to H presence being a significant factor in W's restoration kinetics.

5. Experiment Details and Procedure

5.1 Materials

Magnum-PSI at DIFFER, was used to load a set of samples under ITER reactor relevant conditions simulating steady state conditions and repeated transient heat loading to mimic ELMs striking the target. An ITER grade polycrystalline tungsten rod with square cross-section (36 x 36 mm²) was procured from Plansee SE for the purpose of this experiment. Powder metallurgy was employed for the manufacturing of mentioned rod, with tungsten purity certified by the manufacturer at 99.97%. Although the specific manufacturing specifications were not disclosed by the manufacturer due to confidentiality, it is stated that the sintering temperature was between 2000 and 2500 °C, and the material was annealed at 1000 °C after bidirectional forging [39] (Figure 24 illustrates a typical manufacturing process for these type of samples). The end result of this process being a square rod which, when cut transversally grains are oriented perpendicularly to the "face" of the slide as shown on Figure 25a. These grains have an average diameter of ~10 µm in the transverse direction and an elongated structure of 5 x 25 μm^2 in the rolling direction (Figure 25b). From this source rod, 12 pure tungsten disc samples (Ø30 mm x 4 mm) were cut and mirror polished to be made available for the experiments, 9 of which were supplied for the hydrogen plasma loading experiment in Magnum-PSI at DIFFER [40].

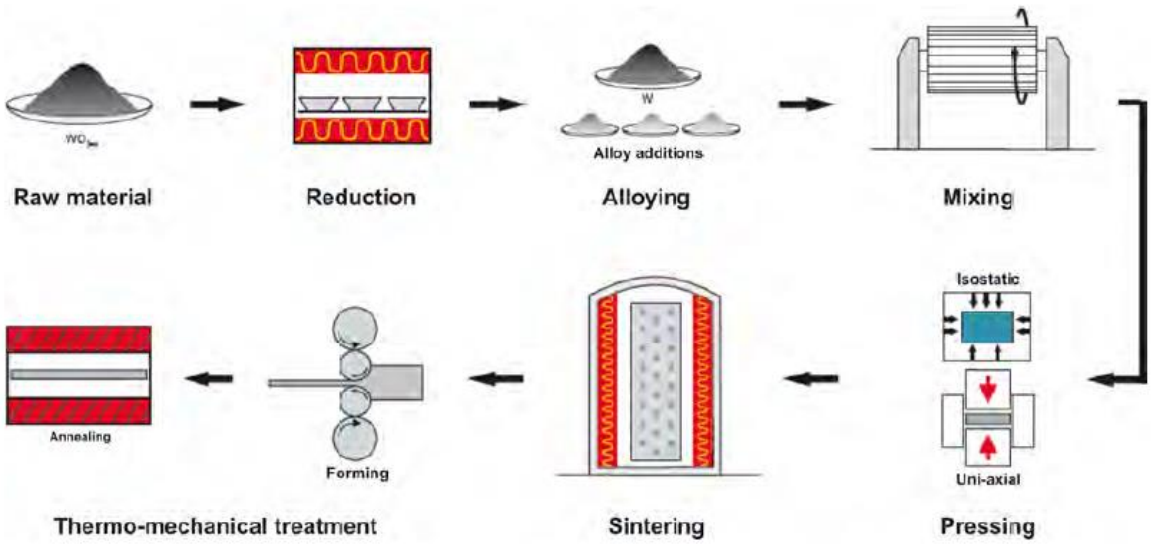

Figure 24. Standard powder metal processing similar to the one used for the manufacturing of the experiment samples [23]

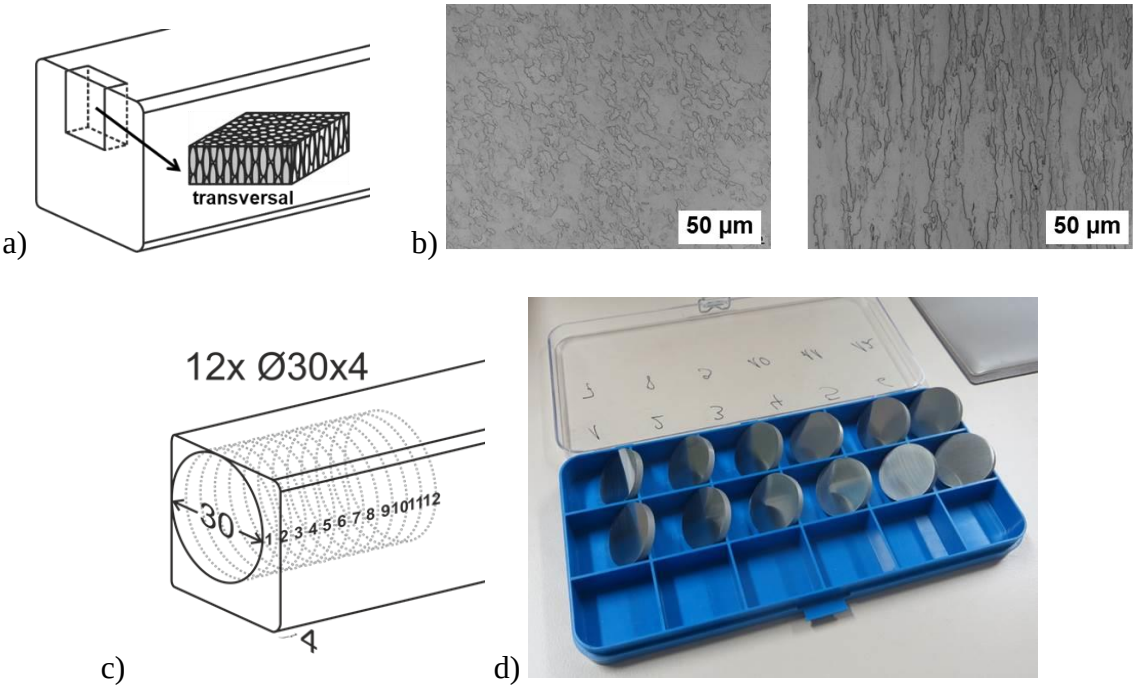

Figure 25. a) Schematic of transverse cut for correct grain orientation, b) transverse and rolling views of microstructure of said cut, c) cut schematic for experiment and d) tungsten samples supplied for H plasma loading experiment [40]

5.2 Equipment

Aside from the previously mentioned Magnum PSI plasma linear device described in section 2.5, for control purposes two samples were exposed to heating inside a furnace, to be able to compare directly material from the same source being exposed to equivalent temperatures with and without plasma. For each of the plasma exposed samples, in situ data was collected from the instrumentation available at the Magnum-PSI facility with the following diagnostic tools:

- *Fast Infrared (IR) Camera:* Makes high frequency measurements of the target's temperature (T_{base} and T_{pulse}).

- *Spectro - Pyrometer:* Measures T_{base} and its tolerance (error) independently of the sample's emissivity (ε). Data used in tandem with IR camera's data to determine ε and temperature changes throughout the exposure.

- *Time Resolved Thomson Scattering (TRTS):* Measures electron temperature (T_e) and electron density (n_e) used for ion flux density (n_i), power density and energy density calculations.

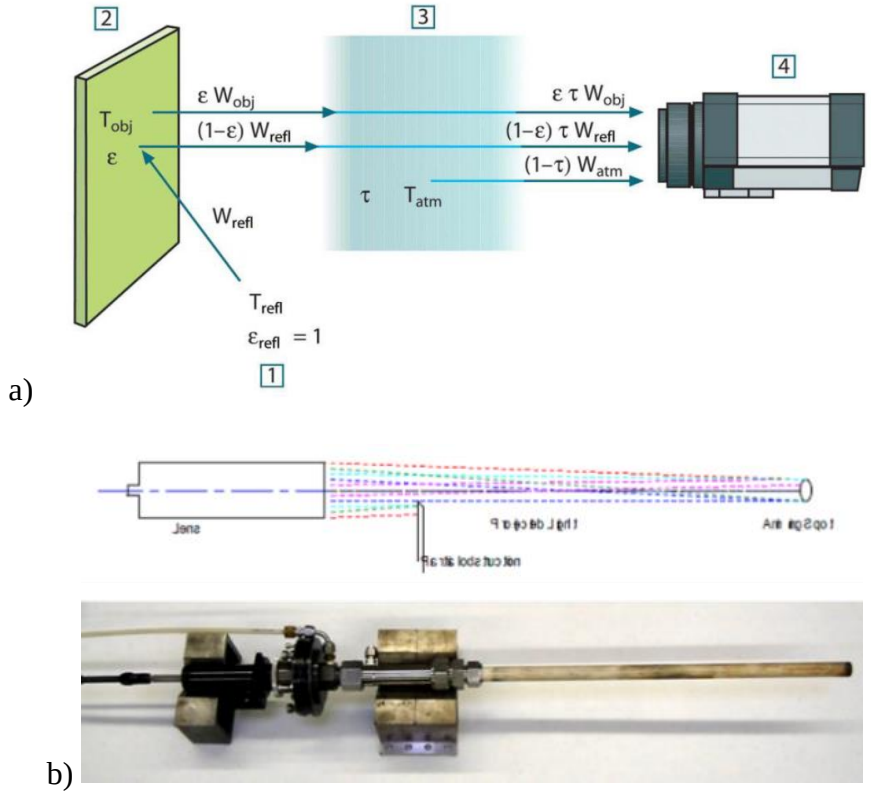

Figure 26. Schematics for working principles of the a) Fast IR camera and the b) Spectro-pyrometer used in this work

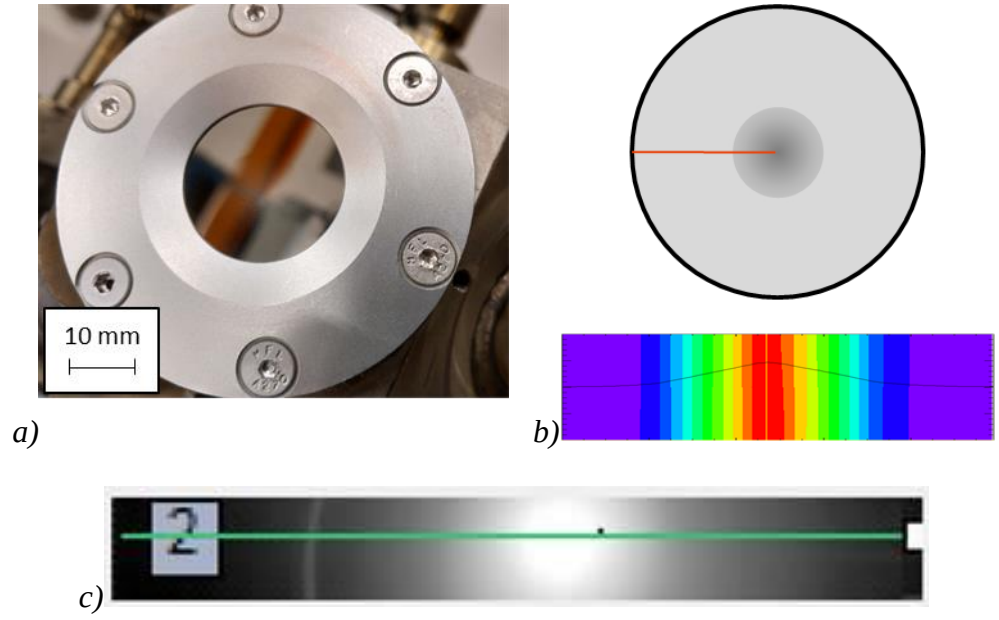

Figure 27. a) Mounted target sample for Magnum PSI experiment, b) schematic of intended radial profile showing temperature distribution mapping along sample c) IR camera snapshot showing typical measurement profile during exposure recording.

After the samples were exposed, post mortem measurements were carried out to study the effects of the different types of exposure they were subjected to. Analyses were first carried on the surface of the disks, followed by metallographic analysis through a cross-section of the exposed target to compare surface and bulk properties with the following tools:

- *Scanning Electron Microscope (SEM):* Identification and analysis of microstructural features on surface and cross-section.
    - *Secondary Electrons (SE):* Analysis of surface morphology characteristics (recrystallization, grain growth, melt, sputtering, crack formation, etc.…)
    - *Electron Backscatter Diffraction (EBSD):* Crystallographic characterization of samples (grains, brain boundaries, texture, etc.…)
- *Light Microscope:* Visual analysis of surface and bulk morphology.
- *Microhardness:* Vickers hardness measurements to assert degree of recrystallization along affected areas.

To analyze and correlate the data collected from the diagnostic equipment, and derive meaningful calculations from it, the following processing tools were used:

- *Altair Software:* It is the IR Camera's native data collection software. Provides full recording of raw data processed to output high frequency temperature. Emissivity is a manually adjusted parameter.
- *nView:* Magnum PSI software. Provides timestamped full recording of emissivity independent temperature from pyrometer. Provides also timestamped recording of the pyrometers' recording tolerance which is temperature dependent. Data is collected at low frequency compared to ELM pulses.
- *Matlab:* Numerical computing environment used for designing routine codes capable of extracting and integrating the raw collected data from diagnostic tools. Pulse analysis, temperature distribution and comparison, heat and particle flux, and energy density calculation routines were developed for this project.
- *Mecway:* Finite Element software used to simulate temperature and heat flux distributions inside the samples' bulk, using surface collected diagnostic data as initial and boundary conditions.
- TMAP7: (Tritium Migration Analysis Program) Software developed by Idaho National Lab for solving the diffusion equations for hydrogen isotopes in materials.

5.3 Experiment Layout

Of the available nine samples, six were chosen for initial exposure in Magnum-PSI, two for furnace heating as controls, and a dummy sample for parameters setting to achieve the desired conditions on the device as well as any unforeseen testing calibration (See Table 2).

Target	Plasma Species	T_{base} [°C]	Pulsed ΔT [°C]	Pulses Frequency [Hz]	Exposure Time [h]	Notes
W1	H	1200	200	5	1	1min high freq. IR recording every 8 min
W2	H	1500	200	5	1	1min high freq. IR recording every 8 min
W3	H	1500	-	-	1	Steady state low freq. IR recording
W4	H	1500	-	-	4	Steady state low freq. IR recording
W5	H	1000	-	-	1	Steady state low freq. IR recording
W6	H	1000	300	5	1	1min high freq. IR recording every 8 min
W7	-	-	-	-	1	Dummy sample for calibration
W8	-	1000	-	-	1	Furnace heated sample
W9	-	1200	-	-	1	Furnace heated sample

Table 2. Experiment layout summary for each sample

5.4 Data processing

The Altair IR camera analysis software requires the sample emissivity (ε) to be declared in order to obtain the correct temperature reading. The pyrometer can detect the recorded ε, an error of ± 0.1, but this gives a sensible starting point to determine the correct value. Since the pyrometer temperature recording is independent of the sample's ε, the temperature along with the measured ε range, are used to calibrate the temperature of the sample at any given snapshot on the IR recording, preferably during a point of steady state loading (no pulses). Sampling resolution should give the same temperature reading on both diagnostic tools during steady state loading. This is because although the pyrometer's resolution, which is around 10 Hz, is not fast enough to independently analyze the simulated ELMs, the IR camera can do so and shows measurement for both steady and transient temperature loading. This data reconciliation is done manually as shown in Figure 28, by identifying matching points between the IR camera and pyrometer data, both using their time stamps and time vs. maximum T_{base} profile.

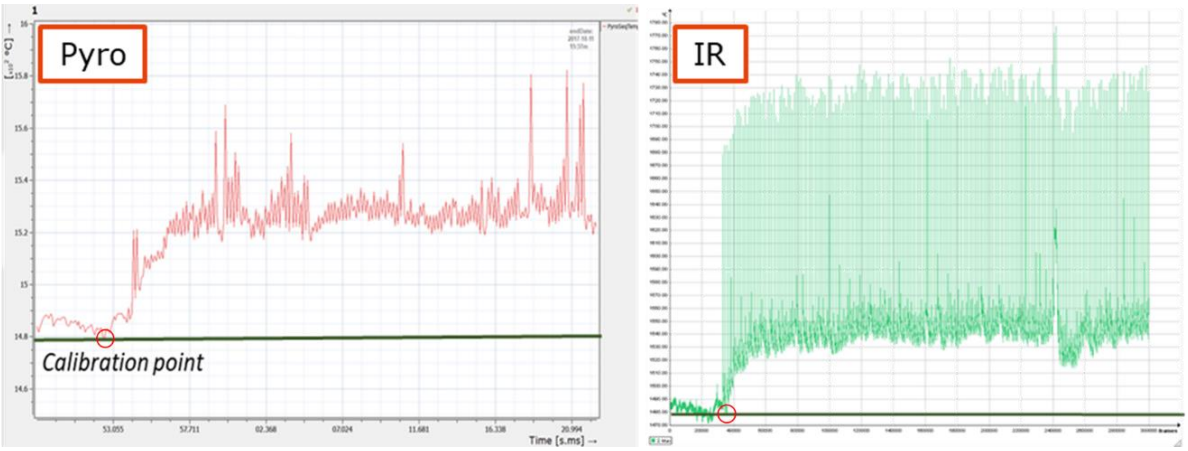

Figure 28. Example of calibration point determination between the two sources, Pyrometer and IR camera software. Emissivity is then adjusted to match both diagnostics.

5.5 Temperature Pulse Analysis

After reconciling IR temperatures to match the emissivity independent reading, the raw data is extracted from both sources by the designed Matlab routine. The first analysis routine is designed to identify the plasma pulses, calculate their actual peak temperature taking into account sampling rate, and to calculate the variation of the pulse peaks through time. At the end of the process, a diametral profile emerges summarizing the average base and peak temperatures over time as shown in Figure 29. The analysis described below is applied for any selected point along the recorded diameter.

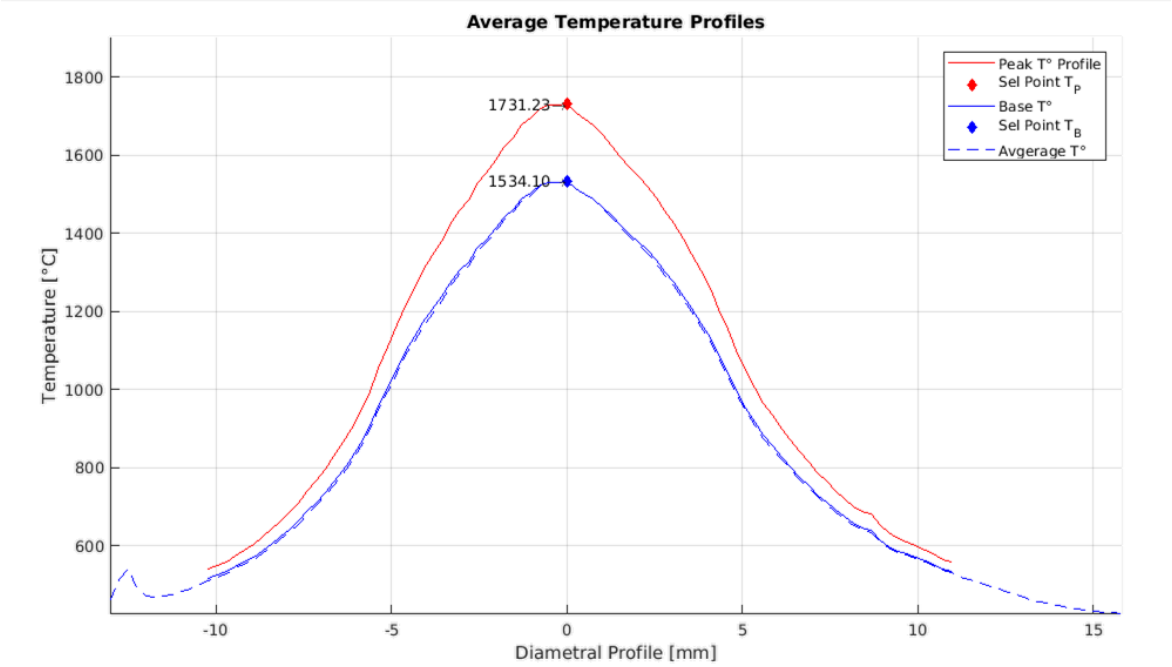

Figure 29. Example of surface diametral profile after pulse analysis highlighting the average base and peak temperature over the analyzed time.

- First, a minimum temperature from where to measure the pulses and a minimum pulse prominence (height from this starting minimum temperature) are used to filter out noise, and thus requires previous knowledge of the experiment's parameters.

- The routine then outputs the location index (first pulse, second pulse, etc.…) of every recorded pulse and its timestamp, paired with the measured temperature of each peak.

- The real temperature of the peak is then calculated. This real temperature differs from the measured one due to the high velocities of the sample rate for the camera and the frequency of the simulated ELMs. This "Peak Calculation and Completion" uses the highest measured peak point, and the nearest two preceding and following data points (five in total) and completes the pulse's shape using a cubic spline that runs through this subset of the data points. The highest point on this completion spline is recorded as the pulse's "True Peak", with the difference between it and the highest measured point for the peak added to the measurement error bar. This process is shown in figures 30 & 31.

- Higher numbers of data points were tested to increase fidelity on the "True Peak" calculation, but offered diminishing returns in terms of accuracy and computation time.

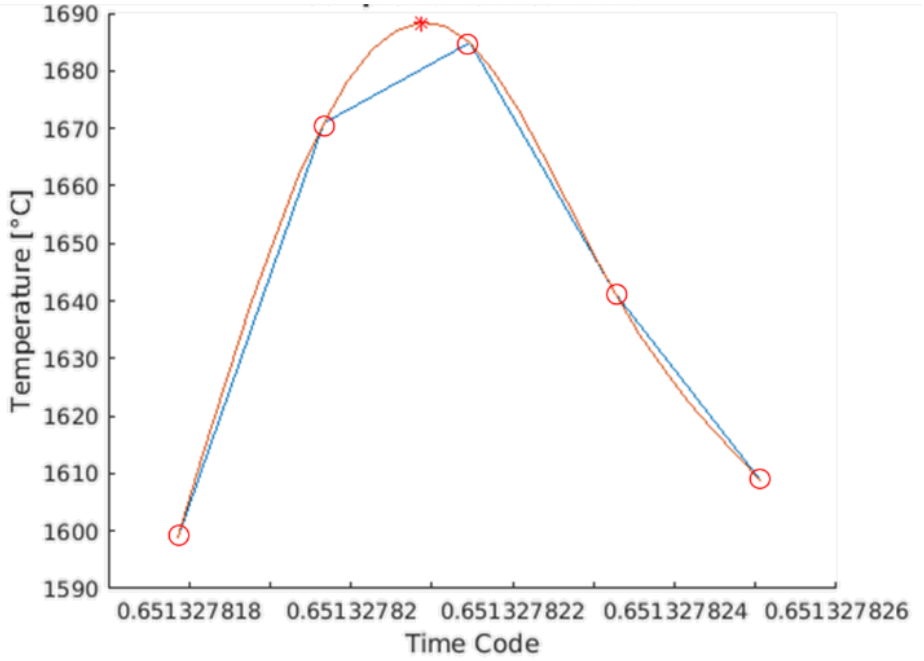

Figure 30. Single pulse completion process. Red circles are the 5 closest points to the peak maximum. A completion cubic spline runs through them and the identified maxima of this spline is recorded as the "true" peak temperature.

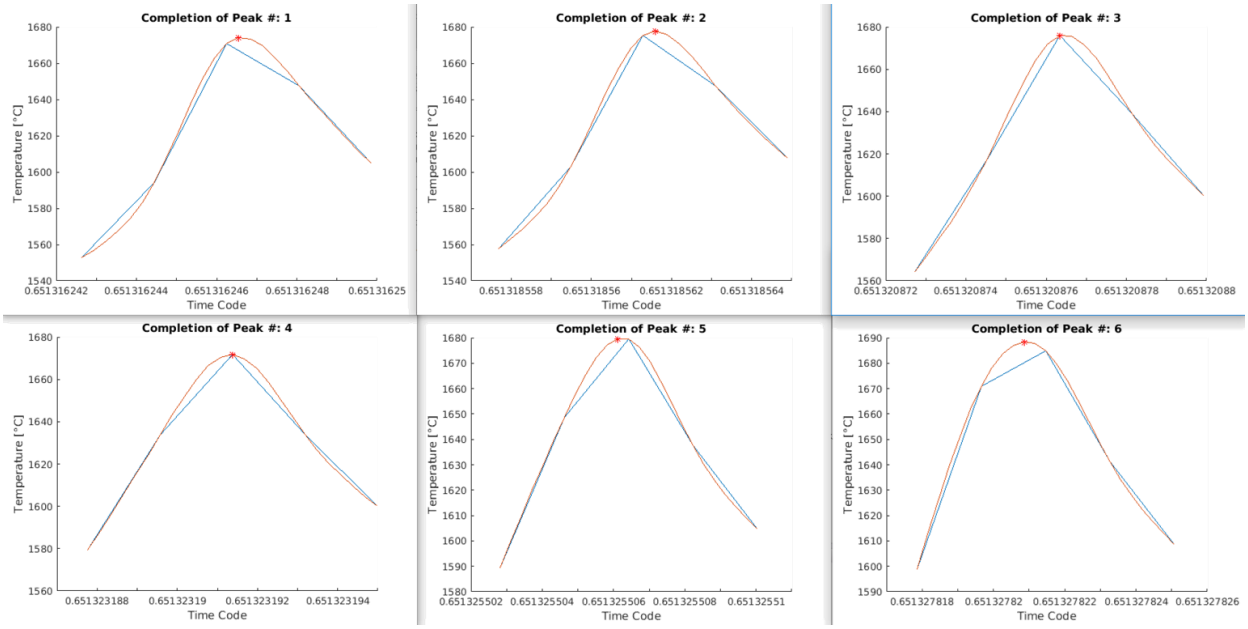

Figure 31. Series of identified peaks' highest points with their corresponding completion spline to illustrate the process with different scenarios of recorded pulse shapes.

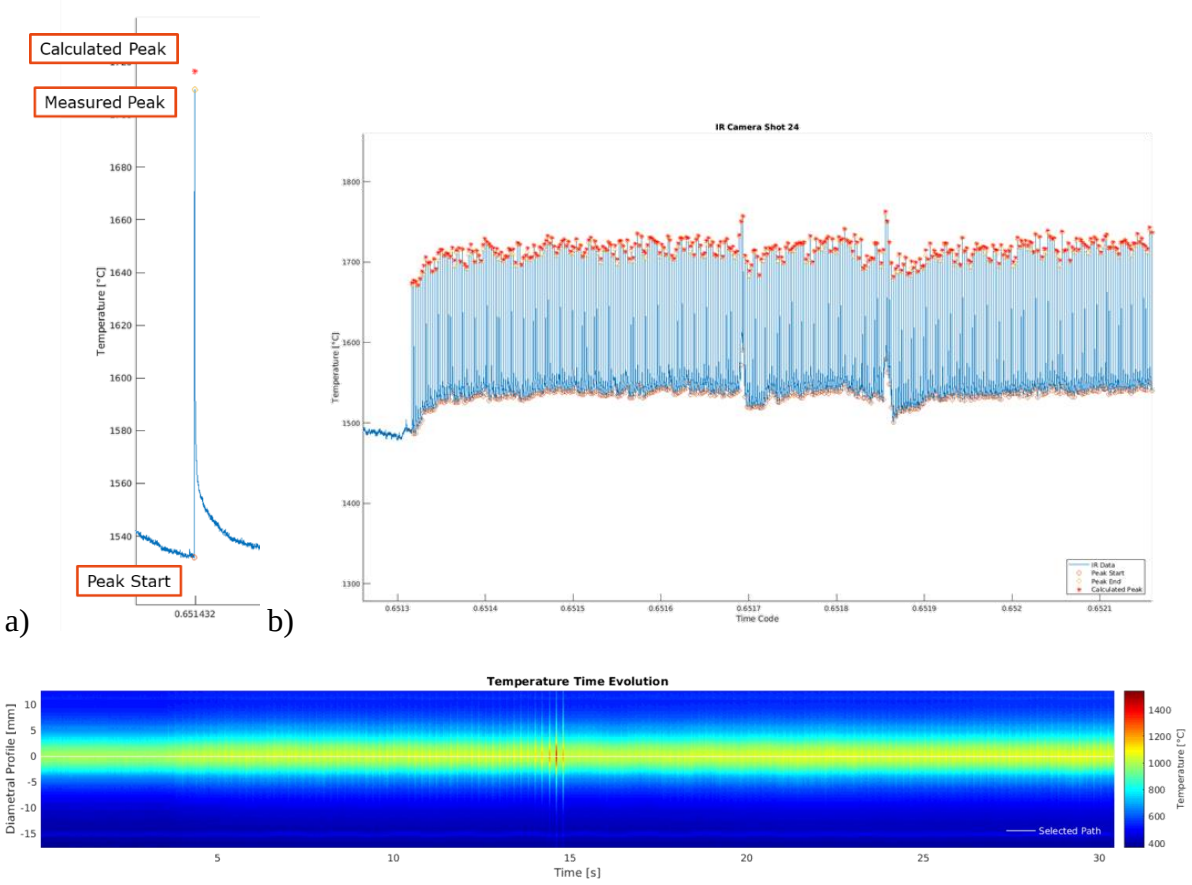

Figure 32. a) Close-up of one full pulse showing its shape, the identified peak's start, its measured and its calculated peak height. b) Assembly of full analyzed IR temperature data set at a specified point in the diameter. c) Processed full temperature evolution through time along the diameter

Having carried out the previous process, the routine takes the calculated and recorded data and compares the base versus peak temperature. Then a trend line is fitted through the data to observe if there is any deviation of ΔT that cannot be explained by the measurement error, thus showing a change in the thermal response of the material to the plasma pulses. These calculated points are defined as follows: (The result for one high frequency snapshot can be seen in Figure 33).

- *Peak - Base Temperature (ΔT)* = Calculated Peak Height (PH_{Id}) – Identified Pulse Start Temperatures (PH_{Calc}) (see Figure 25a)
- *Measurement error* (e_{mPH}) = Resolution uncertainty + Pyrometer tolerance (Diagnostic tools characteristics)
- *Positive error bar*: e_{mPH}
- *Negative error bar*: $e_{mPH} + PH_{Calc} - PH_{Id}$

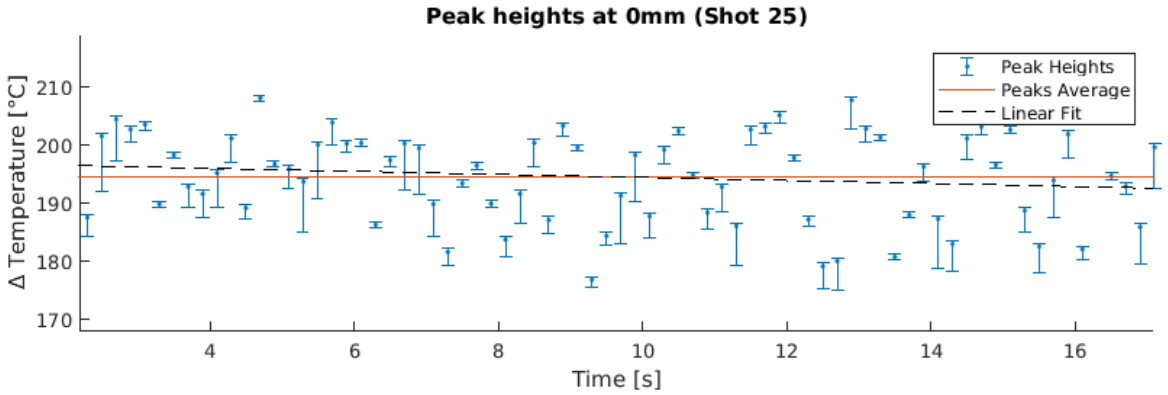

Figure 33. Example of ΔT calculation results with error bars and linear trend line through the mean.

Finally, when all snapshots from a full long exposure experiment have been processed, the variation of the temperature peaks can be cumulatively analyzed to understand the effect of the experiment over the whole timeframe. This overarching analysis encompasses the full response of the sample over time to the temperature loading by superimposing the "discrete" snapshots of the peak analysis, over the full pyrometer recording of the base temperature. It also yields the complete sample of the peak heights vs base temperature with the corresponding error bars, and a linear fit through the data to show the overarching trend, and thus showing if there is a difference of thermal response throughout the whole experiment. Figure 34 shows an example of such cumulative overlay over a point in the exposed diameter.

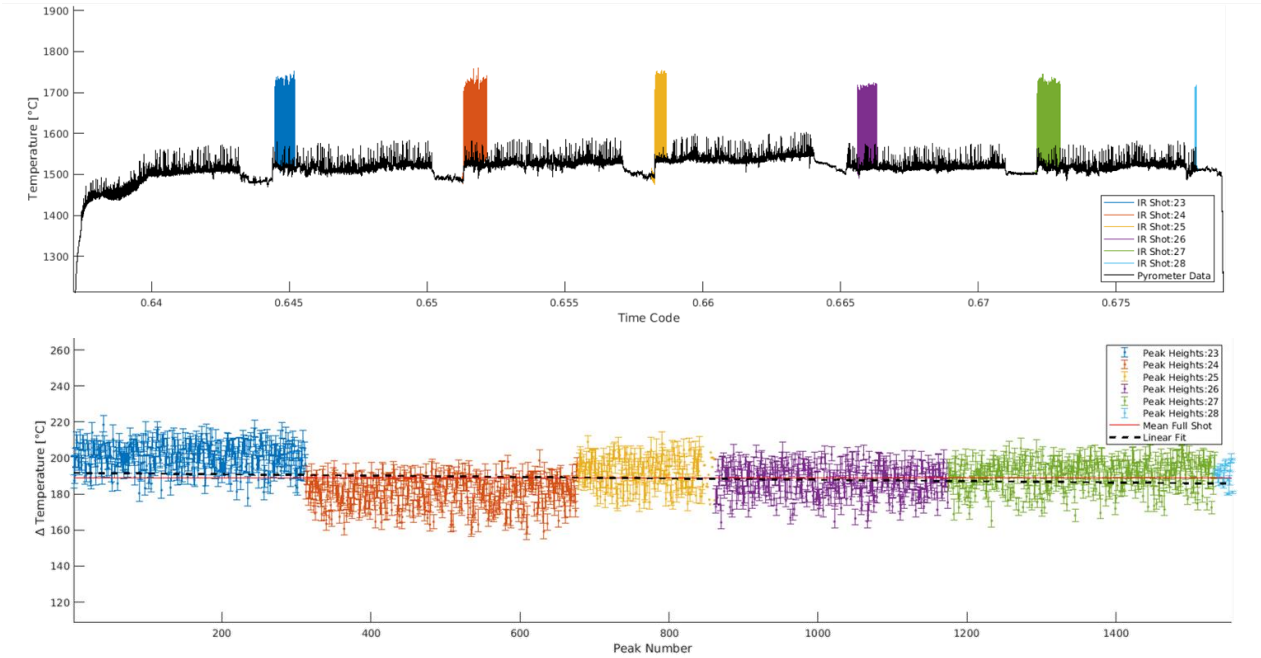

Figure 34. Example of cumulative peak analysis result over a whole exposure

5.6 FEM Bulk Analysis

The IR and pyrometer recordings and the processing of this data is only confined to the surface of the sample. For comprehensive analysis of the effects of H plasma exposure throughout the bulk, a profile of the temperatures and heat fluxes inside the sample is necessary. To achieve this, the experimental setup is recreated in the FEM suite. Since the sample is a disk, and the plasma beam has a circular spot with an intensity that follows a Gaussian distribution, we can model the system by simulating a cross-sectional slice from the diameter of the sample.

The elements simulated are a 4 mm thick tungsten slice exposed to the plasma, a grafoil layer placed for increased thermal contact, a 4 mm thick copper slice of the cooling housing, and a water temperature sink due to the active cooling from the Magnum-PSI setup. The tungsten section is modeled with the finest elements near the surface of the sample, with the smallest elements located near the center of the target having a side length 0.031 mm. The largest elements in the tungsten bulk have a maximum thickness of 0.0875 mm for an accurate temperature and heat map resolution inside of the target. The emissivity of the material was taken from the IR camera analysis, and the temperature dependent mechanical and thermal properties of the materials were taken from the ITER materials handbook [41].

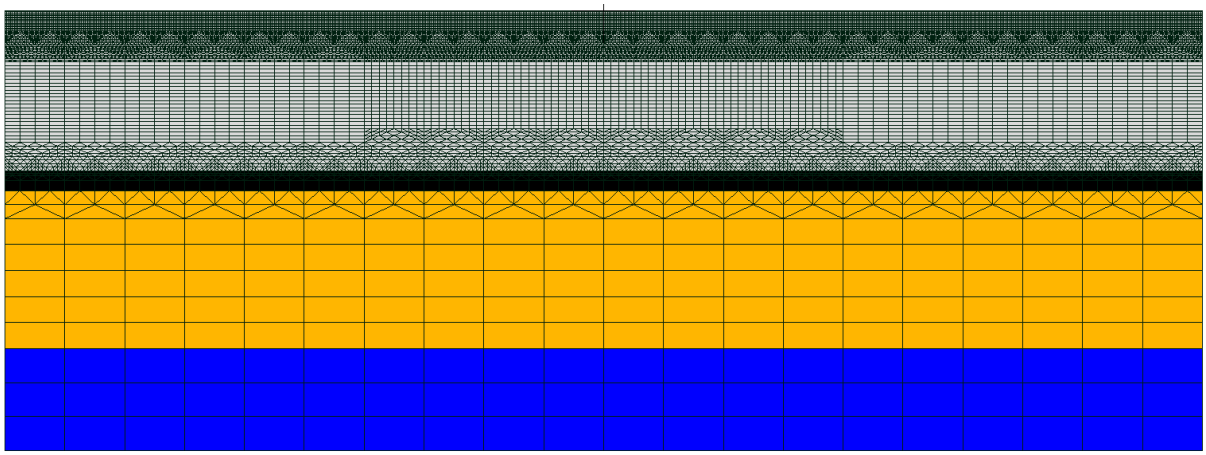

Figure 35. FEM mesh used for bulk analysis. From top to bottom: tungsten, grafoil, copper and water.

Per the experimental setup, running water was used to actively cool the sample, so this was used as a boundary condition and modeled to run constantly at 20 °C. The plasma exposure is made on a vacuum chamber and thus there is no convection of heat dissipation modeled on the outer walls of the model. Since the IR recorded data shows the actual temperature on the sample (not the plasma beam), this temperature profile is used on the surface of the target as a boundary condition as well. With this setup a steady state thermal analysis is run to determine the temperature and heat flux profile in the bulk. These boundary conditions are shown schematically in Figure 36.

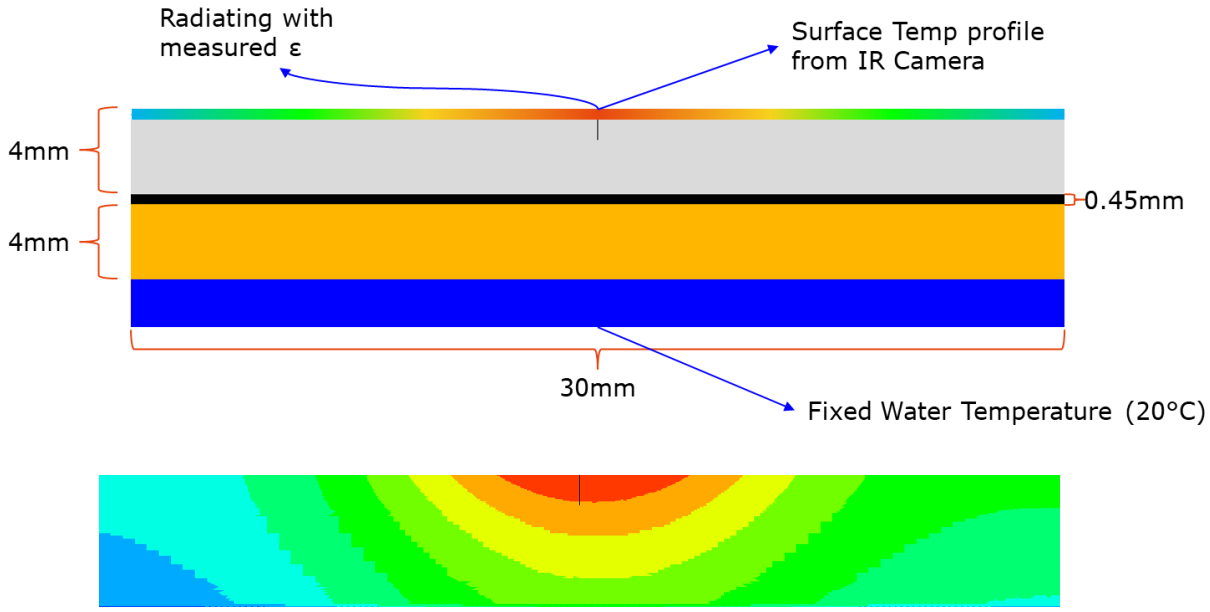

Figure 36. a) Schematic of FEM boundary conditions for Steady State thermal analysis and b) characteristic steady state thermal profile solution of the 4mm W simulated slap

The steady state thermal map of tungsten is then used as starting condition to run a transient (through time) thermal analysis to determine the effect of the pulses on the material. For this, pulses across the diameter are extracted from the surface pulse analysis and used as time varying conditions in the transient calculations. As a result, the extent of the temperature and heat flux penetration of the pulse can be determined, as well as the effective heat flux pulse length (the temperature pulse length is directly measured from the IR camera). This also provides the full picture of these parameters thus the driving input energies in the whole sample. This can be then correlated to any features and measurements across the geometry of the target, and as such set the baseline for the results and conclusions derived from the observations part of this study. Figure 37 shows a snapshot of the results.

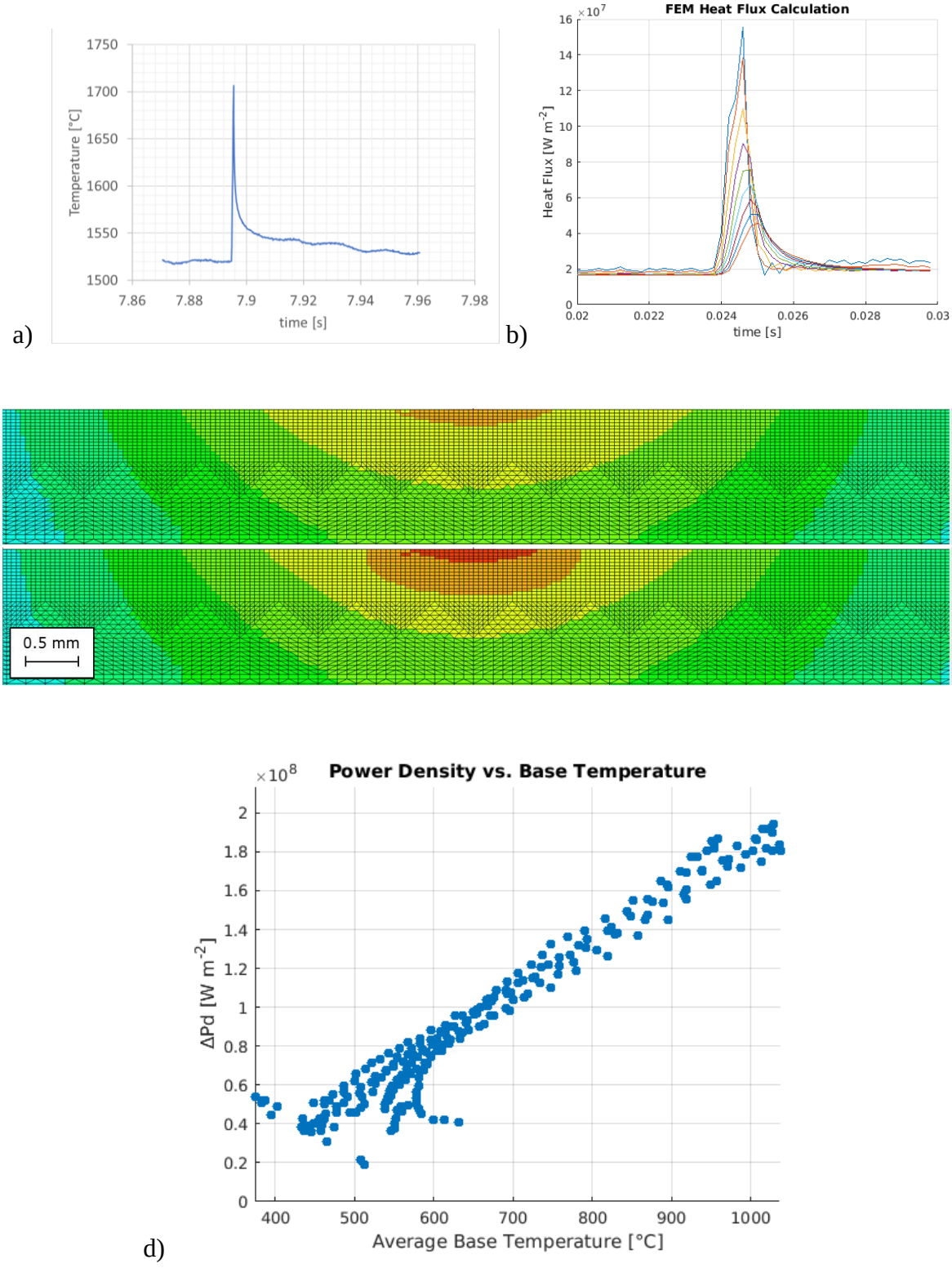

Figure 37. a) IR extracted temperature pulse, b) resulting heat flux pulse through several bulk layers (magnitude decreasing with depth) and c) effect of temperature pulse (before and during maximum intensity) across a slice of the bulk and d) correlation between base temperature and peak heat flux across the exposed surface of a sample.

5.7 TMAP7 hydrogen Concentration Analysis

TMAP7 models diffusion and trap interactions of hydrogen as it disperses trough the tungsten. The code uses a 1D model where the thickness of the material is simulated as layers which increase in separation with the material's depth. Each of these layers is associated with a temperature which has been previously calculated in the FEM analysis. The hydrogen influx is modeled with input collected from the Thomson Scattering at the strike point. The necessary values are the hydrogen's T_e, n_e and, the surface's time to reach a steady base temperature when the exposure starts. Particle flux (Γ) is calculated using the Bohm Criterion in equation 5.1, where m_i is the hydrogen's mass and γ is the adiabatic index. With these parameters, a mobile concentration of hydrogen between layers due to the concentration gradient is calculated. [30]

$$\Gamma = \frac{n_e}{2}\sqrt{\frac{k_b T_e(1+\gamma)}{m_i}} \tag{5.1}$$

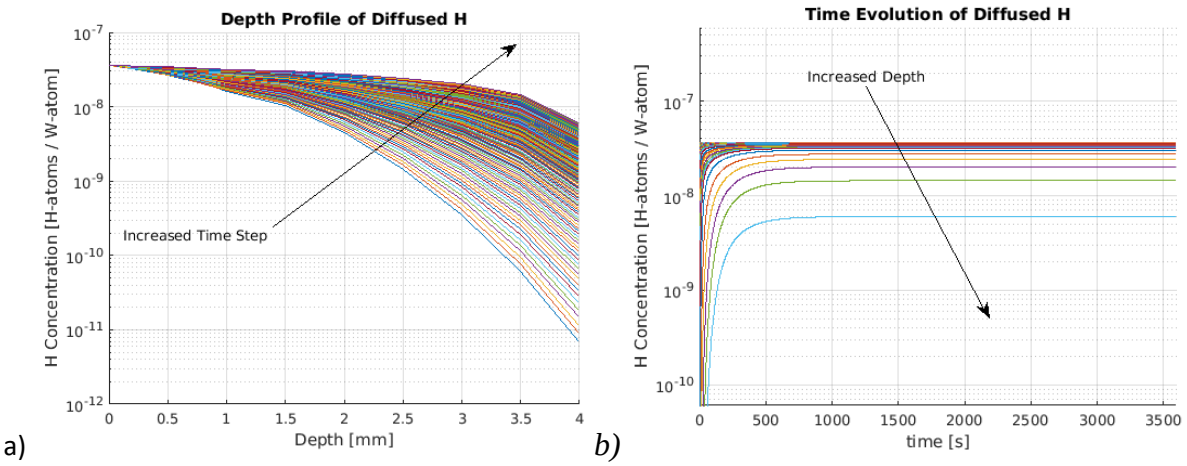

a) *b)*

Figure 38. a) Example Thomson Scattering data used as input, and b) processed TMAP7 output showing hydrogen concentration through time across different layers of the material

6. Results

6.1 Surface Thermal Shock Response

As detailed previously, three targets were loaded in Magnum PSI with simulated ELMs at 5 Hz for 1 hour. IR recording frames were taken at 6418 Hz every 8 minutes for a duration of 1 minute each. The measurements for the initial shot of each target (first 10 minutes of exposure) were discarded due to high measurement error on the pyrometer tolerance, and thus an inability to properly calibrate the IR recording for the shot; after that, the pyrometer tolerance stabilized for the rest of the exposure, providing reliable measurements for reconciliation with IR camera data.

Surface SEM imaging of the targets was performed to map the damage morphologies and correlate their location in the target (with respect to the identified beam strike point) with the corresponding base temperature and pulse height along the diameter. This analysis leads to mapping the identified damages along the target in a Power Density vs. Base Temperature map as it is customary in the literature.

6.1.1 Sample W1 [1200 °C Base + 200 °C Pulses]

The mean base temperature measured for W1 was 1258 °C with ΔT 213 °C at the beam's strike point. Figure 39 shows the average temperature distributions, as well as the different snapshots recorded during the exposure, and the superimposed IR and pyrometer data.

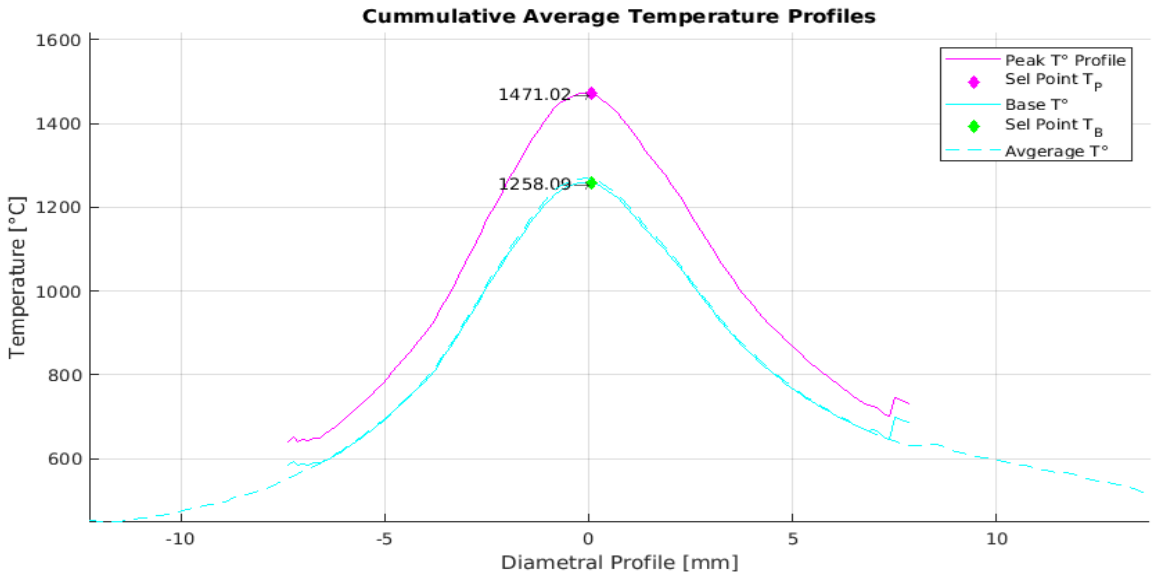

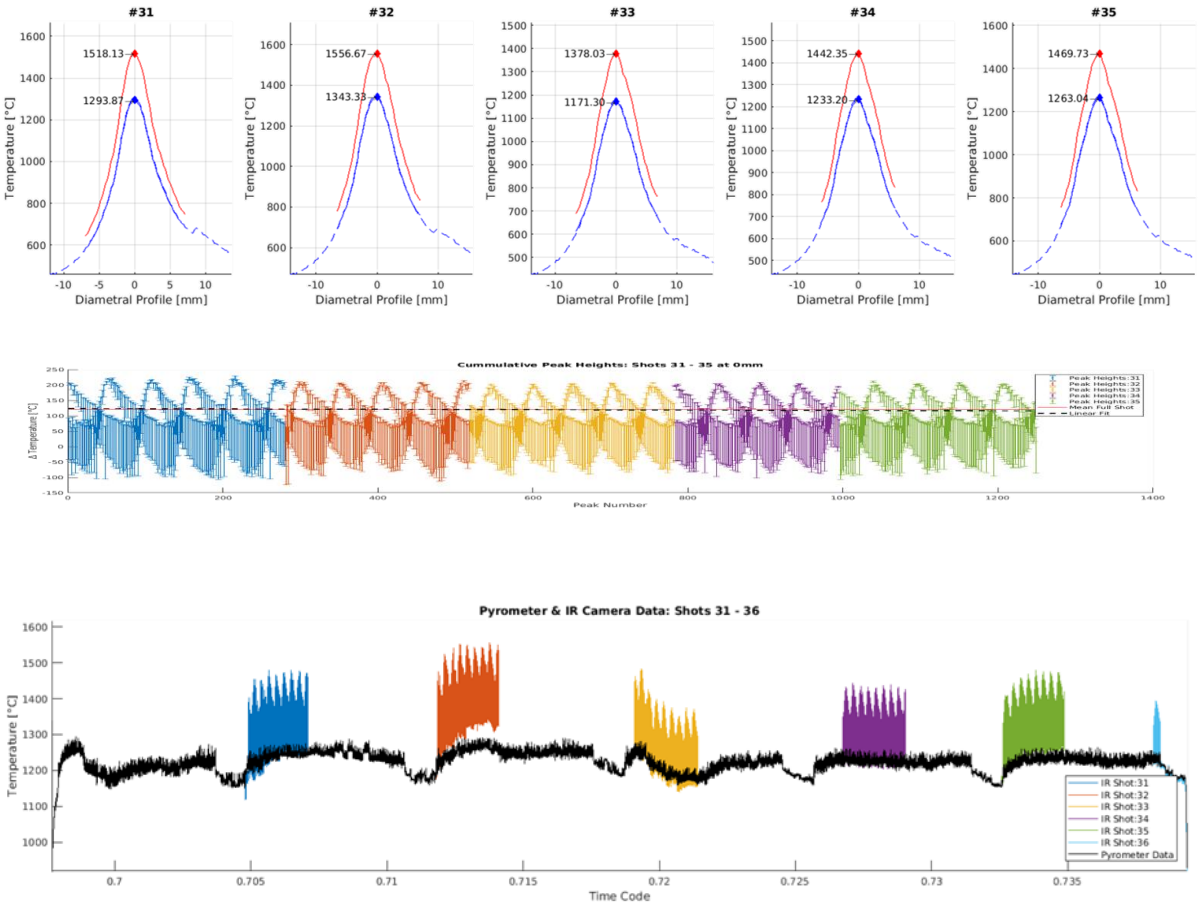

Figure 39. W1 Temperature distributions along radius and through time of exposure

The pulse analysis shows that the pulse temperature (ΔT) during the simulated ELMs keeps constant within the expected variance throughout the shot. This means that the thermal properties of the surface were unaffected during the exposure. Continuing with the power density analysis, a pulse length of ~2 ms and a maximum heat flux of 150 MW m^{-2} are identified. The FEM transient analysis also shows that at it maximum intensity point, there is no thermal change larger than 150 °C below 0.21 mm.

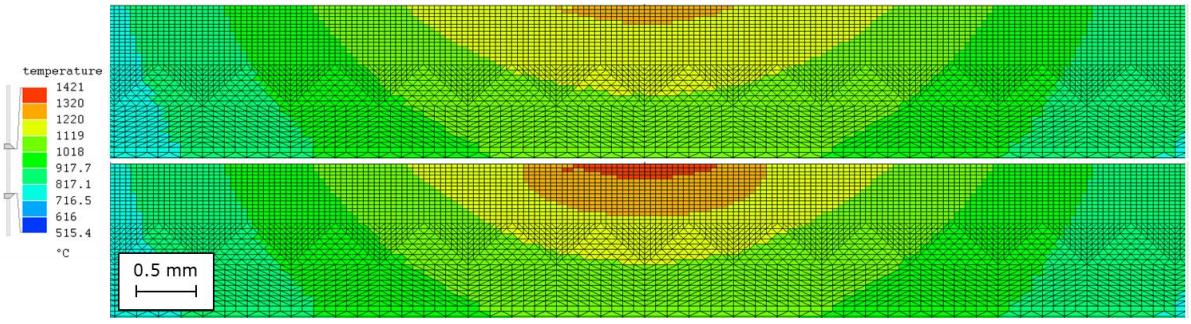

Figure 40. W1 Pulse temperature penetration of 0.21 mm of at least 150 °C temperature increase at the maximum intensity point

After SEM imaging, extensive surface damage can be observed on the sample, with crack networks and damage diminishing as distance from center extends. The damage mapping for this sample was done on 2 sets, one around the strike point, and one moving radially away from it with magnifications varying from 23x to 5000x. This mapping is shown in Figures 41 and 42.

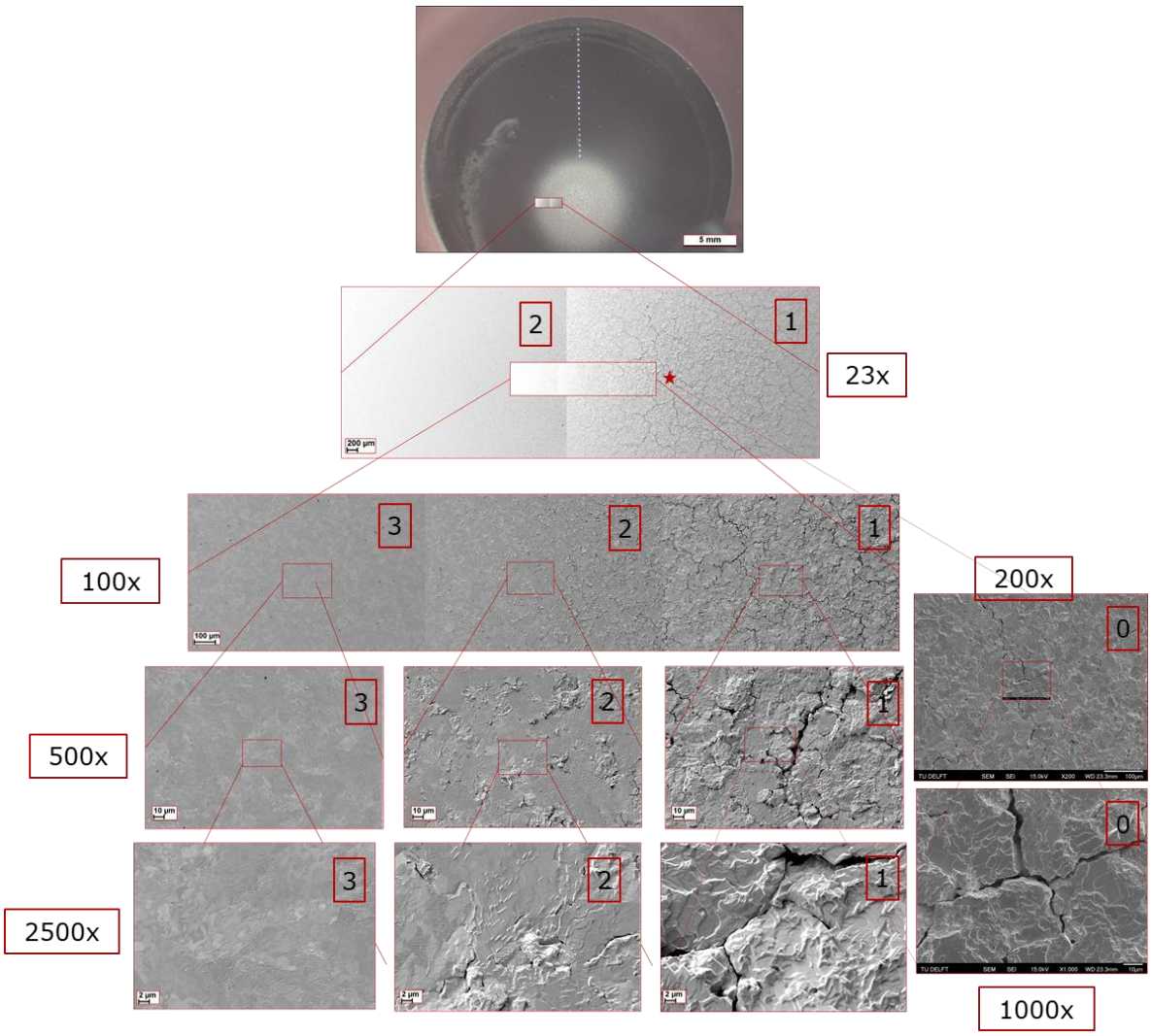

Figure 41. W1 SEM imagining of near-center area damage morphologies

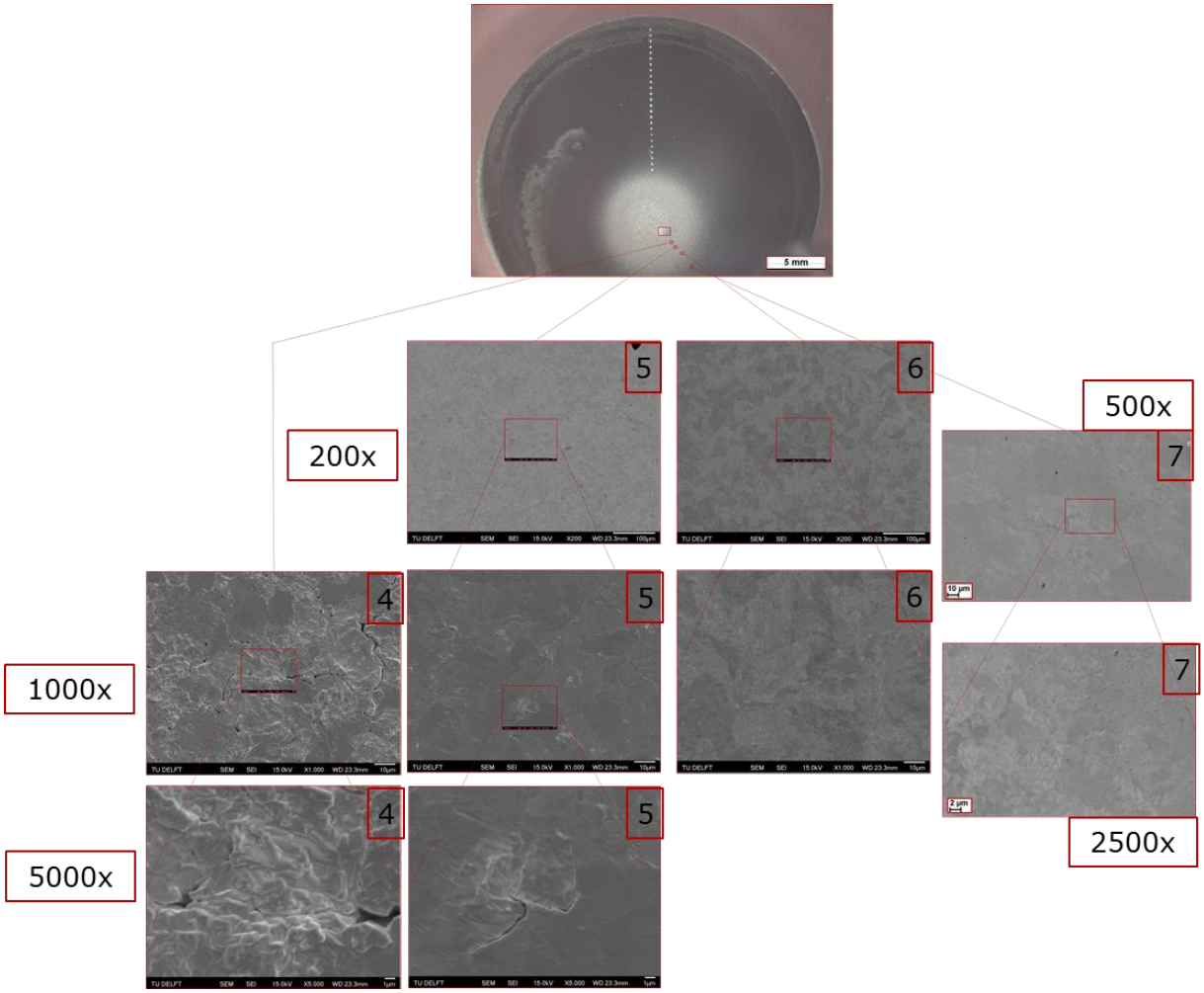

Figure 42. W1 SEM radial imagining of damage morphologies

Surface damages were categorized as described in Section 3.3, and mapped to the corresponding temperature vs. power density point along the target (shown in Figure 43). Of note is the addition of blistering, particularly in the low end of the spectrum (both temperature and power density wise) which was not typified in the existing literature as part of this type of damage assessment [23]. Even though there is some scatter in the data points, the power density shows a positive trend with increasing temperature, and as they increase, the dominating damage type becomes a more severe type of failure.

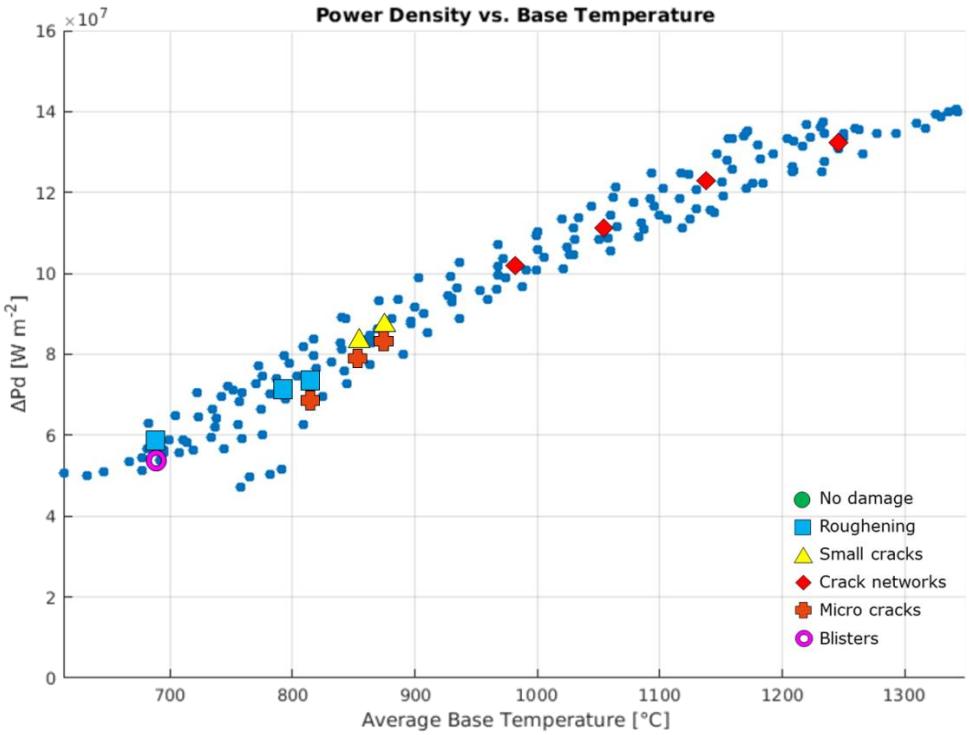

Figure 43. W1 Thermal shock response damage mapping

6.1.2 Sample W2 [1500 °C Base + 200 °C Pulses]

The mean base temperature measured for W2 was 1530 °C with ΔT 195 °C at the beam's strike point. Figure 44 shows the average temperature distributions, as well as the different snapshots recorded during the exposure, and the superimposed IR and pyrometer data.

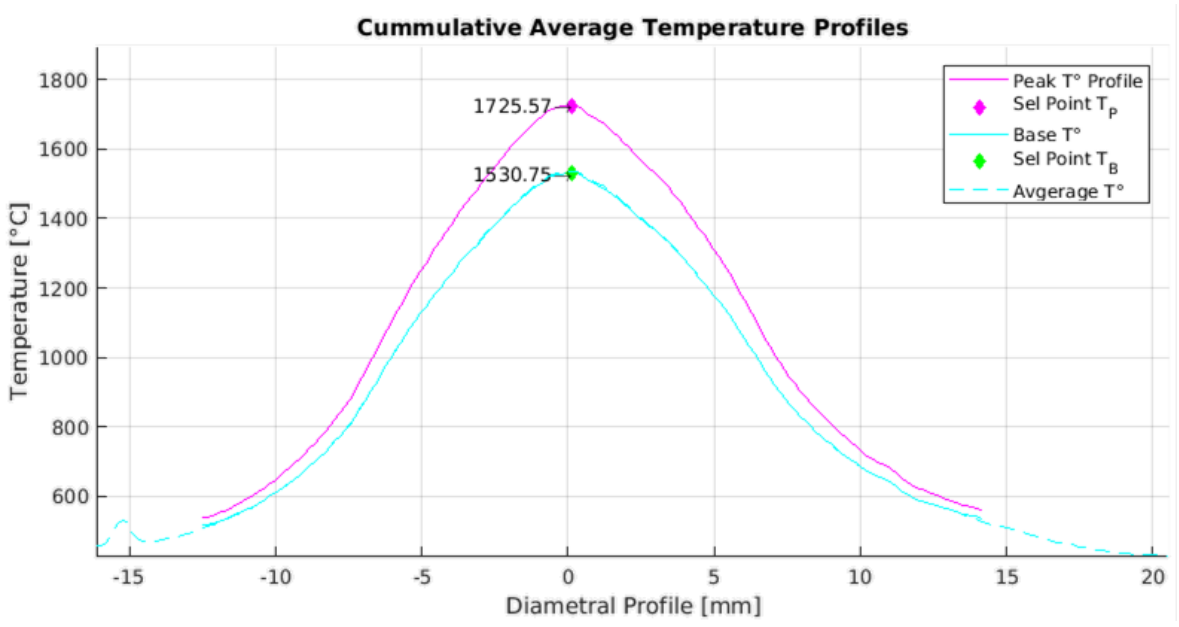

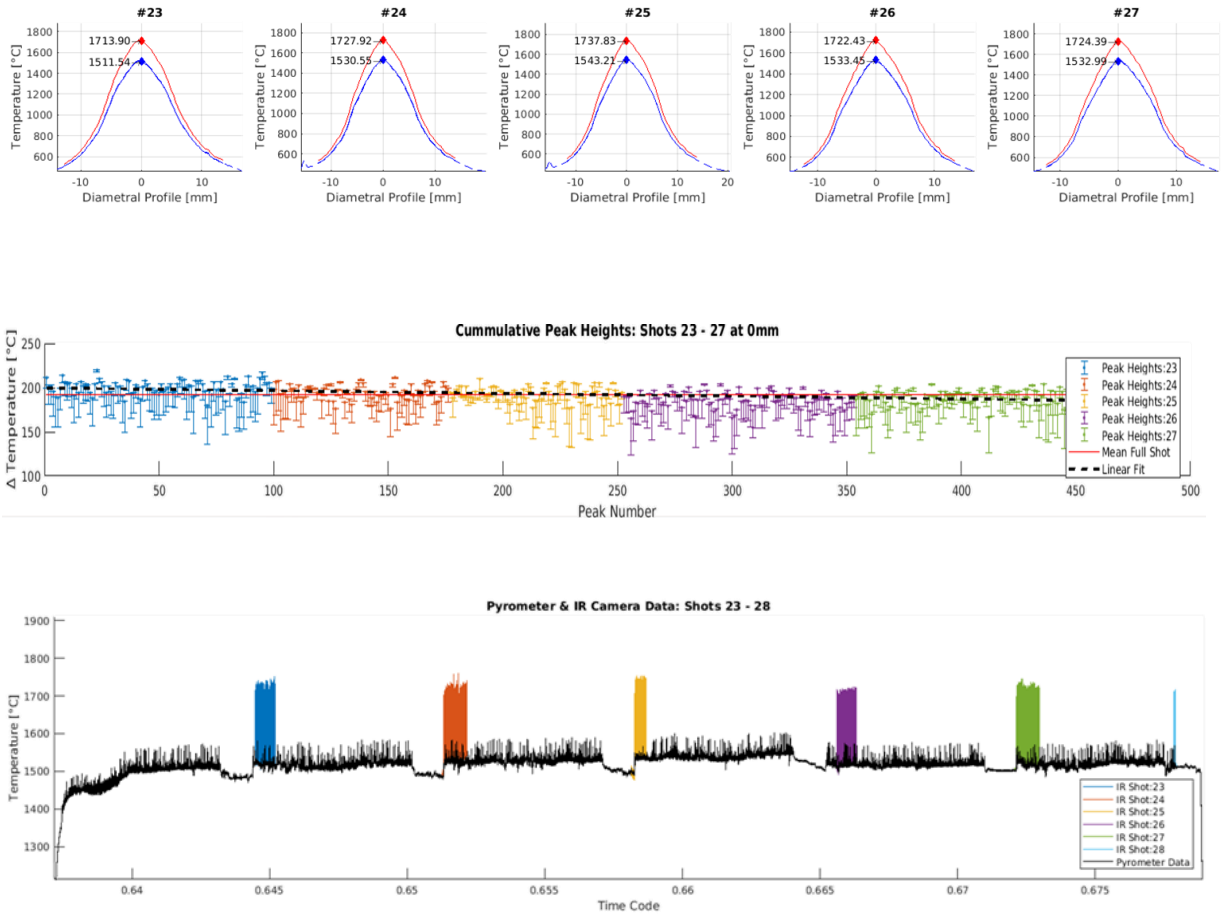

Figure 44. W2 Temperature distributions along radius and through time of exposure

The pulse analysis shows that the pulse temperature (ΔT) during the simulated ELMs is constant within the expected variance throughout the shot, showing that the thermal properties of the surface were unaffected during the exposure. The power density analysis shows a pulse length of 1.6 ms and a maximum heat flux of 155 MW m^{-2}. The FEM transient analysis also shows that at it maximum intensity point, there is no thermal change larger than 150 °C below 0.3 mm.

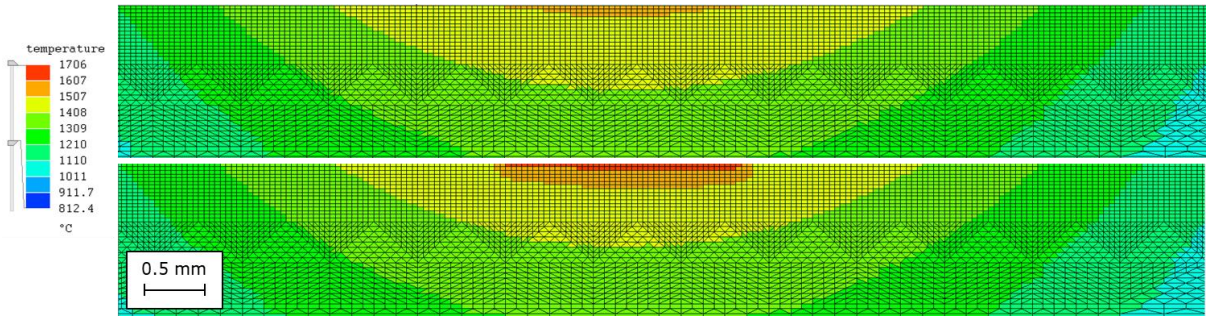

Figure 45. W2 Pulse temperature penetration of 0.30 mm of at least 150 °C temperature increase at maximum intensity point

After SEM imaging, extensive surface damage can be observed on the sample, with crack networks and damage diminishing as distance from center extends. The damage mapping for this sample was done on 2 sets, with an overlapping range. Both start around the strike point, but the first zooms into the center structures (Figure 46) and the other one moves radially away from it for about 10mm to assess the change in damage structures (Figure 47).

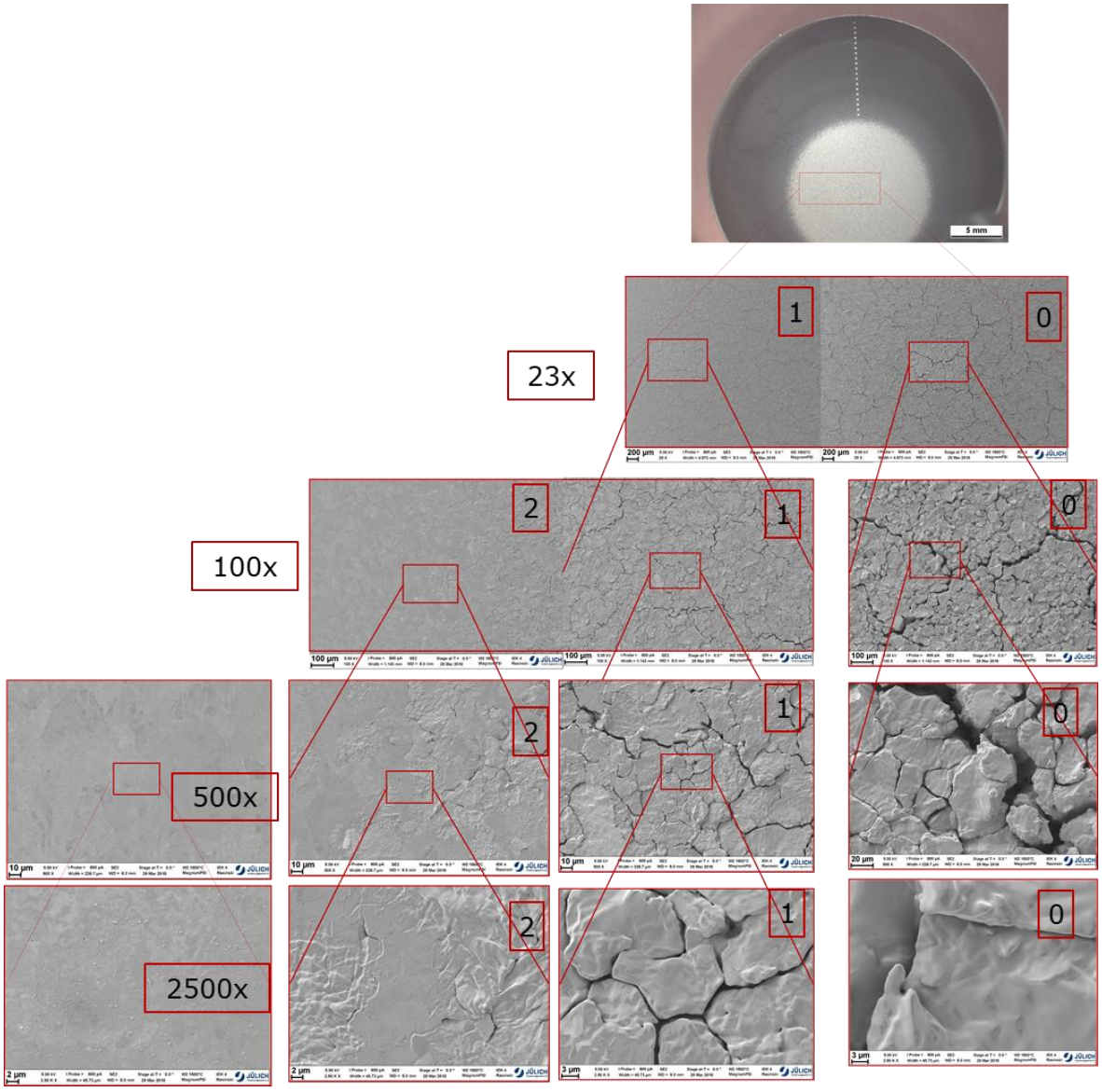

Figure 46. W2 SEM imagining of near-center area damage morphologies

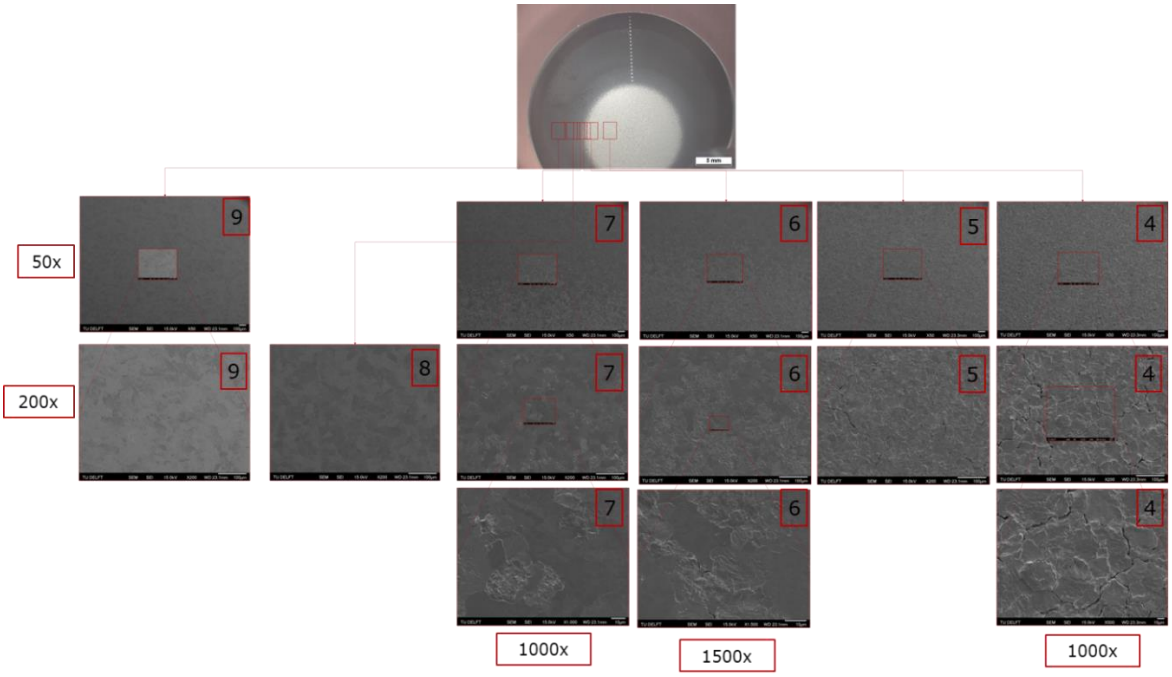

Figure 47. a) W2 SEM radial imagining of damage morphologies

As before, surface damages were categorized as described in Section 3.3, and mapped to the corresponding temperature vs. power density point along the target (shown in Figure 48). No blistering was observed as in the previously examined sample, but some surfaces were categorized as "no damage" which previously was not seen. Again as before, power density shows a positive trend with increasing temperature, and as they increase, the dominating damage type becomes a more severe type of failure.

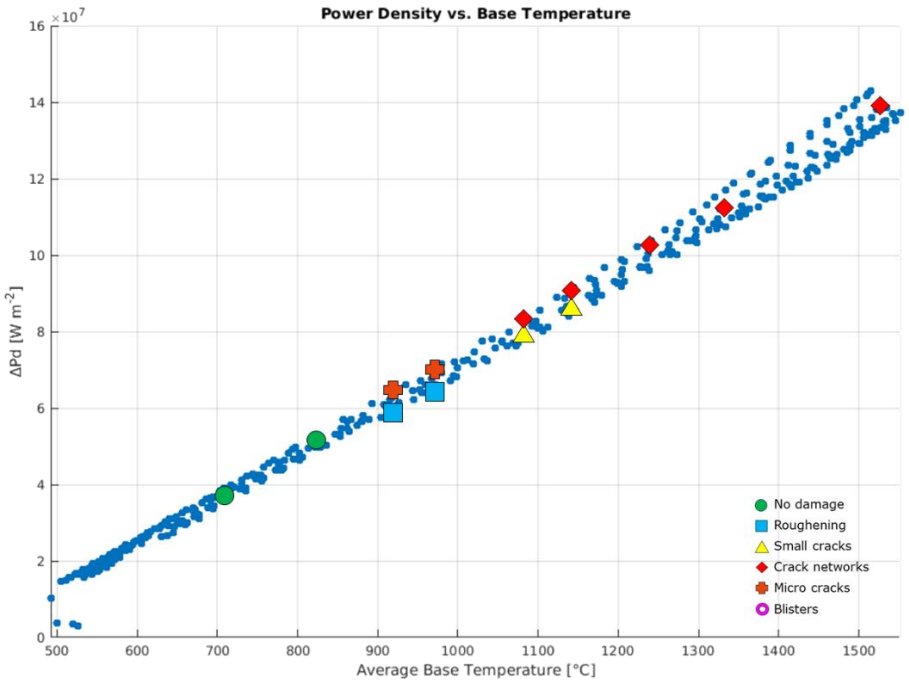

Figure 48. W2 Thermal shock response damage mapping

6.1.3 Sample W6 [1000 °C Base + 300 °C Pulses]

The mean base temperature measured for W6 was 1005 °C with ΔT 330 °C at the beam's strike point. Figure 49 shows the average temperature distributions, as well as the different snapshots recorded during the exposure.

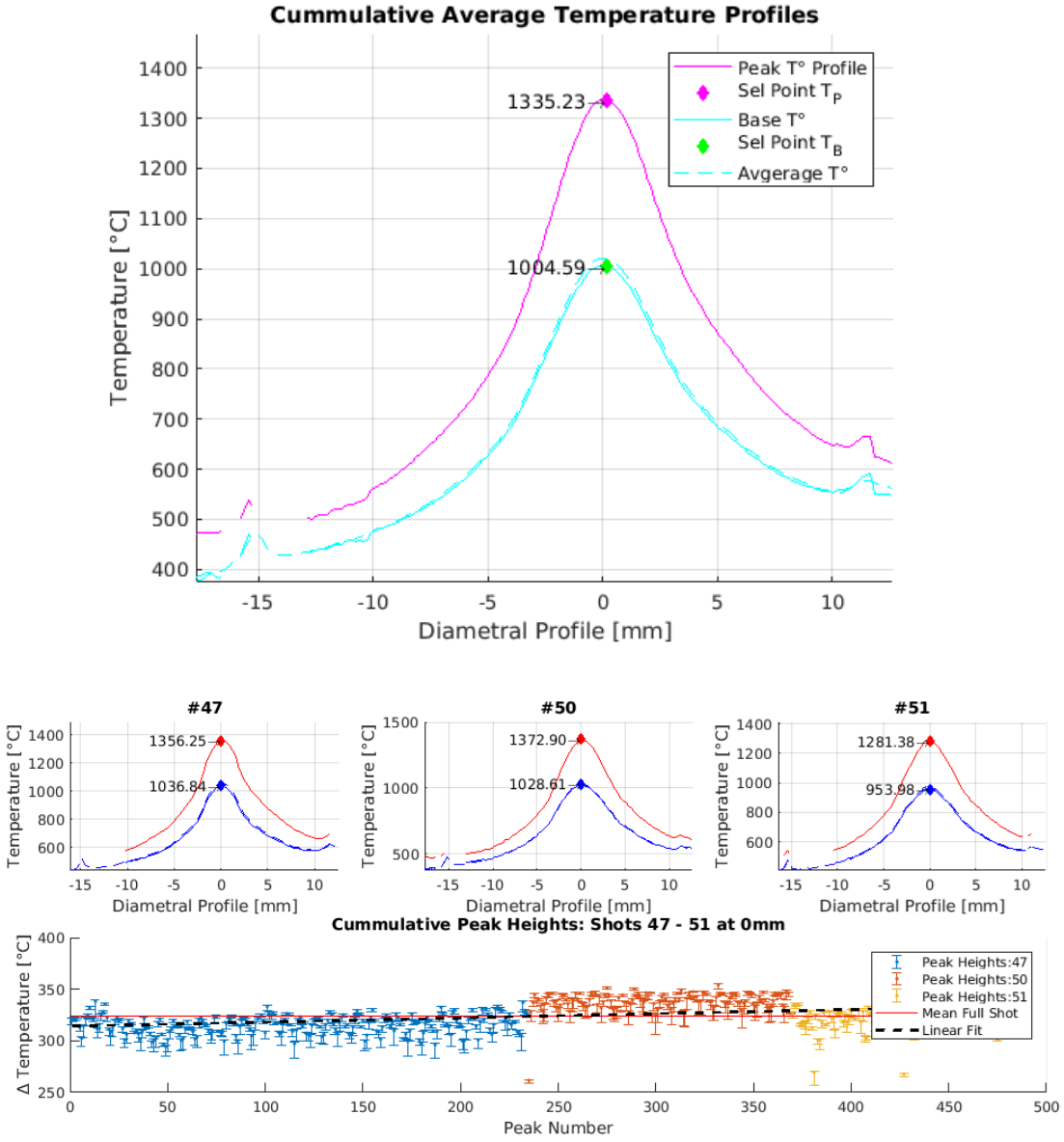

Figure 49. W6 Temperature distributions along radius and through time of exposure

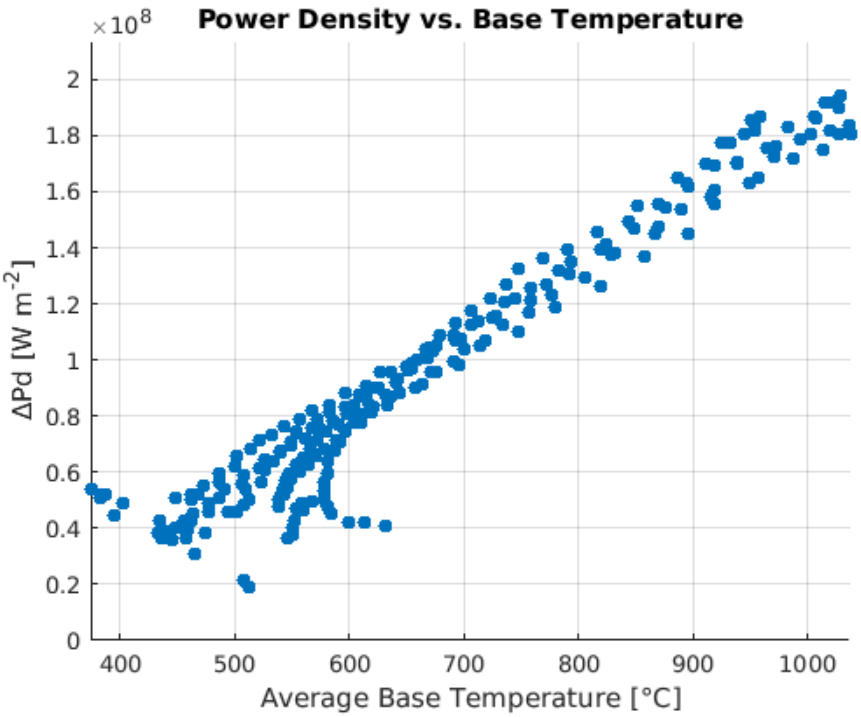

Figure 50. W6 Thermal shock response

The pulse analysis shows that the pulse temperature (ΔT) during the simulated ELMs is constant within the expected variance during the shot. This means that the thermal properties of the surface were unaffected throughout the exposure. During the power density analysis, a pulse length of 3.0 ms was identified and a maximum heat flux of 196 MW m^{-2} was calculated. The FEM transient analysis also shows that at it maximum intensity point, there is no thermal change larger than 150 °C below 0.15 mm.

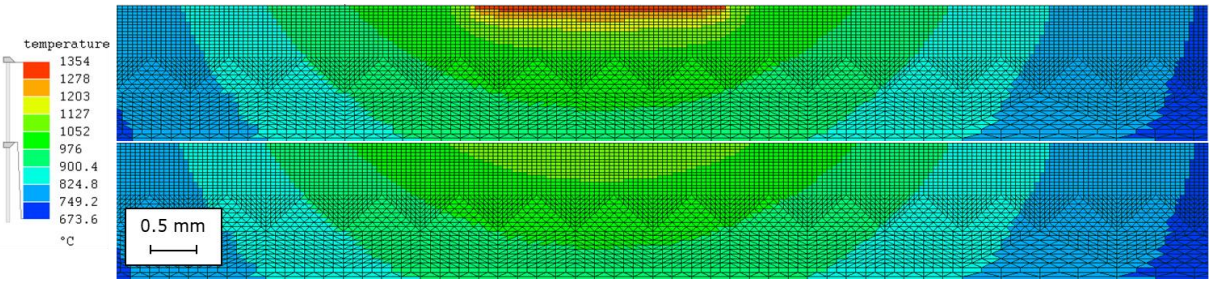

Figure 51. W6 Pulse temperature penetration of 0.15 mm of at least 150 °C temperature increase at maximum intensity point

At the exposure, during the last minute (59 minutes in) the Magnum-PSI plasma source broke down. The machine was immediately shut down, and the incident was deemed unexceptional by the diagnostics team. Nevertheless when the sample was removed from the target holder, a layer of copper had deposited on the surface. Measurements for the diagnostic bench showed a spike in copper and other residual elements such as calcium when the source (machined out of copper) broke down.

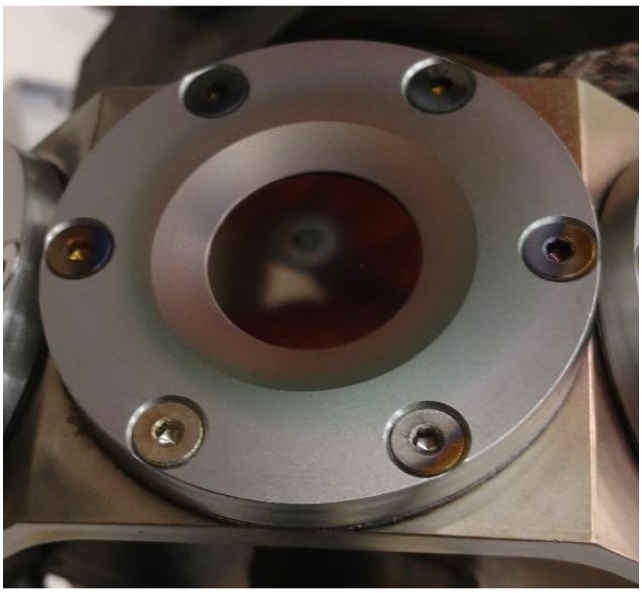

Figure 52. W6 after exposure showing copper colored deposit in the target and the sample holder

Because of this, there is no data for the last planned IR high speed recording, and no surface imaging for W6 was taken as the copper contamination at the end of the exposure may have affected some of the possible features to be observed, and any conclusions derived would be subject to interpretation of the effect of the copper increasing them or hiding them (i.e. crack sizes, networks, etc…). It was agreed then not to do this analysis, as it may have not been reliable.

6.1.4 Summary Surface Thermal Shock Response

Samples W1 and W2 (200 °C ΔT pulses at 1200 °C and 1500 °C base temperatures respectively) had their surfaces analyzed and the damage morphologies stemming from the center of the beam's strike point classified according to established literature [23][24][42]. Sample W3 analysis had to be discarded as the copper surface contamination prevented a reliable analysis to be performed. When overlaying the results from W1 and W2 they seem to follow a similar behavior in their base temperature vs power density excursion with W2 having higher values for power density at equivalent base temperatures.

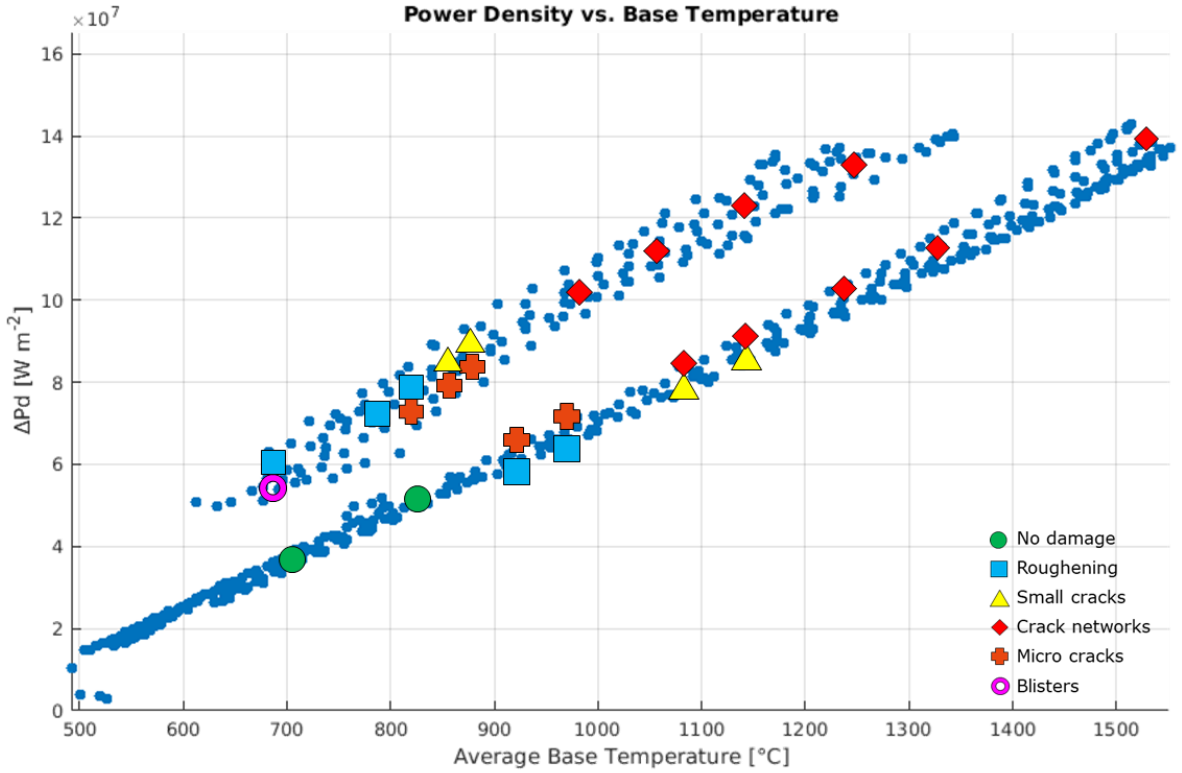

Figure 53.W1 and W2 cumulative damage mapping classification

Upon further analysis in these transient pulsed inputs, the power density is dependent on the heat flux's shape (triangular shape in this scenario), and ΔT. This behavior is governed by Equation 6.1 where P_0 is the power density, τ_t is the total pulse time, and τ_r is the rise time or time for the pulse to reach its maximum intensity [43].

$$P_0 = \frac{3}{4} \cdot \frac{\Delta T \sqrt{\pi \rho c_p (2\tau_t - \tau_r)}}{\tau_t} \tag{6.1}$$

For all pulses, the rise time was very similar at 1 ms. The Gaussian nature of the beam lets equivalent temperatures from both samples to be compared directly, and along the exposures, the observed ΔT of W1 is consistently higher by around 60 °C. Since the ΔT difference between both samples is much higher than the differences in τ_t (which are very similar) it makes sense that this would be the dominant factor in making the absorbed power density higher in W2 at equivalent temperatures. It is worth noting that looking at Figure 50, W6 does not follow this path, and the path it follows has a steeper gradient suggesting a higher difference in ΔT at equivalent base temperatures during that exposure.

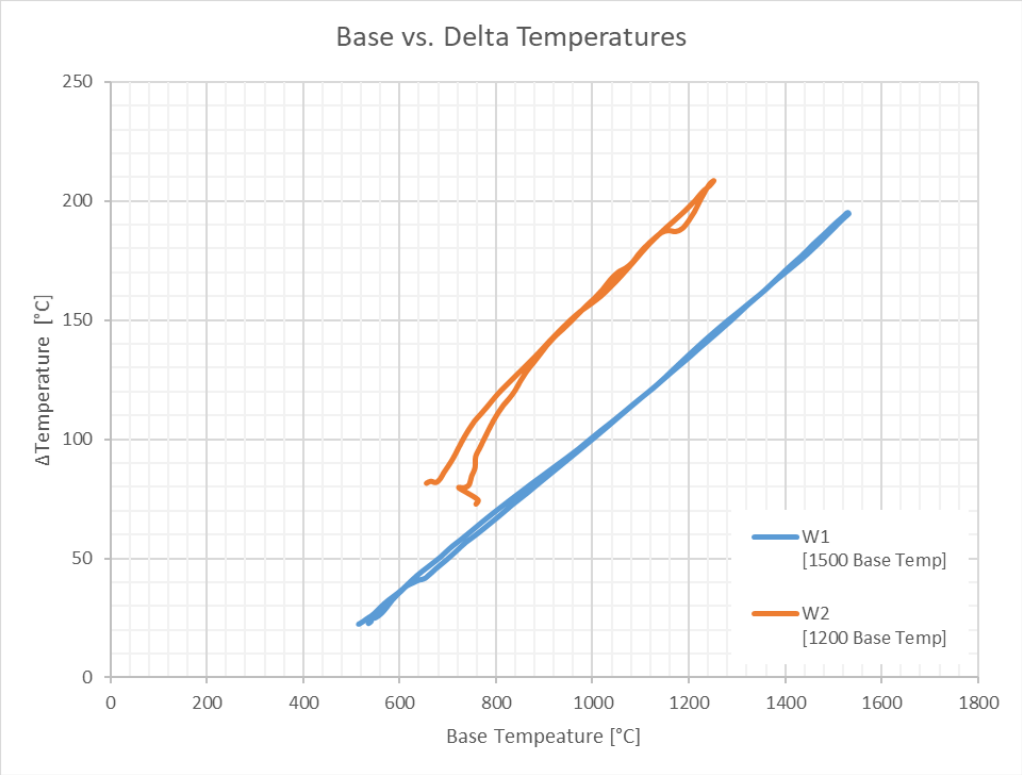

Figure 54. W1 and W2 comparative of measured ΔT at the respective base temperatures. The behavior seen is very similar to the power density vs. base temperature plot in Figure 53.

6.2 Recrystallization Behavior

As mentioned, the main driver for this research is to understand tungsten's recrystallization behavior when exposed to hydrogen plasma under different regimes. Since the unexposed material has a directional grain structure with an elongated refined grain size of 5×25 μm^2, the change from unaffected areas and the non-preferentially directioned recrystallized ones (with a grain size of about 40 µm) can be visually assessed with microscopy. Moreover the hardness difference between the used highly deformed tungsten, and the recrystallized material is in the order of 100 HV, so taking microhardness measurements across the samples' geometries can show the degree of recrystallization of the sample at the points of interest. [17][36][40]

For all plasma exposed samples, hardness measurements were recorded at the surface, then the samples were cut across their diameter. This cross-section was polished and etched with a solution of NH_3:H_2O_2:H_2O at 1:2:7 per volume for about 30 – 40 seconds to reveal the grain structure. With this visual, microhardness measurements were taken along the cross-section as well. All internal measurements were done at least 0.6 mm below the exposed surface to prevent stress fields from the edge to affect the hardness measurement. In turn, this means that the measurements did not record the effects of the pulse thermal field (as this is too shallow as discussed in the previous section). Also, surface hardness measurements from heavily cracked areas (usually near the center of the pulse targets) were not recorded due to their lack of reliability. All hardness measurements were taken at a minimum spacing of 0.5 mm to avoid the stress field caused by previous measurements. The final hardness recordings then were correlated to the temperature map developed from the FEM simulations to provide a full assessment of the recrystallization effect of the experiments.

6.2.1 W8 & W9 Reference Samples

To be able to have a baseline for the plasma exposed samples, three sets of microhardness measurements were taken on samples un-exposed to the plasma source. One set on W8 before any heat treatment, another one on that same sample after 65 minutes in a temperature controlled furnace at 1000 °C, and another one on W9 after 65 minutes in a temperature controlled furnace at 1200 °C.

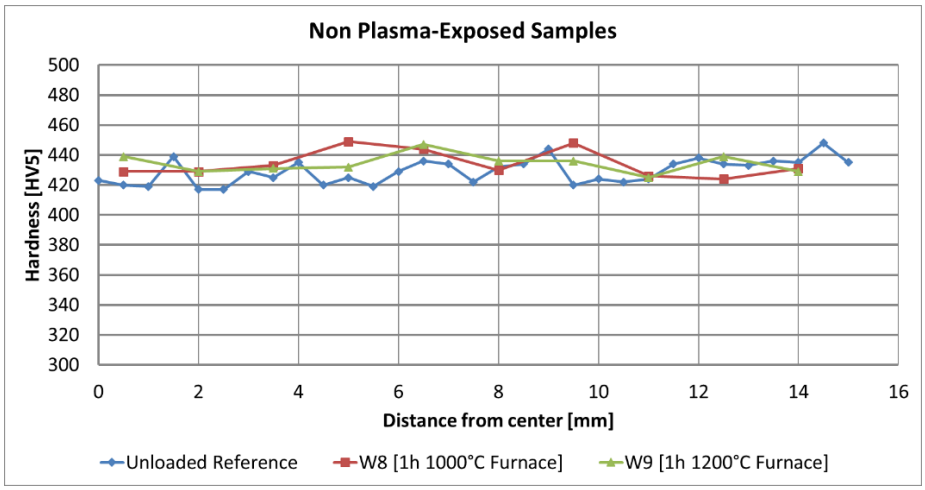

Figure 55. Hardness measurements across profile for unexposed samples

The results from Figure 55 show that, as expected, there was no identifiable recrystallization under these conditions (this point will be elaborated further in the Discussion). The averages were 421 ± 4 HV5 with the minimum hardness measured at 417 HV and the maximum at 449. This baseline suggests that if plasma has no effect on recrystallization, plasma exposure under this regime (1 h at 1000 – 1200 °C) should show no recrystallization either.

6.2.2 Sample W1 [1200 °C Base + 200 °C Pulses]

For W1, surface hardness measurements were complemented with cross-sectional measurements at a depth of 1mm below the exposed surface. The hardness measurements show some variance at lower temperatures, and tend towards a slow decrease in hardness consistent with recovery behavior. The surface was too damaged due to the plasma pulses to take a direct surface recrystallization measurement at the strike point. Measuring from the lower temperature regions, the observed recovery behavior abruptly ends at ~1000 °C where a sharp decrease in hardness, consistent with recrystallization, occurs. This grain size change can be visually observed, and moreover it remarkably follows the isothermal line marking for 982 °C from the FEM simulation. This analysis is summarized in Figure 56.

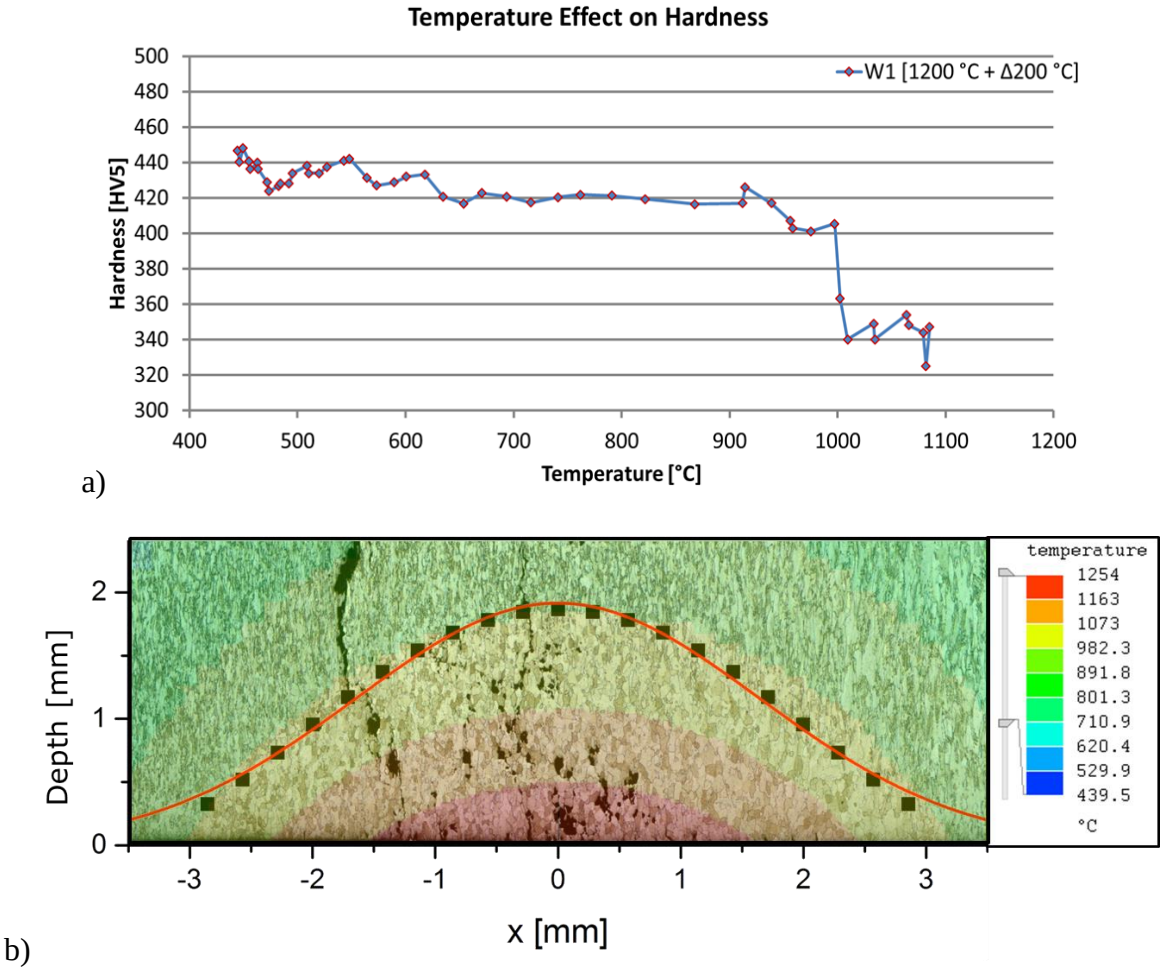

Figure 56. W1 a) Hardness vs. Temperature plot and b) cross-section superimposed with corresponding temperature map from FEM simulation (dotted line to guide the eye on identified recrystallization threshold)

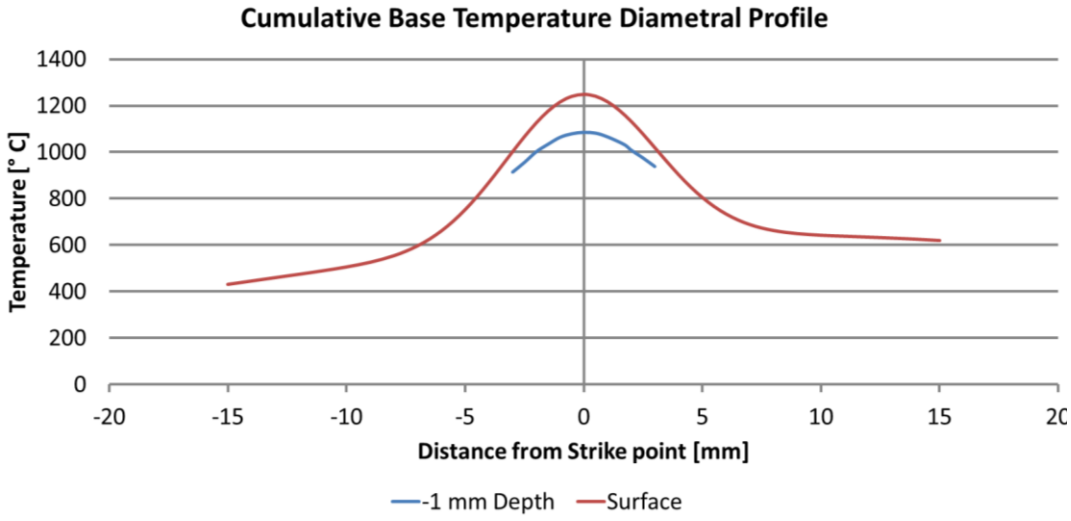

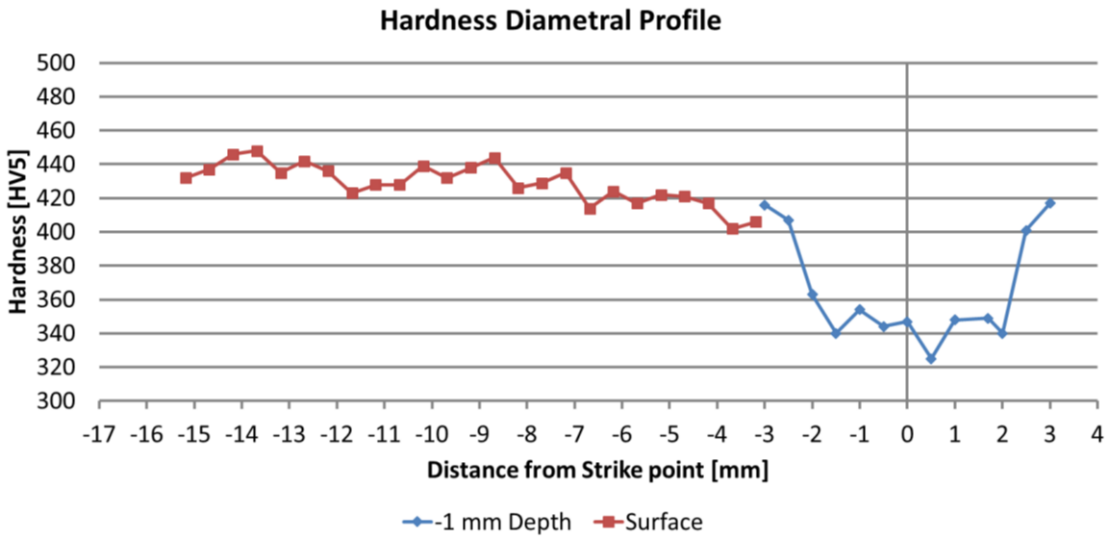

Figure 57. W1 a) base temperature and b) hardness diametral profiles for surface and bulk

6.2.3 Sample W2 [1500 °C Base + 200 °C Pulses]

For W2, surface hardness measurements were complemented with cross-sectional measurements at a depth of 2 mm below the exposed surface. The hardness measurements show some variance at lower temperatures, and although it seems to tend towards a slow decrease in hardness consistent with recovery behavior, this is not obviously clear from the data, as the variance oscillates during this section. The surface was too damaged due to the plasma pulses to take a direct surface recrystallization measurement at the strike point. Measuring from the lower temperature regions, the "high hardness" behavior abruptly ends at ~980 °C where a sharp decrease in hardness, consistent with recrystallization, occurs. This observed recovery was obtained from the bulk measurements. The grain size change can be visually observed, and it again remarkably follows the isothermal line marking for 891 °C from the FEM simulation (although this correlation is weaker than in other samples). This analysis is summarized in Figure 58.

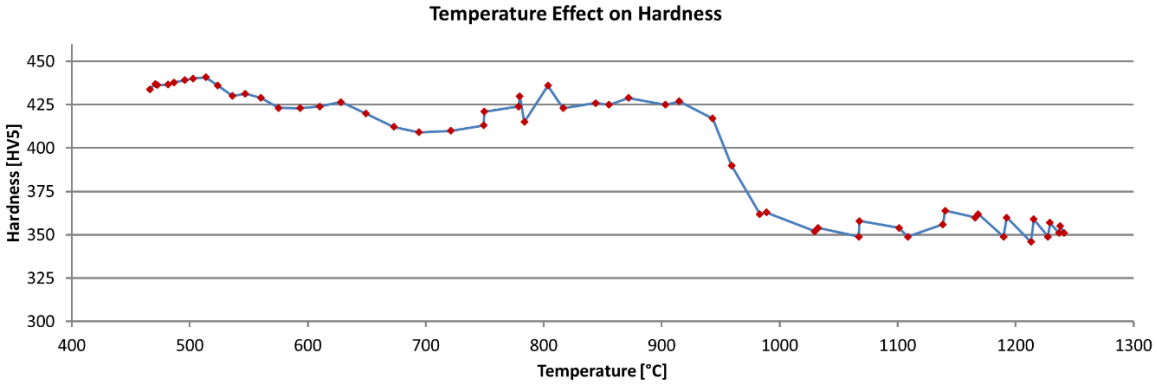

a)

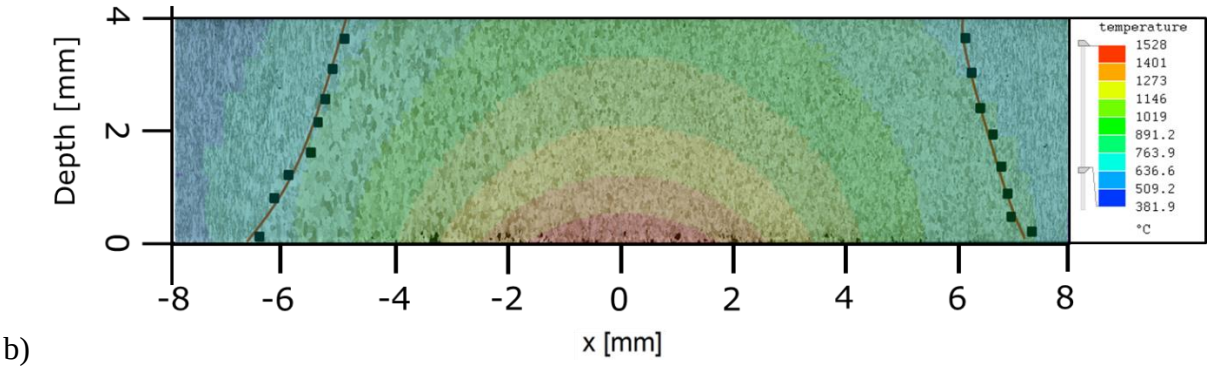

b)

Figure 58. W2 a) Hardness vs. Temperature plot and b) cross-section superimposed with corresponding temperature map from FEM simulation (dotted line to guide the eye on identified recrystallization threshold)

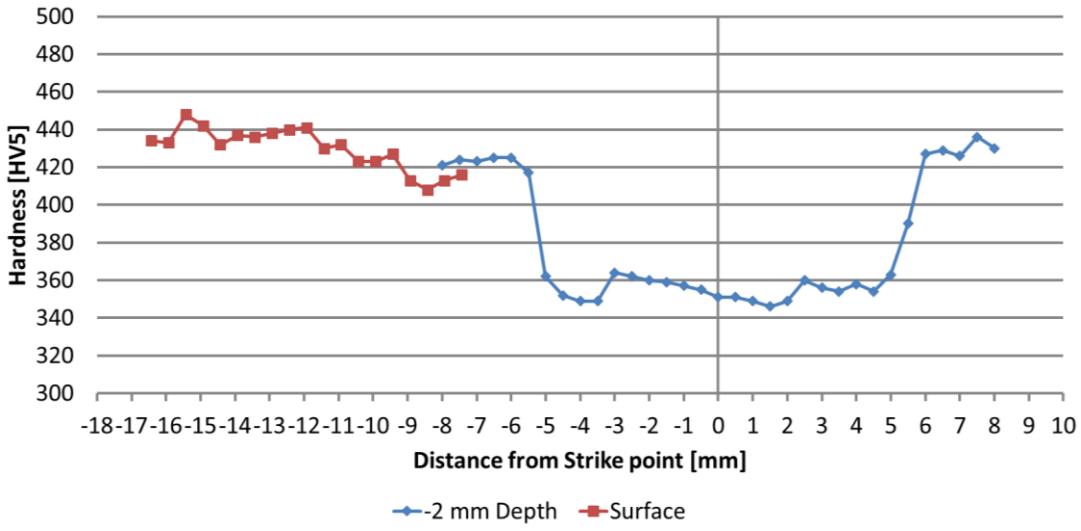

a)

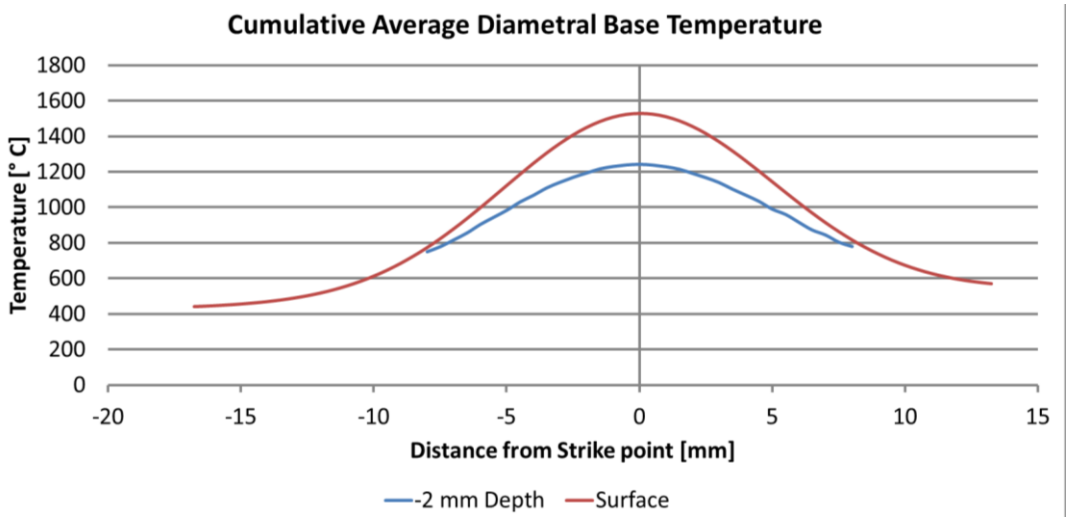

b)

Figure 59. W2 a) base temperature and b) hardness diametral profiles for surface and bulk

6.2.4 Sample W6 [1000 °C Base + 300 °C Pulses]

For W6, no surface hardness measurements were taken as there was copper contamination at the end of the exposure due to the Magnum-PSI source breaking down as previously mentioned. It was agreed then not to do this analysis, as it may have not been reliable. This accounts for the low number of data points compared to other samples. Hardness measurements were then taken in the cross-sectional area at a depth of 0.6 mm below the exposed surface. The hardness measurements show a stable behavior at lower temperatures, with a value around 420 HV, consistent with recovery behavior. The "high hardness" behavior stops at a point between ~850 °C and ~980 °C which is lower than previously seen, although this might be an effect due to the low number of data points. The grain size change can be visually observed, and it again remarkably follows the isothermal line marking for 891 °C from the FEM simulation. Due to the proximity to the border, hardness measurements were not taken closer to it. This analysis is summarized in Figure 60.

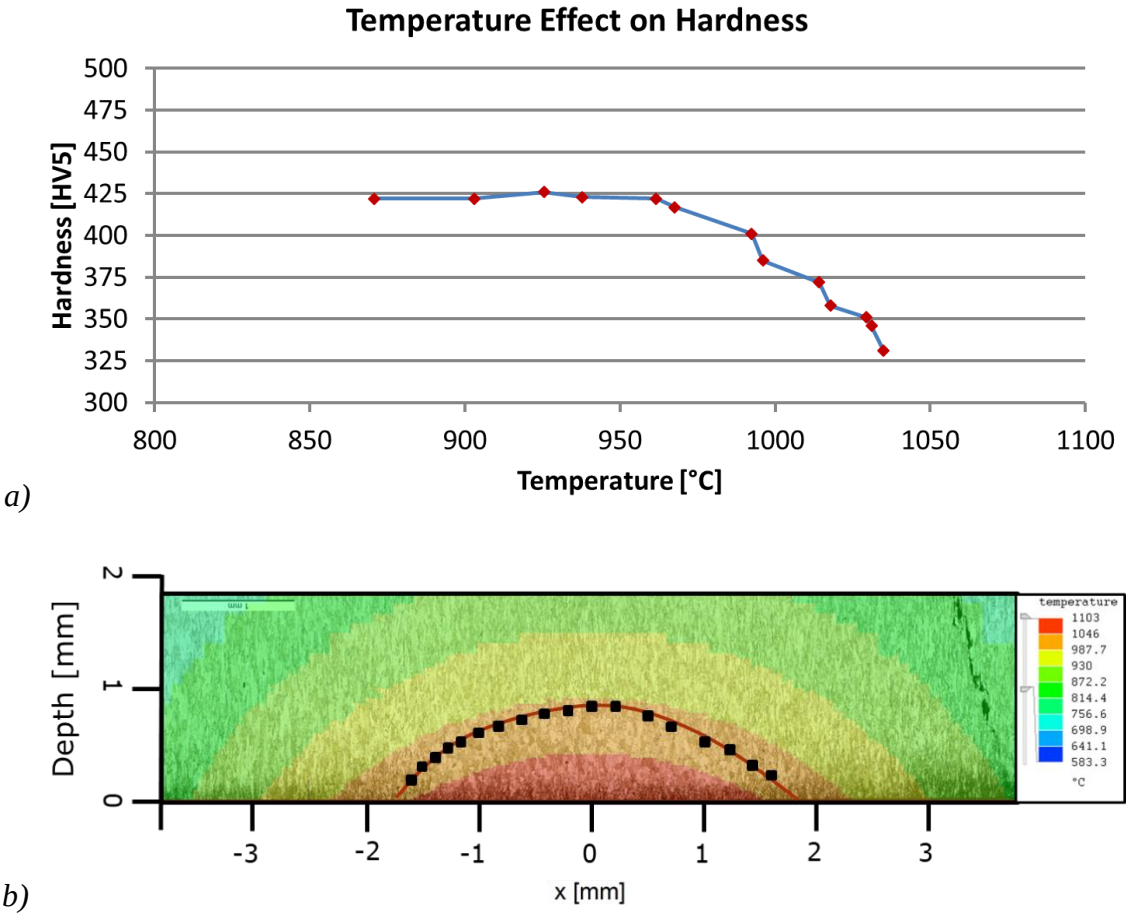

Figure 60. W6 a) Hardness vs. Temperature plot and b) cross-section superimposed with corresponding temperature map from FEM simulation (dotted line to guide the eye on identified recrystallization threshold)

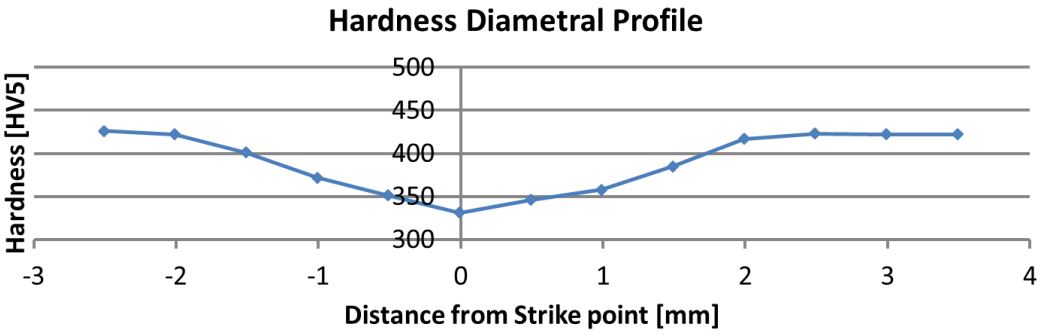

a)

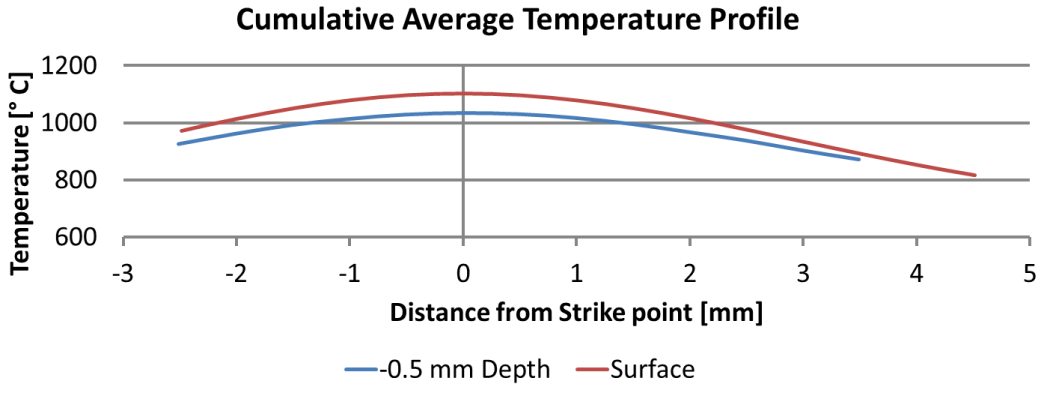

b)

Figure 61. W6 a) base temperature and b) hardness diametral profiles for surface and bulk

6.2.5 Sample W4 [1000 °C Base]

W4 was exposed to steady state plasma loading, in contrast to the previous pulsed samples. The average temperature at the strike point was 996 °C. Surface hardness measurements were complemented with cross-sectional measurements at a depth of -0.6 mm below the exposed surface. The hardness measurements show some oscillation through the whole temperature range, nevertheless it seems to tend towards a slow decrease in hardness consistent with recovery behavior. There is no sign of recrystallization in the hardness data collected. The grain size change can be visually observed, to show some recrystallization but due to the proximity to the border, hardness measurements were not taken closer to it. This analysis and the surface temperature profile for W4 are shown in Figures 62 and 63.

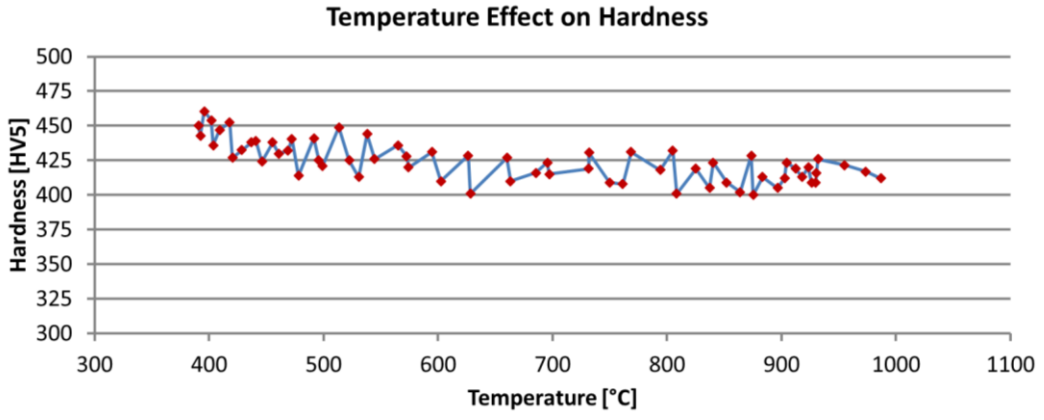

a)

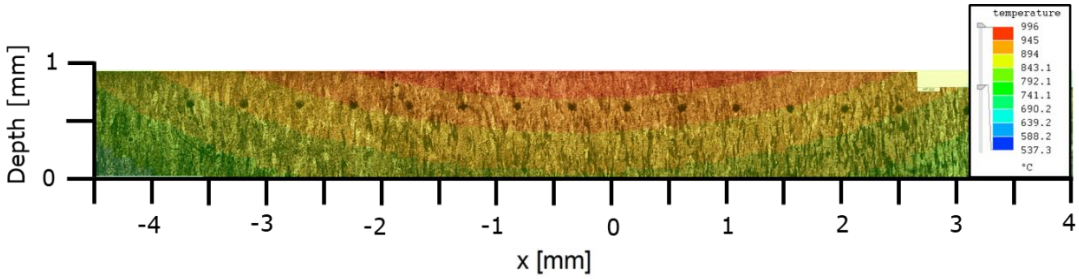

b)

Figure 62. W4 a) Cross-section superimposed with corresponding temperature map from FEM simulation and b) Hardness vs. Temperature plot

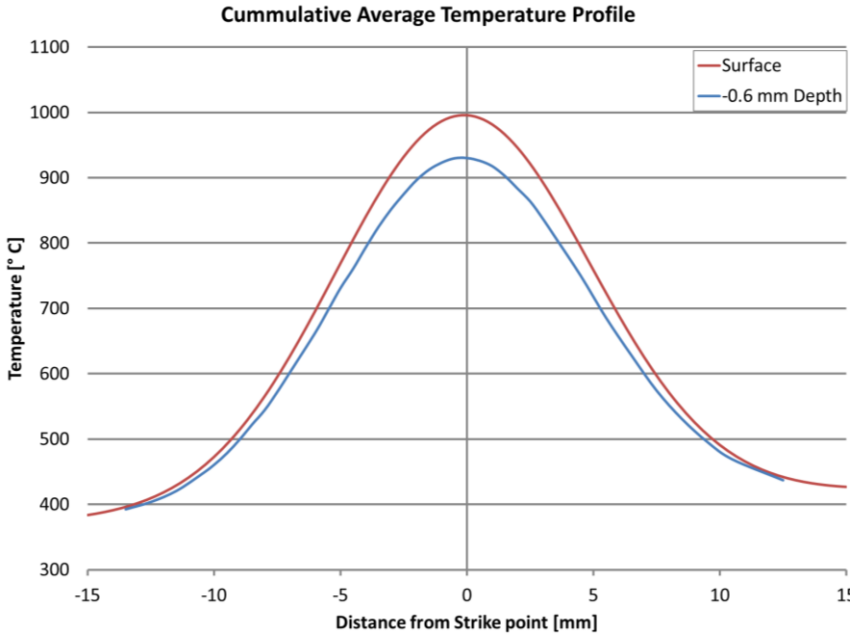

a)

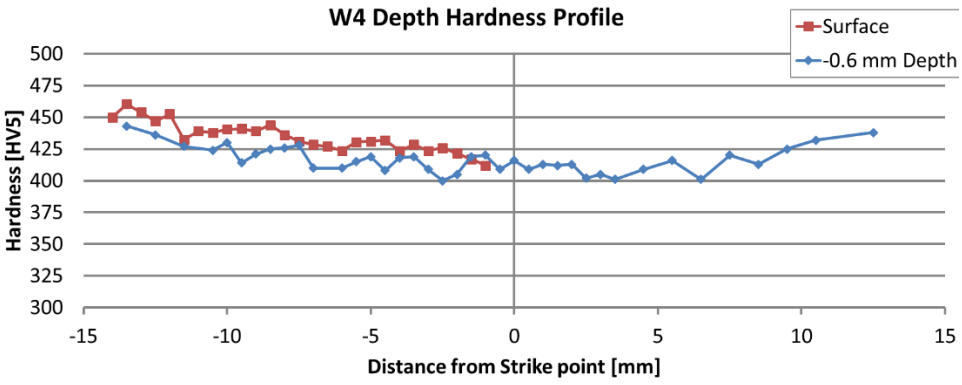

b)

Figure 63. W4 a) base temperature and b) hardness diametral profiles for surface and bulk

6.2.6 Sample W3 [1500 °C Base]

W3 was exposed to steady state plasma loading with an average temperature at the strike point of 1532 °C. Curiously, when analyzing the grain structure, there is an abnormal grain growth structure shown in Figure 64. This phenomena was not observed in any of the other samples.

Figure 64. W3 abnormal grain growth

Our hypothesis is that for some reason thermal contact was lost between part of the backside of the sample and the cooling surface below. The left side of Figure 64 does show a more "common" grain structure and separating band between elongated and recrystallized grains. Moreover, the surface temperature IR recordings show a ~200 °C asymmetry between the 2 edges of the disk, but the highest intensity is still located towards the center of the beam and not on an edge as seen in Figure 65.

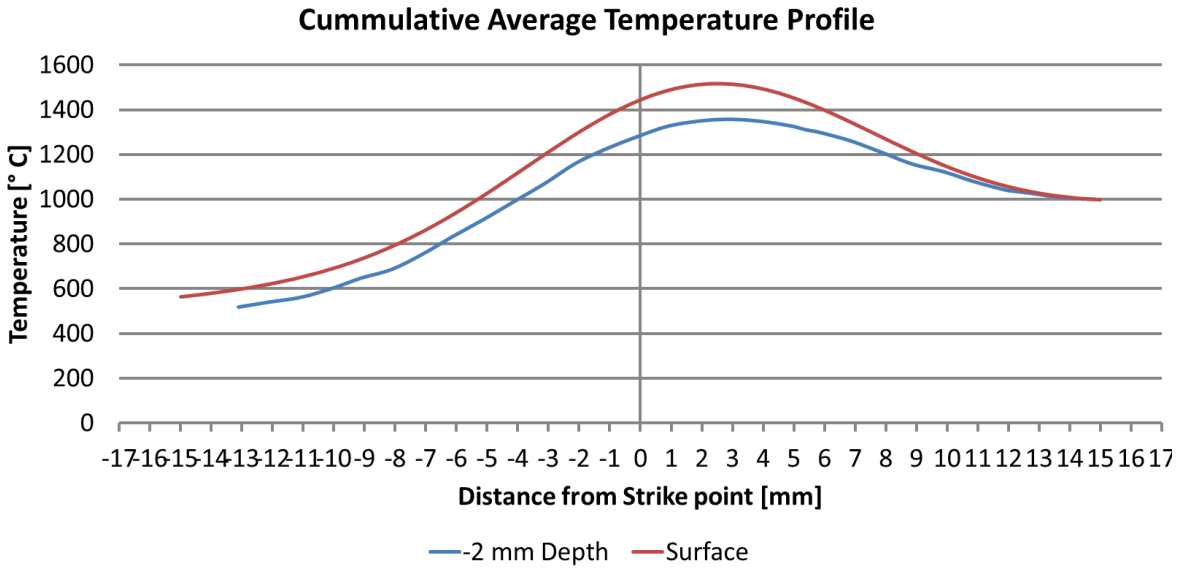

Figure 65. W3 base temperature profile

Using this surface data as starting point, the FEM software was used to simulate several conditions of lost cooling contact to try to replicate the observed cross-section effects. The result was, that by removing 19.5 mm of thermal contact from the bottom of the sample (this would simulate the screws on the target holder from one side not clamping the sample in place against the cooling plaque) a temperature banded profile that closely matches the recrystallization band profile from the left side of Figure 66 and the beginning of the abnormal grain growth on the right side of it. Moreover, if we plot the Heat Flux as well we can

differentiate between two regions, a high temperature and high heat flux region, and a high temperature and low heat flux one, which divide the two recrystallized sections observed in the image.

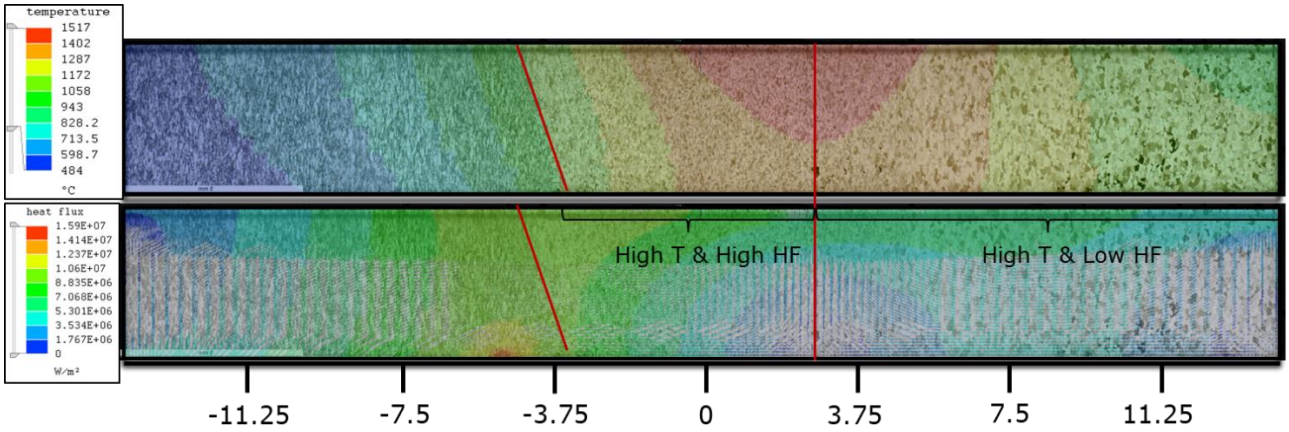

Figure 66. W3 cross-section a) temperature and b) heat flux profiles showing a marked distinction between the termed "High Temperature and High Heat Flux" and "High Temperature and Low Heat Flux" regimes

Surface hardness measurements were complemented with cross-sectional measurements at a depth of 2 mm below the exposed surface, but because of the temperature profile anomaly, they are first presented separately, as the surface results can reliably be reported as accurate, while there is a more substantial assumption made for the other. Nevertheless, both data sets, the surface one which was taken from the "left side" of the sample, and the "2 mm" depth one across the whole bulk, reasonably agree with each other, showing a recrystallization threshold at ~1050 °C.

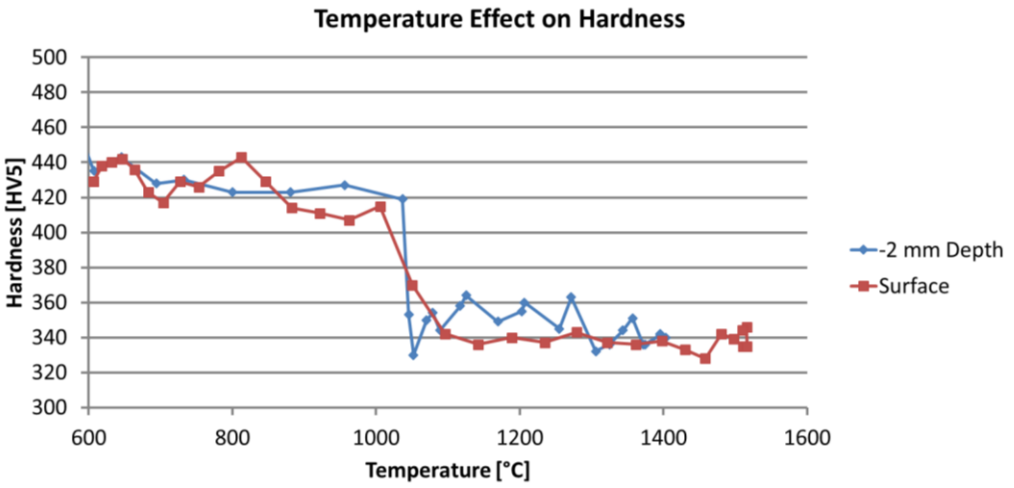

a)

b)

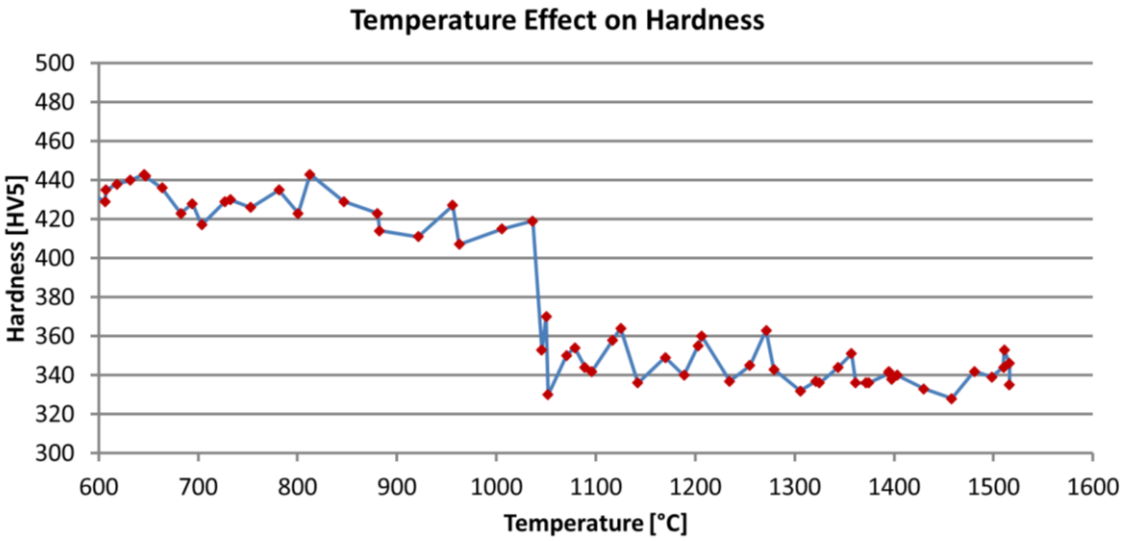

Figure 67. a) Surface and bulk at 2mm depth Temperature vs Hardness plot for W3 and b) combined surface and bulk plot

6.2.7 W5 [1500 °C Base] (4 hour exposure)

For W5, a longer exposure was set to take the conditions to the extreme: 4 hours at steady state plasma with a maximum of 1500 °C. Surface hardness measurements were complemented with cross-sectional measurements at a depth of -3 mm below the exposed surface. The hardness measurements show complete recrystallization through the bulk even at 75% of the depth. The grain size change can be visually observed to show a homogenized grain structure. This analysis and the surface temperature profile for W5 are shown in Figures 68 and 69.

a)

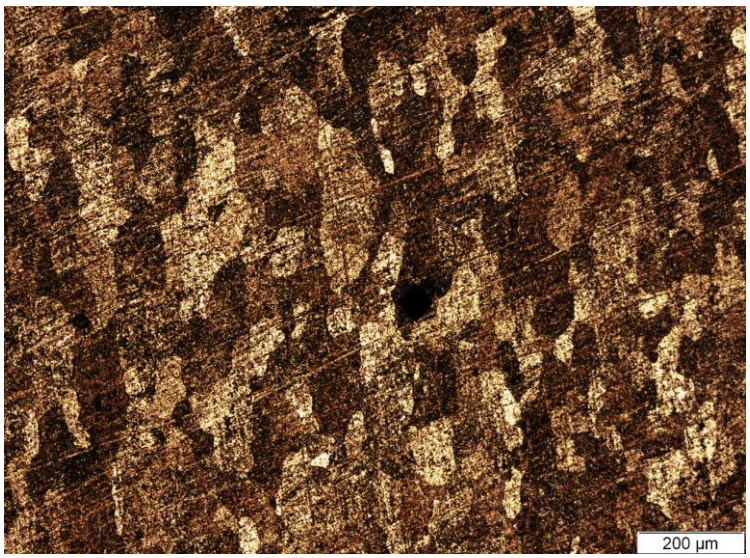

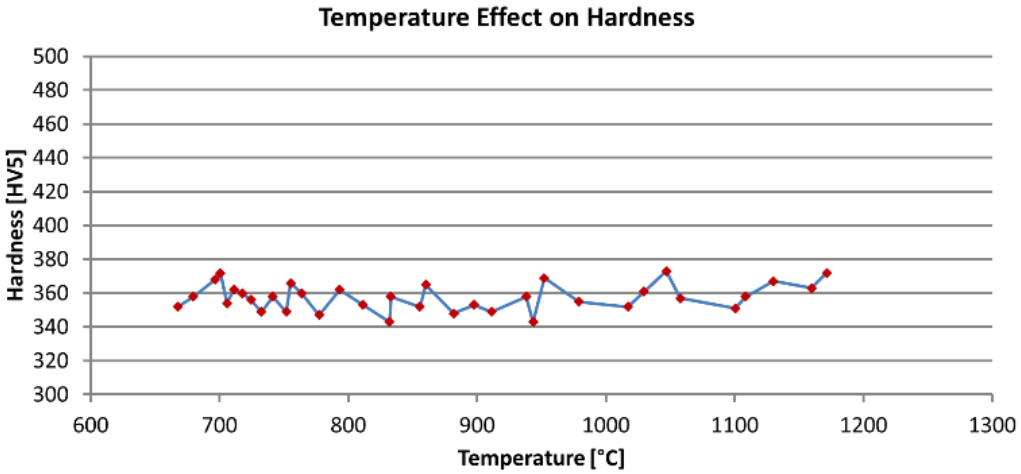

b)

Figure 68. a) Grain structure throughout W5 and b) Hardness vs. Temperature plot

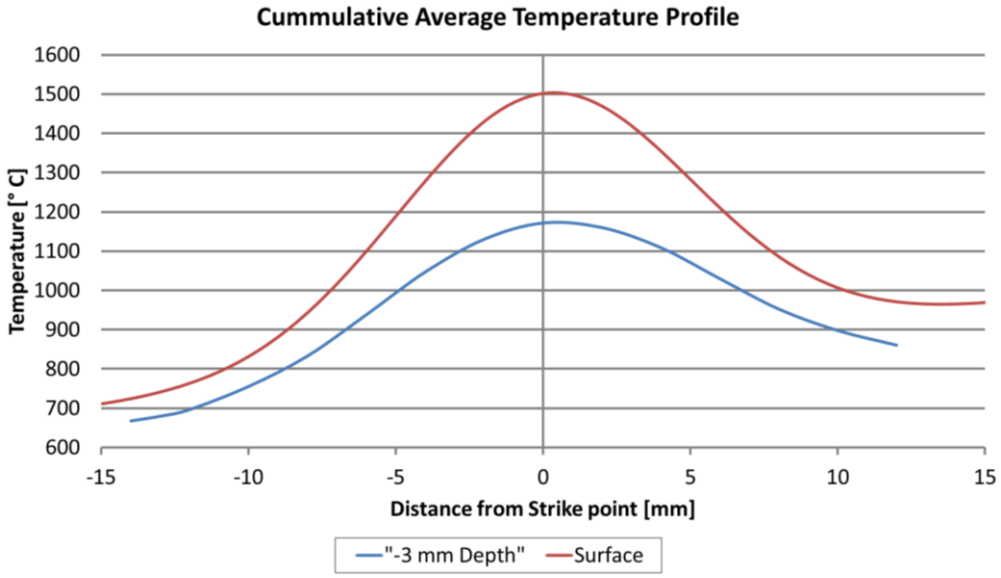

a)

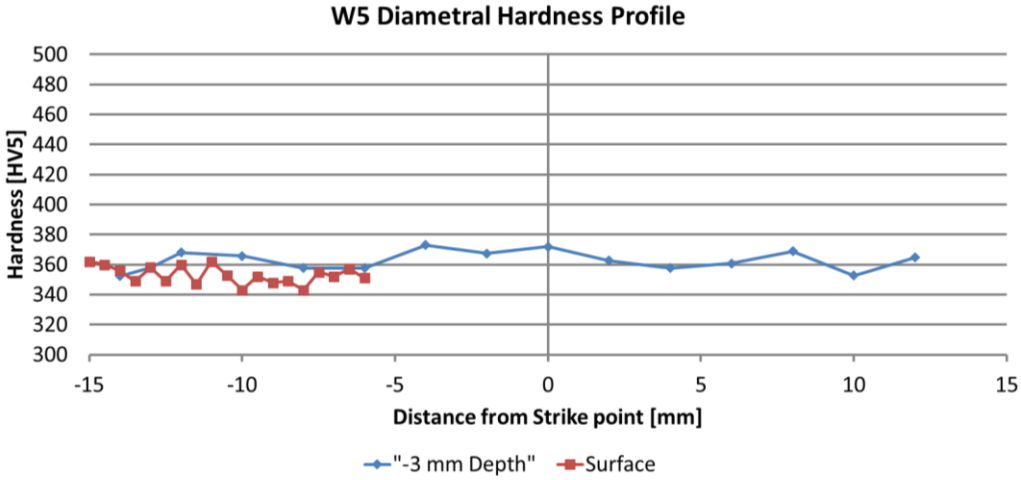

b)

Figure 69. W5 a) base temperature and b) hardness diametral profiles for surface and bulk

6.2.8 Summary Recrystallization Behavior

Based on the IR camera analysis, the average temperature of the samples' surface is constant throughout the shot regardless of the transient pulses, and as shown by the FEM analysis, the pulse´s temperature excursion quickly dissipates below the surface. Because of this the recrystallization behavior was characterized versus the base temperature on the surface of the sample, as well as the steady state calculated temperature of the bulk. The bulk measurements were all taken at least twice as far from the surface, as the pulse excursion to prevent any issues with the reliability of the temperature referenced. The isochronal behavior of all samples exposed for 1 hour is shown in Figure 70.

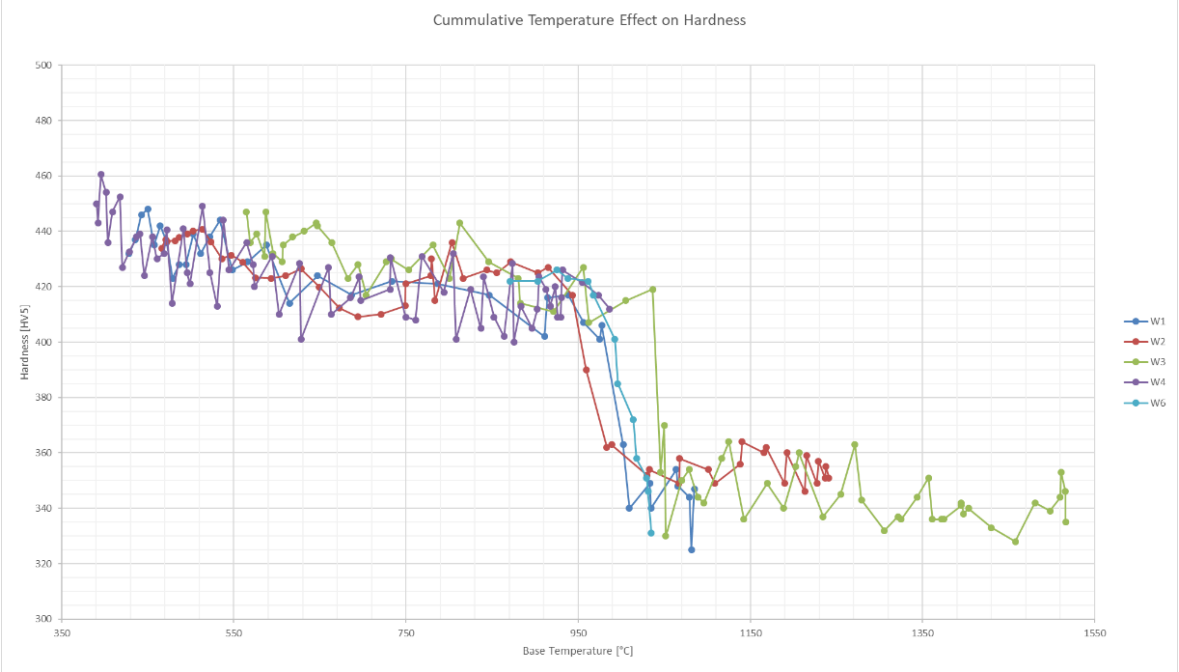

Figure 70.Cumulative hardness behavior of all 1h exposed samples vs the base temperature of the measurement location.

The cumulative behavior shows what looks like a logarithmic decay in hardness which is consistent with the expected recovery mechanics during annealing (this will be explored in chapter 7). This behavior stops at a region between 960 and 990 °C, where the hardness abruptly drops. This hardness drop is consistent with recrystallization behavior, and it shows a very steep slope during the temperature transition at the studied timescale and temperature range. There is no appreciable difference between the behavior of the surface and the bulk measurements, and thus for this analysis they were treated equally, even for sample W3 where the grain distribution and size suggested an atypical behavior. It is worth noting that, although the general behavior of W3 is consistent with the rest of the samples, it does show a recrystallization temperature slightly higher than the rest of them (~100 °C), but there is also a higher uncertainty on the bulk temperature of this sample due to the characterization difficulties detailed in section 6.2.6. The general behavior of the curve in Figure 70 is consistent with what is expected of tungsten from the available studies [17] but as will be discussed in chapter 7, the

recrystallization temperature measured was ~300 °C lower than expected from the available body of work.

6.3 Hydrogen Concentrations

For the hydrogen concentration calculation, the tungsten's behavior was simulated by TMAP7. The material's depth profile was modeled with finer elements of 2.5 nm near the surface, gradually growing to 0.5 mm deep in the bulk of the target (see Table 4). Thomson Scatter data collected from the center of the strike point was used for the plasma parameters, and reference literature data was used for the tungsten-hydrogen interaction properties. The above parameters are summarized in Table 3. For ease of calculation resources, intrinsic defects and traps (dislocations, grain boundaries, and vacancies) are coupled together in one defect parameter. Concentration is given in traps per W atom. [30][44]

Activation energy		eV
dissociation energy	$\frac{1}{2}E_{D_2}^{D}$	2.3
chemisorption energy	E_c	0.4–0.9
diffusion barrier	E_m	0.39
heat of solution	E_s	1.04

E_{trap}	trap concentration	depth
0.85 eV	$1.0 \cdot 10^{-4}$	whole

# of Elements	Depth of element [m]
1	0
8	2.5e-09
8	1.0e-08
4	2.5e-08
8	1.0e-07
4	2.5-07
8	1.0e-06
4	2.5e-06
8	1.0e-05
4	2.5e-05
8	0.0001
6	0.0005
1	0

Tables 3 & 4. Reference values for diffusion parameters and trapping energies of hydrogen in tungsten used for TMAP7 simulations and layer structure of simulated depth profile of W sample for simulation. [30] [44]

6.3.1 Sample W1 [1200 °C Base + 200 °C Pulses]

At the center of the strike point the Thomson Scattering measured data for W1 was collected and averaged for use in the TMAP7 simulation (See Figure 71). This data is summarized in Table 5. With this data and the FEM temperature bulk analysis from section 6.2, TMAP7 calculates the hydrogen trapped concentration through the bulk during the exposure.

Plasma Parameters	Values
Electron temperature (Te)	1.87 [eV]
Electron density (ne)	1.14×10^{20} [m^{-3}]
Time to reach steady Temp	80 [s]
Total exposure time	3600 [s]
Particle flux (Γ)	0.868×10^{24} [m^{-2}]

Table 5. W1 plasma parameters used for TMAP7 simulation

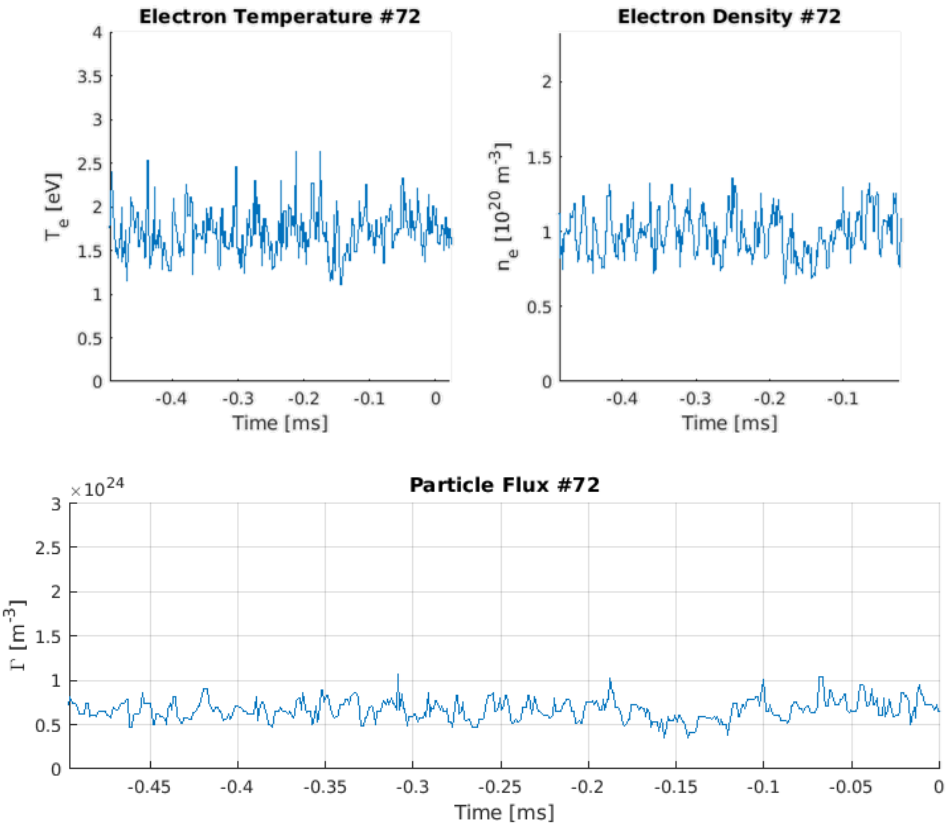

Figure 71. W1 experimental Thomson Scattering collected data

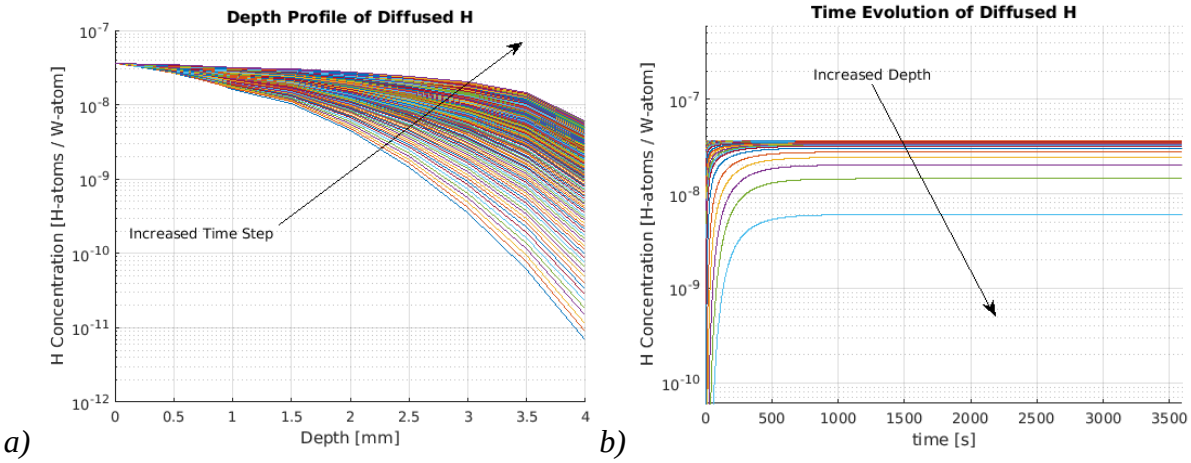

Figure 72. W2 trapped hydrogen concentration. a) Depth profile each time-step and b) Time evolution per layer inside the bulk

The simulations in Figure 72 show that near the surface of the sample, the hydrogen concentration quickly saturates at 3.59×10^{-8}. At the bottom of the bulk, the hydrogen concentration begins at 6.81×10^{-12} and as time goes by, gradually increases, until at ~1100 seconds it saturates at 6.02×10^{-9}. These levels do not change throughout the course of the exposure.

6.3.2 Sample W2 [1500 °C Base + 200 °C Pulses]

At the center of the strike point the Thomson Scattering measured data for W2 was collected and averaged for use in the TMAP7 simulation (See Figure 73). This data is summarized in Table 6. With this data and the FEM temperature bulk analysis from section 6.2, TMAP7 calculates the hydrogen trapped concentration through the bulk during the exposure.

Plasma Parameters	Values
Electron temperature (Te)	2.4 [eV]
Electron density (ne)	5.00×10^{20} [m^{-3}]
Time to reach steady Temp	67 [s]
Total exposure time	3600 [s]
Particle flux (Γ)	4.338×10^{24} [m^{-2}]

Table 6. W2 plasma parameters used for TMAP7 simulation

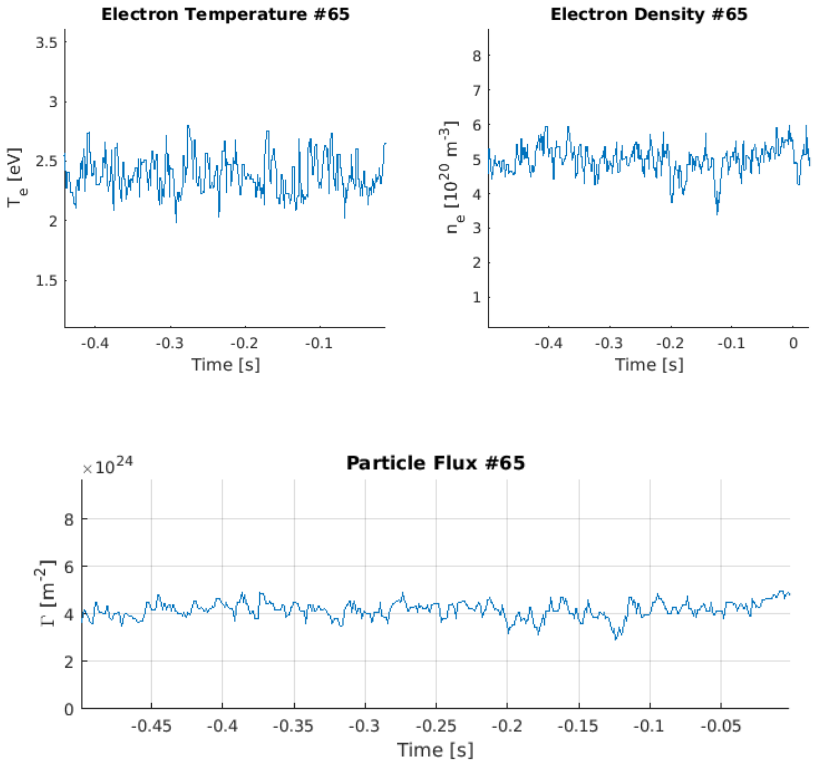

Figure 73. W2 experimental Thomson Scattering collected data

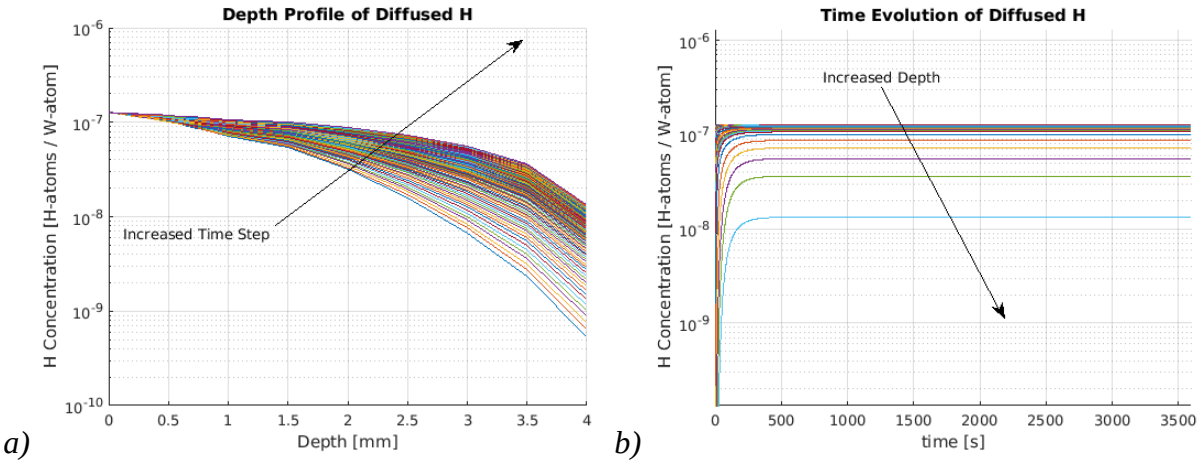

a) *b)*

Figure 74. W2 trapped hydrogen concentration. a) Depth profile each time-step and b) Time evolution per layer inside the bulk

The simulations in Figure 74 show that near the surface of the sample, the hydrogen concentration quickly saturates at 1.27×10^{-7}. At the bottom of the bulk, the hydrogen concentration begins at 3.17×10^{-10} and as time goes by, gradually increases, until at ~530 seconds it saturates at 1.33×10^{-8}. These levels do not change throughout the course of the exposure.

6.3.3 Sample W4 [1000 °C Base]

At the center of the strike point the Thomson Scattering measured data for W4 was collected and averaged for use in the TMAP7 simulation (See Figure 76). This data is summarized in Table 7. With this data and the FEM temperature bulk analysis from section 6.2, TMAP7 calculates the hydrogen trapped concentration through the bulk during the exposure. Thomson Scattering was set with a low frame rate to accommodate the intended long term exposure, but ended up being too low to see the variance of the signal. Nevertheless the average values for T_e and n_e are clear from the data in Figure 75.

Plasma Parameters	Values
Electron temperature (Te)	2.12 [eV]
Electron density (ne)	3.89×10^{20} [m^{-3}]
Time to reach steady Temp	93 [s]
Total exposure time	3600 [s]
Particle flux (Γ)	3.220×10^{24} [m^{-2}]

Table 7. W4 plasma parameters used for TMAP7 simulation

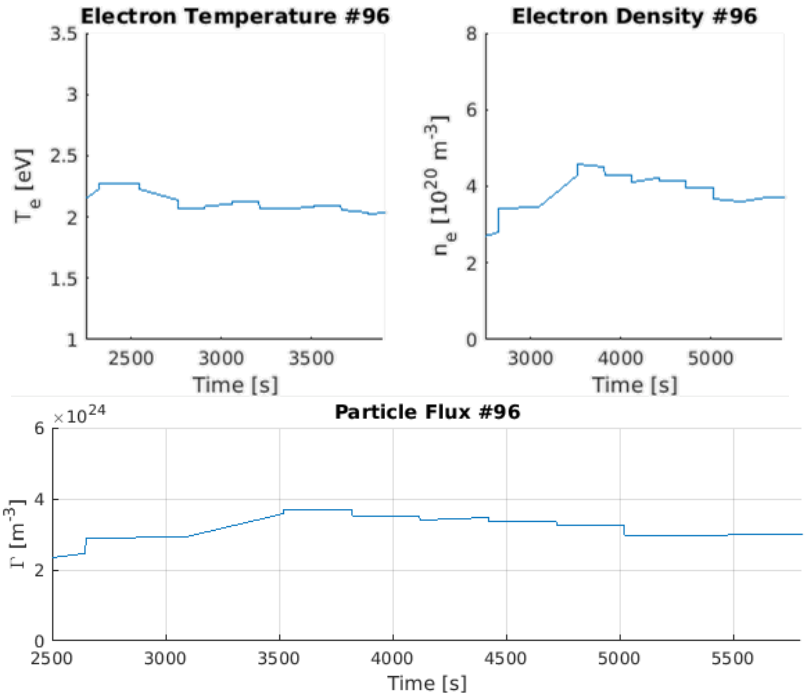

Figure 75. W4 experimental Thomson Scattering collected data

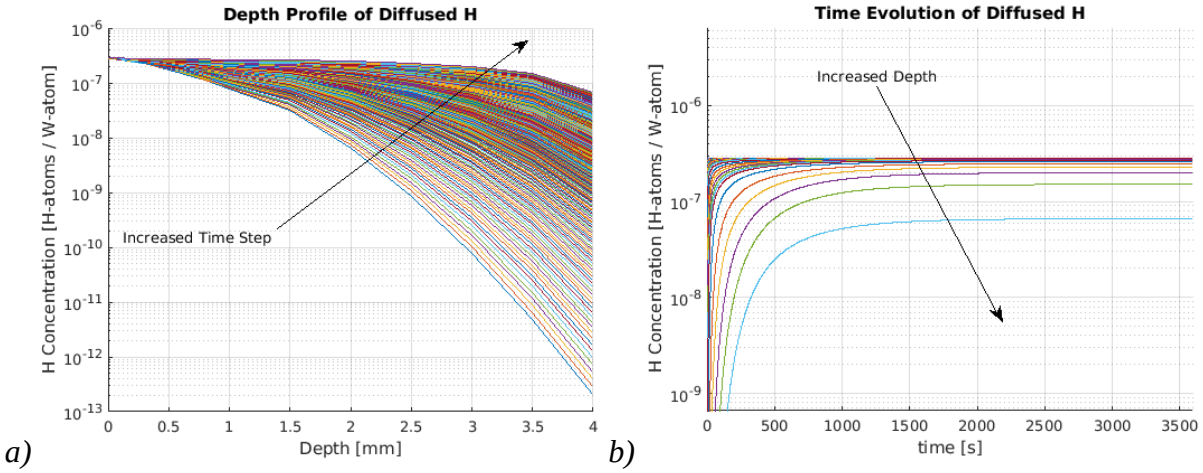

a) *b)*

Figure 76. W2 trapped hydrogen concentration. a) Depth profile each time-step and b) Time evolution per layer inside the bulk

The simulations in Figure 76 show that near the surface of the sample, the hydrogen concentration quickly saturates at 2.83×10^{-7}. At the bottom of the bulk, the hydrogen concentration begins at 2.03×10^{-13} and as time goes by, gradually increases, until at ~2100 seconds it saturates at 6.59×10^{-8}. These levels do not change throughout the course of the exposure. It is worth noting that saturation at the bottom of the bulk is much lower in this regime than in the other samples studied.

6.3.4 Sample W5 [1500 °C Base] (4 hour exposure)

At the center of the strike point the Thomson Scattering measured data for W5 was collected and averaged for use in the TMAP7 simulation (See Figure 78). This data is summarized in Table 8. With this data and the FEM temperature bulk analysis from section 6.2, TMAP7 calculates the hydrogen trapped concentration through the bulk during the exposure. Thomson Scattering was set with a low frame rate to accommodate the intended long term exposure, but ended up being too low to see the variance of the signal. Nevertheless the average values for T_e and n_e are clear from the data in Figure 77.

Plasma Parameters	Values
Electron temperature (Te)	3.12 [eV]
Electron density (ne)	0.95×10^{20} [m^{-3}]
Time to reach steady Temp	60 [s]
Total exposure time	14400 [s]
Particle flux (Γ)	0.935×10^{24} [m^{-2}]

Table 8. W4 plasma parameters used for TMAP7 simulation

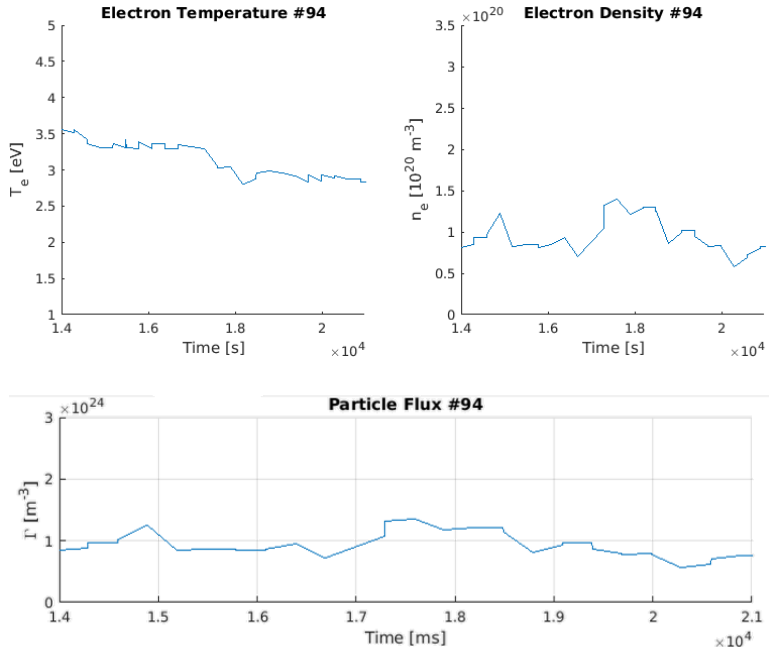

Figure 77. W4 experimental Thomson Scattering collected data

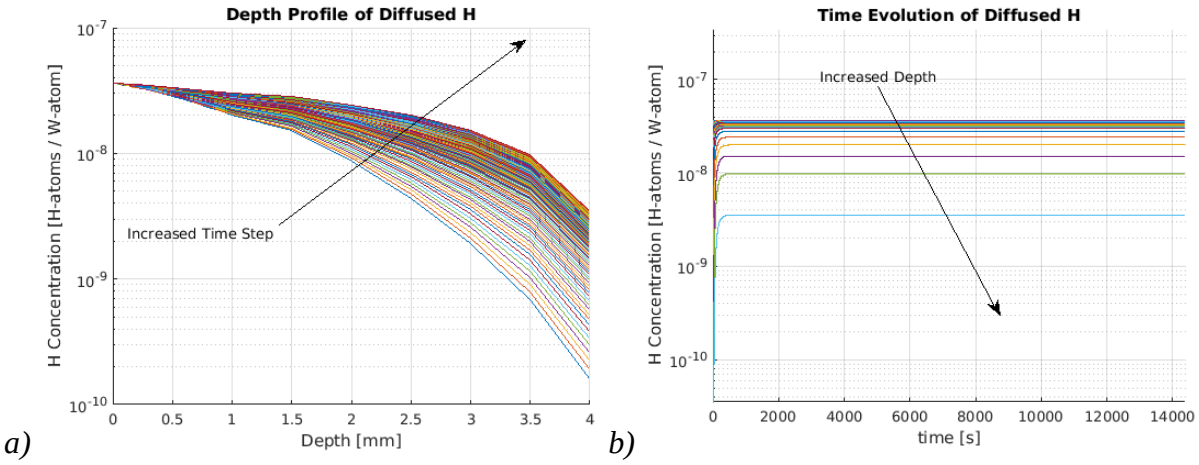

Figure 78. W5 trapped hydrogen concentration. a) Depth profile each time-step and b) Time evolution per layer inside the bulk

The simulations in Figure 78 show that near the surface of the sample, the hydrogen concentration quickly saturates at 3.63×10^{-8}. At the bottom of the bulk, the hydrogen concentration begins at 1.60×10^{-10} and as time goes by, gradually increases, until at ~420 seconds it saturates at 3.53×10^{-9}. These levels do not change throughout the course of the exposure.

6.3.5 Sample W6 [1000 °C Base + 300 °C Pulses]

Thomson Scatter diagnostic did not fire during the exposure W6 so no plasma data could be retrieved. Reasons for this are unclear and the situation was detected after the exposure, not during it, so no corrections were able to be taken.

6.3.6 Sample W3 [1500 °C Base]

As mentioned in section 6.2.6, sample W3 showed an abnormal material and temperature response behavior, somewhat consistent with bad thermal contact, but not completely explained by it. According to the FEM simulation, heat flux in this sample does not flow straightforwardly from the surface to the bottom of the sample, and so, the TMAP7 1D simulation is inadequate to characterize the diffusion of hydrogen during this experiment. Because of this, no calculations are shown for this sample.

6.3.7 Summary Hydrogen Concentration

The TMAP7 simulations show that in general near the surface of the sample, the mobile hydrogen concentration quickly saturates for the whole exposure, and at the bottom of the bulk, the mobile hydrogen concentration starts from a concentration a hundred times less than that of the surface soon after the plasma exposure starts. As time goes by, this level gradually increases, until it saturates at a concentration around ten times less than that of the surface. Among the exposed samples the simulated concentration near the surface ranged from 0.359 – 2.83×10^{-7} and at the bottom of the bulk ranged from 0.353 – 6.59×10^{-8}. As seen in the timing plots, these levels stabilize relatively quickly in respect to the total exposure time, and afterwards do not change throughout the course of the exposure.

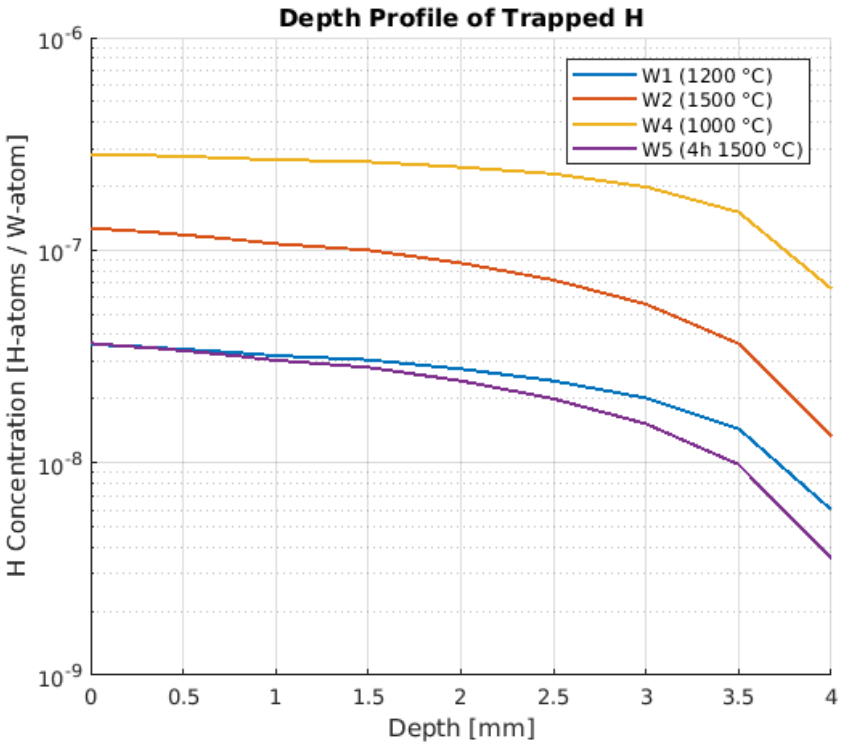

Figure 79. Samples' cumulative H concentration simulation at the end of their respective exposure.

7. Discussion

7.1 Surface damage morphologies classification

Understanding the damage response of tungsten to the expected ELMs, as well as to any other temperature excursions that can occur during the reactor's operation is of paramount importance. Temperature excursions in the reactor are of varied nature and levels. Reviewing the temperature range, heat flux and pulse durations calculated in Chapter 6, this research's loading regime falls on the order of magnitude of the expected ELMs and transient reattachment events hitting the divertor [35]. Although ELMs and other transient events can have higher power densities than the ones studied [18], this range in particular encompasses the reported safe operation conditions of the tungsten divertor, and as seen earlier in chapter 6 there was prominent damage on the studied samples.

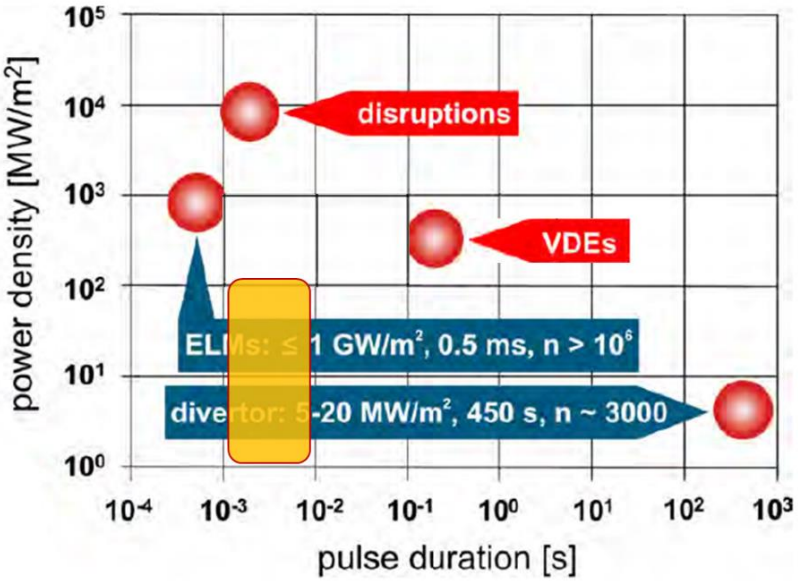

Figure 80. Different divertor operation regimes and this work's studied range [18]

Referring to the cumulative damage mapping in Figure 53 of section 6.4, a consistent behavior can be observed. Unsurprisingly, at higher temperatures and power densities, the damages identified tend to be more severe with crack networks dominating the damage morphology. Gradually looking at lower temperatures and power densities, the crack networks observed are less interconnected, with isolated cracks noticeably being visible below ~1100 °C and 100 MW m^{-2} regions of the plot. Crack networks stop dominating the damage landscape at ~1000 °C and 80 MW m^{-2} where interconnecting networks are smaller and scarcer, and evenly distributed isolated cracks through the surface of the samples become a more prominent features. In the same manner, as temperature and power density drops the identified cracks are of smaller until they are only recognized as microcracks. At this point the roughened surface is also a prominent feature through the sample. Consistency starts to break at this point as in one sample no roughening quickly begins to become apparent, in the other there is clear roughening until the edge of the target.

The thermomechanical stress that the samples were subjected to was clearly catastrophic, especially above ~1000 °C and 100 MW m^{-2}. Roughness profiles and statistical measurements of the crack parameters were made in an attempt to characterize the crack networks size, the cracks' widths and distribution, but the LM microscopy resolution and contrast, as well as the scope of the project itself and the time available, made this task unfeasible. Of special interest is the roughened surface apparently caused by thermoplastic deformation. This deformation seems to follow a preferential slip plane in the grains (see Figure 81). Additionally microcracks seem to appear at these sites (the statistical likelihood of this happening was left unresolved) which is an indicator that this is the mechanism by which cracks are nucleated, and thus where the material failure originates during pulsed regimes.

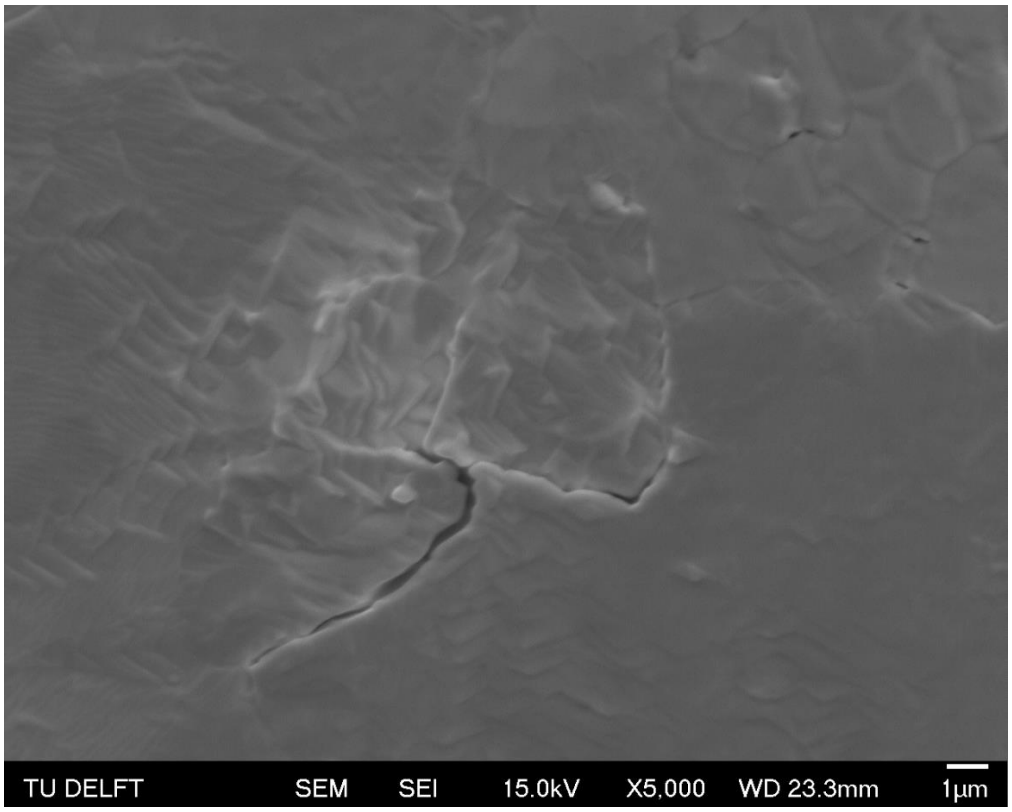

Figure 81. Microcracks forming at grain boundaries. Grains near the crack show plastic deformation in planes with a seemingly preferential orientation.

Notwithstanding the above, the damage mapping performed during this work, is in the same vein as the established literature on the matter, and adds to the current understanding of tungsten's behavior as a plasma facing material. In Figure 82 the results from Chapter 6 were added to the compiled analysis by other researchers in order to compare the different regimes in which tungsten has been studied [23][24][42].

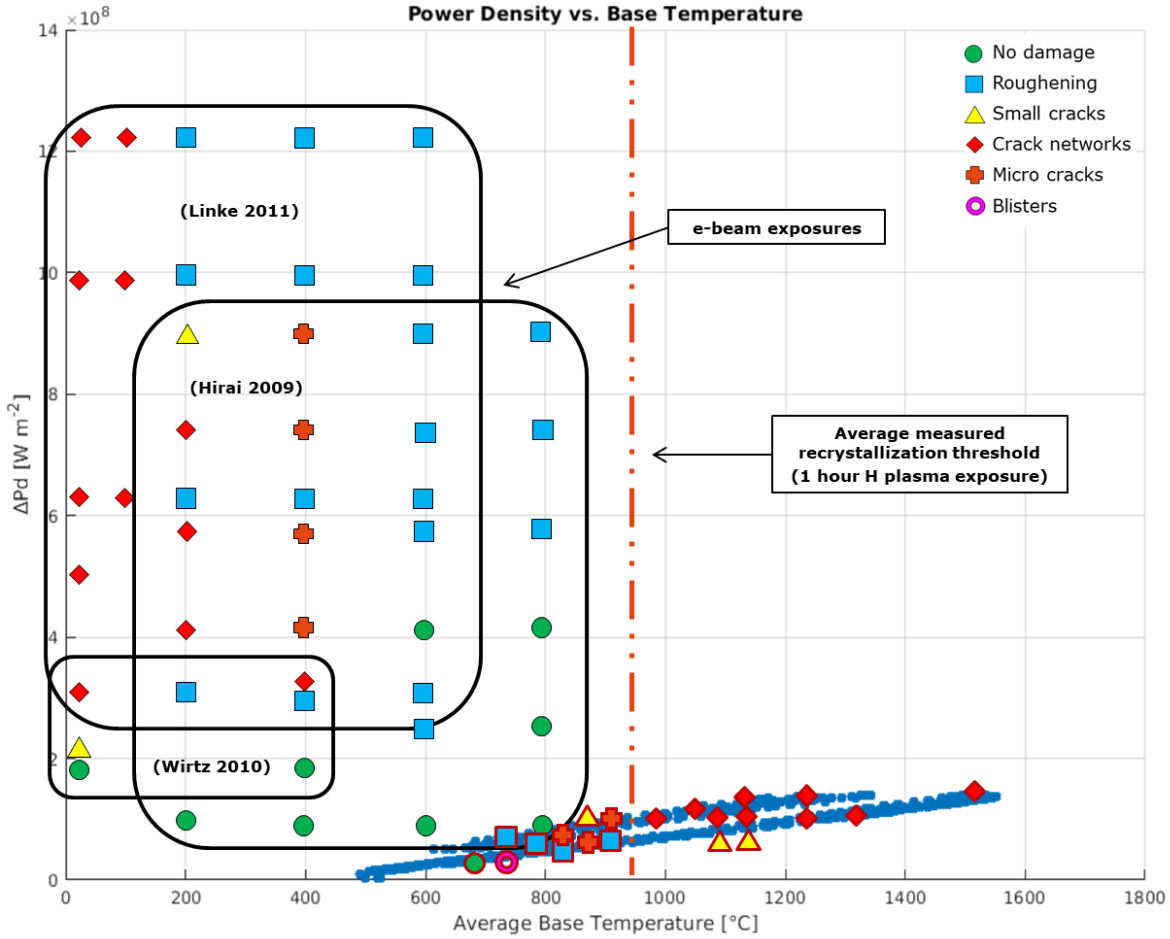

Figure 82. Damage classification of this work superimposed with body of literature [23][24][42]

The most striking feature of the compiled literature on W's response to ITER conditions, is that most of the research has been done with electron beam at low operation temperatures (up to 800 °C) but at a wide range of power densities (200 – 1400 MW m^{-2}). At these regimes, severe cracking seems to occur almost everywhere at low temperatures. As temperatures reach ~400 °C less cracking is observed and roughening and a roughening / microcracks regime dominates. This is consistent with the reported DBTT of tungsten at ~400 °C which would explain the observed better performance against crack formation [23][24][42].

On the other hand, the plasma loaded samples (all well above the DBTT) show the whole spectrum of damage morphologies. Of note is that the measured temperature at which recrystallization occurred in these samples seems to correlate relatively well with the point where cracks and the more severe damages dominate. Since HAGB promoted during recrystallization lead to grain boundary embrittlement and weakening this might be the cause of seeing this severe damage at what are relatively low power density pulses (at least compared to the standing body of literature). This would give further weight to the evidence that recrystallization is happening at this relatively low temperature compared to the expected behavior.

7.2 Modelling expected restoration behavior

Tungsten's properties, under conventional conditions, are well studied and quantified [41]. The choice of tungsten as the Divertor material for ITER reflects the reliability of the scientific consensus on its behavior [7]. Thus, since the motivation for this research is the observed deviation of tungsten under certain conditions, it is first necessary to quantify the expected results of tungsten under the heat loads and time scales described in the experiments.

For this, an analytical recovery and recrystallization model for tungsten was built to, as accurately as possible, calculate the expected behavior of tungsten under the different temperature regimes and times set in the experiment. The initial assumption is that at steady state loading we can treat each point in the bulk as isothermal. This encompasses all of the bulk minus the sliver of up to 0.2 mm where pulses "penetrate", we can treat each point in the bulk as isothermal, matching the steady state FEM simulations performed. As tungsten, being a bcc metal, has a high stacking fault energy, a pronounced recovery region will precede recrystallization during the annealing process. For the model then, both processes are calculated as independent and concurrent, with the recovery kinetics being described with a logarithmic relationship, and the recrystallization kinetics following the JMAK theory, the same way that has been done in the reference literature [17][45].

To establish the baseline behavior, and due to the lack of a robust database with tungsten's response to different annealing times, Lopez et al. (2015) *Thermal stability of warm-rolled tungsten* [17] is used as reference literature to build the parameters, since the material used (thickness 90% reduced warm-rolled, high purity tungsten from Plansee) has the same characteristics as the ones used during this research. Based on this study an unmodified hardness and fully recrystallized hardness are defined as HV_0 = 434 HV5 and HV_{rex} = 351 HV5 respectively. Both parameters coincide with observed experimental data from the Magnum PSI experiments. Annealing data collected in-situ by the researchers of said study is extracted for the following temperature and times [17]:

- 1100 °C from 18.7 to 169 hours
- 1150 °C from 4.07 to 74.1 hours
- 1175 °C from 3.11 to 33.1 hours
- 1200 °C from 2.54 to 20.1 hours
- 1225 °C from 1.64 to 12.0 hours
- 1250 °C from 1.01 to 12.0 hours

These parameters fall well inside most of the data for the current investigation, and for the lower (400 – 1100 °C), and more importantly, the higher (1250 1500 °C) bounds of the data, the working assumption is that recovery and recrystallization behavior do not change within these ranges. The Hardness measurements used are plotted in Figure 83:

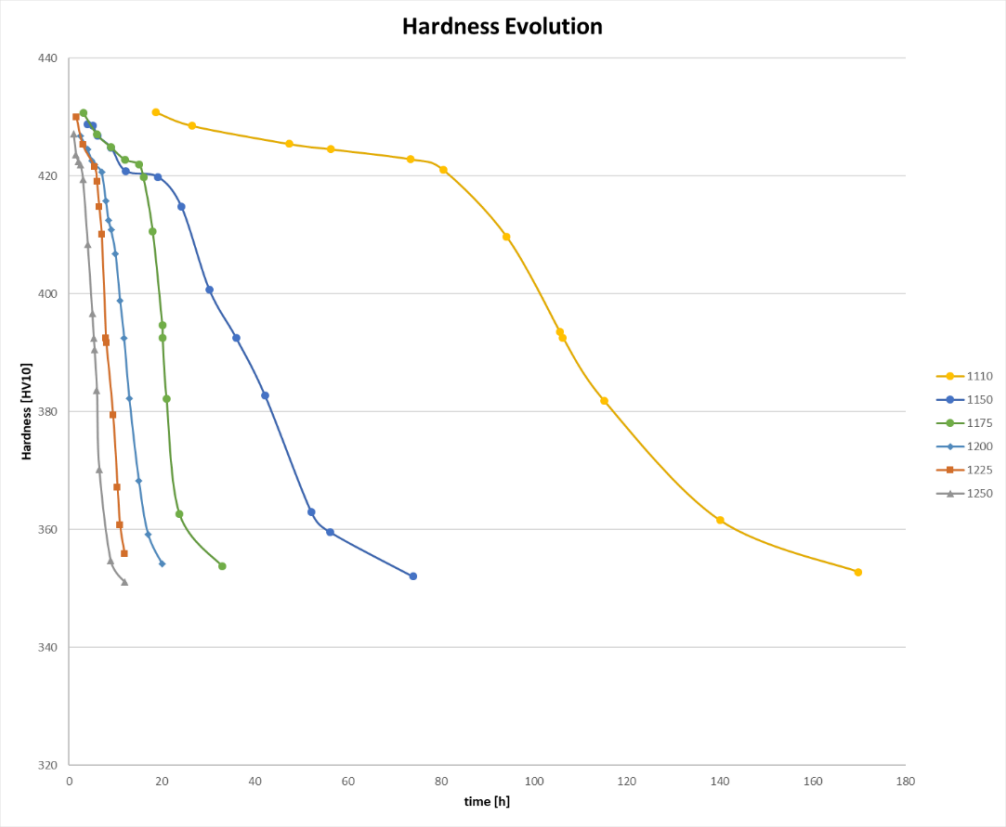

Figure 83. Hardness measurements for W baseline model taken from [17]

7.2.1 Recovery Kinetics

When annealing begins, the material begins to soften, a product of both recrystallization and recovery kinetics taking place. Isolating the recovery kinetics for the moment, the recovered fraction of this softened material f_{soft} [17] (which during recovery amounts only to the recovered fraction) and the recovered rate factor R [45] are calculated based on the hardness HV_t at the relevant time-step t and the defined HV_0 and HV_{rex}:

$$f_{soft} = \frac{HV_0 - HV_t}{HV_0 - HV_{rex}} \tag{7.1}$$

$$R = 1 - f_{soft} \tag{7.2}$$

This calculated recovery follows a logarithmic decay (meaning a rate controlling mechanism dominates the behavior) which can be fitted by [17][45]:

$$R = b - a \cdot \ln(t) \tag{7.3}$$

$$HV_{rec} = HV_0{}^* - C \cdot \ln(t) \tag{7.4}$$

Where HV_0*, b, C and a are the fitting parameters from the linearized equation. The R rate factor for recovery kinetics for the data set used can be seen in Figure 84 with their respective fitting parameters.

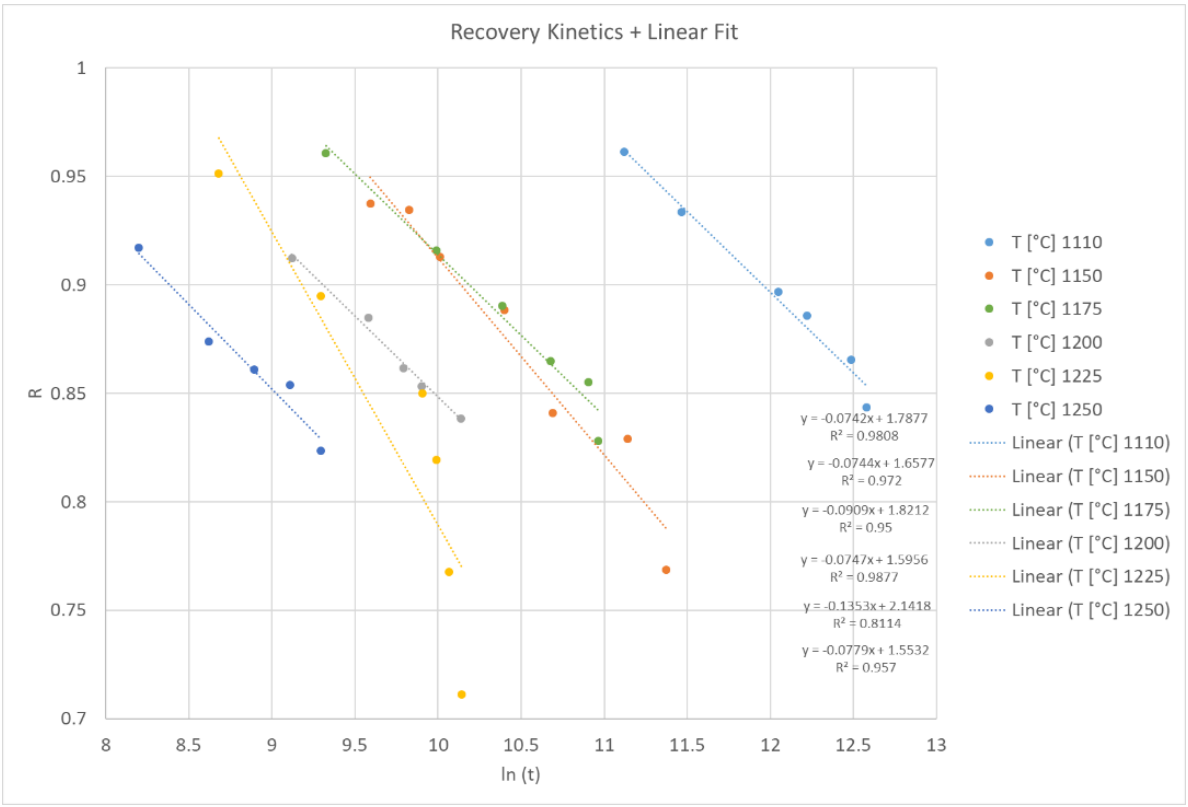

Figure 84. Calculated tungsten recovery kinetics

The slope (coefficient C in equation 7.4) of the linearized equations in Figure 84 represent how fast the recovery occurs at each temperature, with faster kinetics corresponding to higher temperatures. The slope C can be normalized by the annealing temperature to obtain an average C/T coefficient that describes the recovery kinetics of the material [17]. In this case, the calculated C/T value for tungsten is 4.99×10^{-3} HV5 K^{-1}. The same process applied to an average HV_0^* yields 497.04 HV5. This leads to the hardness of the material based on a recovery model for tungsten being calculated as follows [17]:

$$HV_{rec}(T,t) = HV_0^* - \left(\frac{C}{T}\right) \cdot T \cdot \ln(t) \tag{7.5}$$

The above allows to characterize the recovery behavior of tungsten, and subsequently add it to the softening of the material due to recrystallization since, as stated earlier, both are simultaneous processes.

7.2.2 Recrystallization Kinetics

When recrystallization begins, recovery and recrystallization continue concurrently until the matrix is fully recrystallized [17][45][46]. It is generally accepted that there is an incubation time t_{inc} before where recrystallization can be assumed to be zero [17][45][47][46][48].

To be systematic, t_{inc} is calculated by, after each timestep, comparing the R^2 change of the linear fit for the recovery R factor between the current timestep and the previous one, R^2_t and R^2_{t-1} until the R^2 change is more than 0.1 or the R^2 value itself is less than 0.8. The time t at which this happens is deemed t_{inc} and the new "zero" time for recrystallization to begin is defined as:

$$\tau = t - t_{inc} \tag{7.6}$$

This method is of course highly sensitive to the spacing between the measurements during the data gathering stage. Having defined τ, as time progresses from this point onward, the softening of the material can be ascribed to recovery and to recrystallization processes by the rule of mixtures, where f_{rex} is the fraction of the material softened by the recrystallization process [17]:

$$HV_\tau = (1 - f_{rex}) \cdot HV_{rec} + f_{rex} \cdot HV_{rex} \tag{7.7}$$

Equation 7.5 is substituted into equation 7.7 incorporating the recovery kinetics in the calculation of the recrystallized fraction. Here, after rearranging, f_{rex} is obtained as:

$$f_{rex} = \frac{\left[HV_0{}^* - \left(\frac{C}{T}\right) \cdot T \cdot \ln(t)\right] - HV_\tau}{\left[HV_0{}^* - \left(\frac{C}{T}\right) \cdot T \cdot \ln(t)\right] - HV_{re\tau}} \tag{7.8}$$

As defined earlier in this work, due to the thermally activated nucleation and growth nature of recrystallization, the JMAK theory of nucleation (see equation 3.1) is used to characterize the recrystallization behavior starting at τ. Based on previous experiments and literature, the modified JMAK equation taking into account a constant nucleation rate regime used for this model is [17] [45]:

$$X = 1 - \exp(-b^n \cdot t^n) \tag{7.9}$$

Where b^n is equivalent to B in equation 3.1 but b is now a constant and not dependent on the Avrami exponent n from equation 3.3, and X is the model-calculated recrystallization fraction. These values are now calculated for the dataset in the isothermal from τ onward (after t_{inc}) and thus consider the effects when recrystallization starts to become dominant; because of that they have the subscript τ. To obtain b and n, the collected f_{rex} is used instead of X in equation 7.9, and then that equation is linearized so that B_τ and n are fitted below (with $B_\tau = b^n$) [17]:

$$\ln\left(\ln\left(\frac{1}{1-f_{rex}}\right)\right) = \ln(B_\tau) + n_\tau \cdot \ln(\tau) \tag{7.10}$$

Equation 7.10 is applied to every isothermal data set to get a group of n_i and B_i (and thus a value for b_i as well) where i is the number of isothermal data sets used for the building of the model. With this cumulative fits, the obtained values for n_i are averaged out as $\bar{n}$. This new $\bar{n}$ is used to calculate a new B_k that represents B_τ for the whole set of isothermal curves. It is calculated from the averaged y and x from the linear equation 7.10 of each isothermal set as follows, where m is the number of data points in each isothermal set [49]:

$$\bar{y} = \frac{\sum_j^m \left\{\ln\left(\ln\left(\frac{1}{1-f_{rex}}\right)\right)\right\}_j}{m} \tag{7.11}$$

$$\bar{x} = \frac{\sum_j^m \{\ln(t)\}_j}{m} \tag{7.12}$$

$$B_k = \frac{\bar{y}}{m} - \bar{n} \cdot \frac{\bar{x}}{m} \tag{7.13}$$

$$B_k = {b_k}^{\bar{n}} \tag{7.14}$$

By using the above derived parameters an analytical calculation for each of the isothermal i data sets is done. These calculations agree with the experimental measured data as seen in Figure 85, giving reasonable confidence in the JMAK model used to describe the recrystallization kinetics.

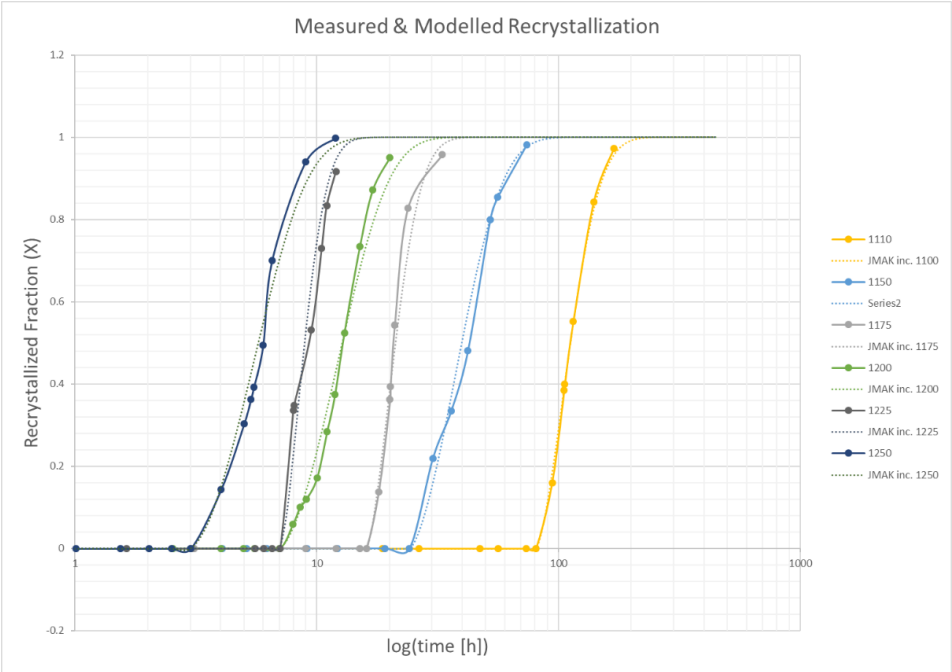

Figure 85. Measured recrystallization fraction [17] *superimposed with calculated recrystallized fraction*

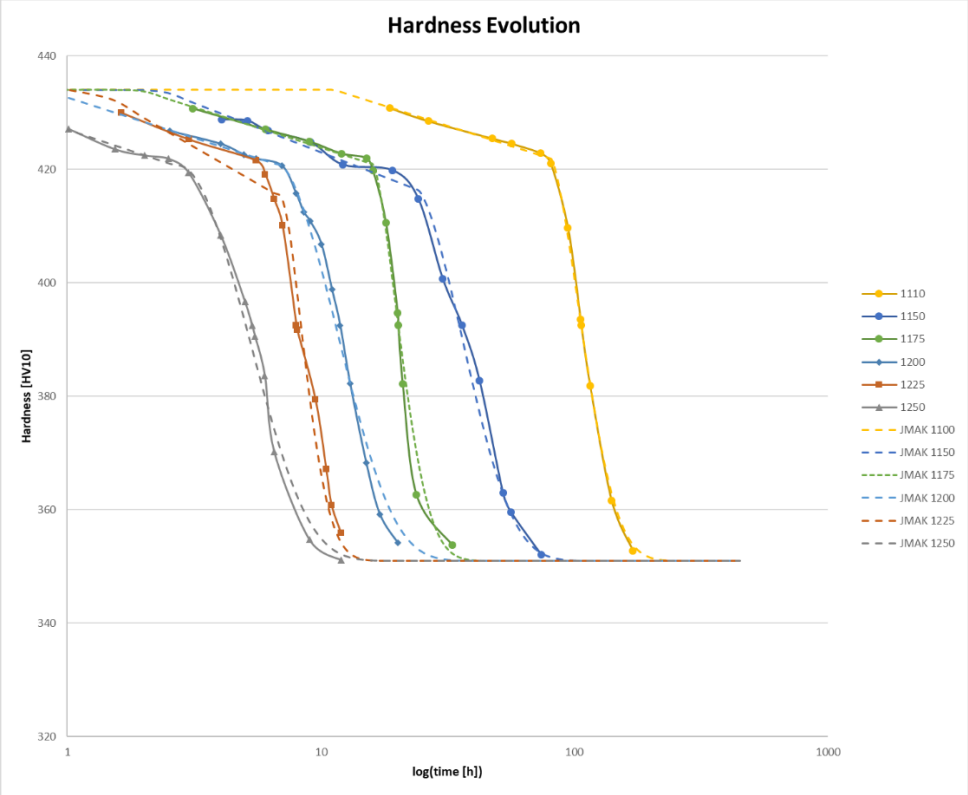

Figure 86. Original hardness measurements [17] *superimposed with calculated fraction (dashed lines) evolution from model (Recovery +Recrystallization)*

The above method gives sufficient information to lay a plot of the different activation parameters of the recrystallization process. The activation parameters follow a temperature (T) dependent Arrhenius relationship as exemplified below [17][45][47][49]:

$$t_z = A \cdot \exp\left(\frac{Q_z}{RT}\right) \tag{7.15}$$

Where R is the universal gas constant, A is a rate controlling material dependent parameter, t_z the time for the parameter z of interest, and Q_z is the activation energy of the different significant parameters to characterize recrystallization kinetics. These parameters are obtained from the JMAK calculations of each isothermal. The Arrhenius-like behavior of these parameters permits a straight line to be fitted through them in a plot of them against the inverse of T, with the slope of each line being their corresponding activation energy Q_z. An analytical model for can then obtained for each of them at every desired temperature. Thus, the parameters of interest are [17][47]:

- $t_{HV/2}$: Time to achieve loss of half of the material's hardness. This is direct data from experimental samples, and serves to corroborate the model's accuracy.

- $t_{X/2}$: Time to achieve half recrystallization based on the described model. This should reasonably coincide with $t_{HV/2}$ and corresponds to the moment when recrystallization kinetics are at their fastest (highest slope on the "S-shape" recrystallization curve).

- t_{inc}: Incubation time for recrystallization kinetics to start with concurrent recovery kinetics. Before this point in time, all softening is ascribed to recovery mechanisms.

- b^{-1}: Inverse Avrami coefficient b that describes thermal activation of the nucleation and growth mechanics of recrystallization, independent of the Avrami exponent *n*.

The results of the Arrhenius plot and the activation energies are seen in Figure 87 and table 9:

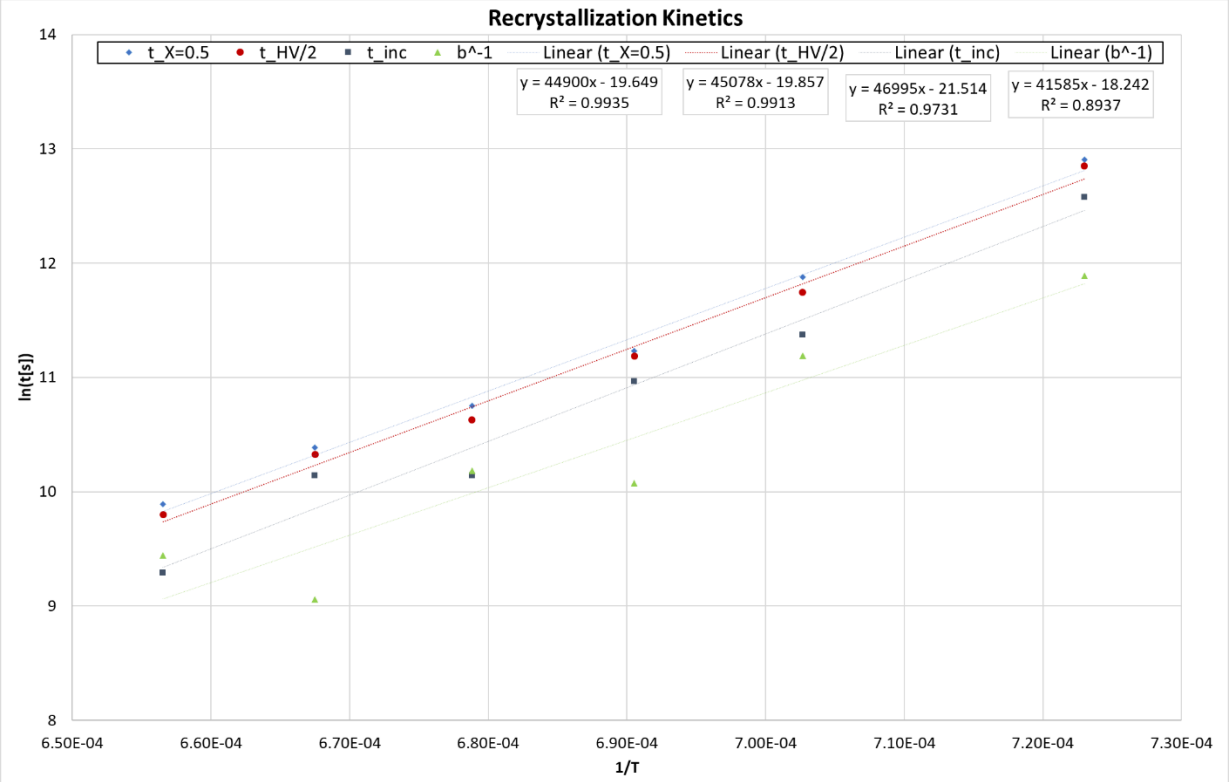

Figure 87. Calculated temperature dependence for $t_{HV/2}$, $t_{X/2}$, t_{inc} and b^{-1}

Process	Arrhenius Slope (Q/R) [K]	Q [kJ mol^{-1}]	ln(A) [ln(s)]	R^2
Q_$t_{HV/2}$	44900	373.32	19.65	0.99
Q_$t_{X/2}$	45078	374.80	19.86	0.99
Q_t_{inc}	46995	390.74	21.51	0.97
Q_b^{-1}	41585	345.76	18.24	0.89

Table 9. Activation energies for $t_{HV/2}$, $t_{X/2}$, t_{inc} and b^{-1} extracted from Figure 87 calculations

The relevant parameters for modelling the system have now been obtained either with a temperature dependent relationship (see figure 83 and table 9) or by averaging the n_i Avrami exponents from equation 7.9 to obtain $\bar{n}$ = 1.45 for this system.

With these final Temperature dependent parameters, a full model based on the JMAK equations for calculating the recrystallization fraction through time at an arbitrary temperature based on equation 7.8 can be explicitly employed:

$$X(T,t) = 1 - \exp\left(-b(T)^{\bar{n}} \cdot \left(t - t_{inc}(T)\right)^{\bar{n}}\right) \tag{7.16}$$

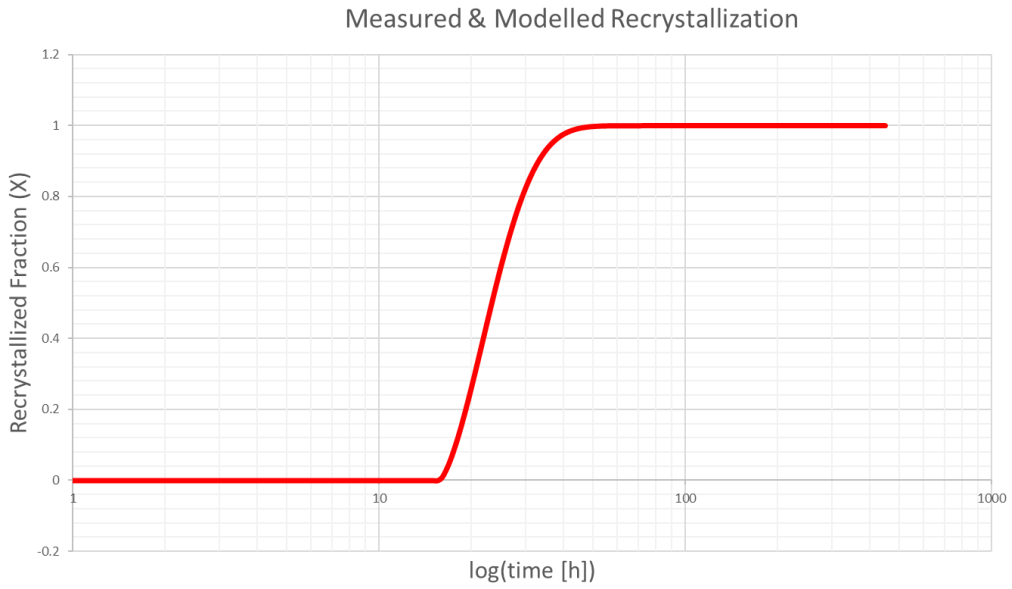

Figure 88. Example of recrystallization curve of tungsten at an arbitrarily chosen temperature of 1175 °C based on model described by Equation 7.16

7.2.3 Recrystallization model vs. experimental data comparison

By applying equation 7.1 to the hardness measurements from Chapter 6, the isochronal softening behavior for 1 hour exposed tungsten can be observed in the softened fraction calculations from Figure 89. As previously noted, recrystallization appears to be abrupt in arrange between 960 °C and 990 °C.

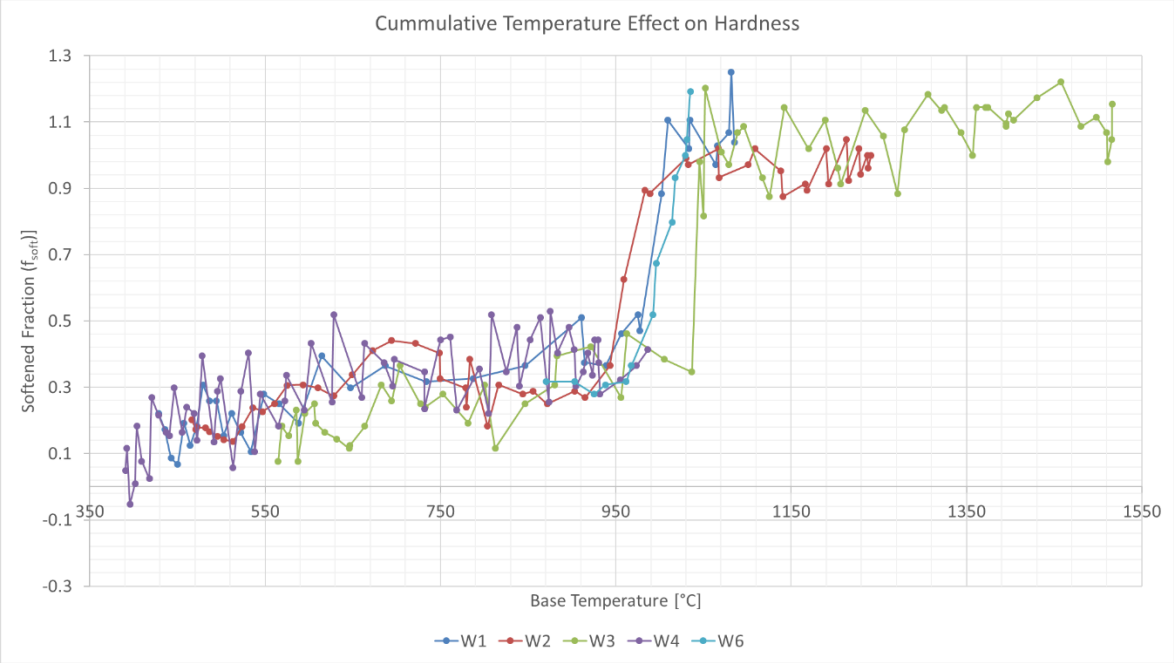

Figure 89. 1h plasma exposed samples' compiled softening behavior

Now, making use of the model described by equations 7.4 and 7.16, an isochronal recovery and recrystallization behavior curve for 1 hour is delimited for the range 300 – 2700 °C which falls within the steady state temperatures recorded from the appropriate sample temperature mappings developed in Chapter 6. The full expansion for the model applied to equation 7.4 and 7.16 based on the above calculated values is seen in equations 7.17 and 7.18.

$$X(T,t) = 1 - \exp\left(-\left[\left(\exp\left[41585\,K\frac{1}{T} - 18.242\right]\right)^{-1}\right]^{1.4552} \cdot \left(t - \exp\left[46995\,K\frac{1}{T} - 19.857\right]\right)^{1.4522}\right) \tag{7.17}$$

$$HV_{rec}(T,t) = 497.04\,HV5 - (4.99 \times 10^{-3}\,HV5\,K^{-1}) \cdot T \cdot \ln(t) \tag{7.18}$$

The values obtained for the temperature range described above after 1 hour of exposure are for HV_{rec} and X are used in equation 7.7 to find HV_{τ} and then in equation 7.1 to obtain the predicted f_{soft}. The result is plotted in Figure 90.

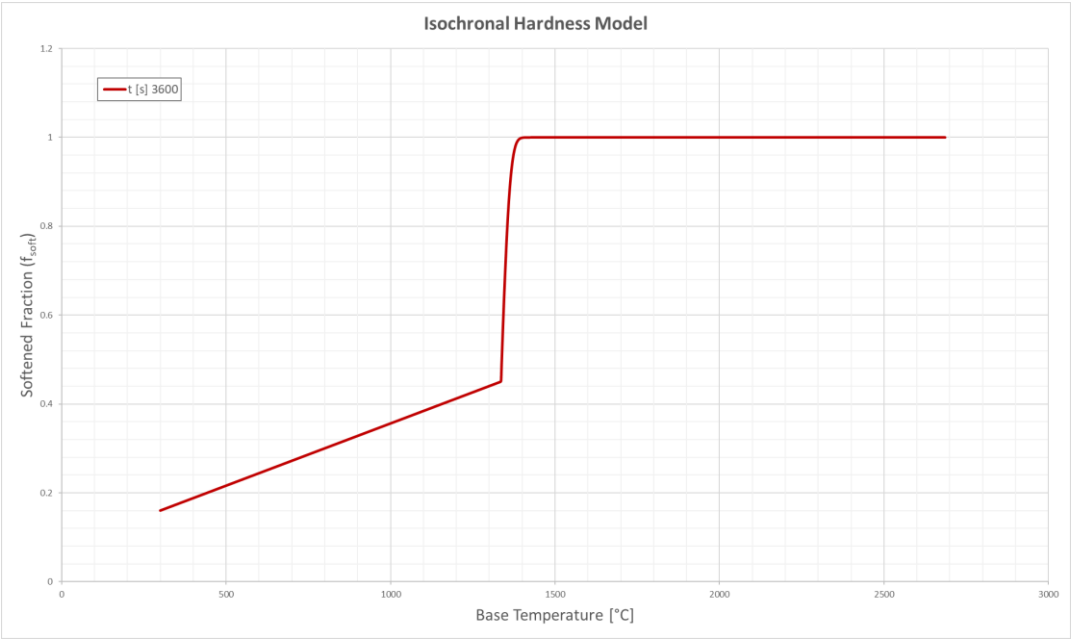

Figure 90. Tungsten softening expected behavior after 1 hour for the 300 – 2700 °C range

The model illustrated above shows that, after exhibiting recovery and then recrystallization dominant behavior, tungsten should be half recrystallized at ~1340 °C, with noticeable recrystallization (X>1%) appearing at ~1310 °C and the process noticeably being complete (X<99%) at ~1400°C. As demonstrated in sections 7.1 – 7.2, this model describes with fair accuracy the recrystallization behavior of tungsten when annealed in a furnace.[17] By superimposing the data from figures 89 and 90, it is abundantly clear that the recrystallization threshold for the plasma exposed tungsten in this research is much lower than that of tungsten annealed by conventional methods.

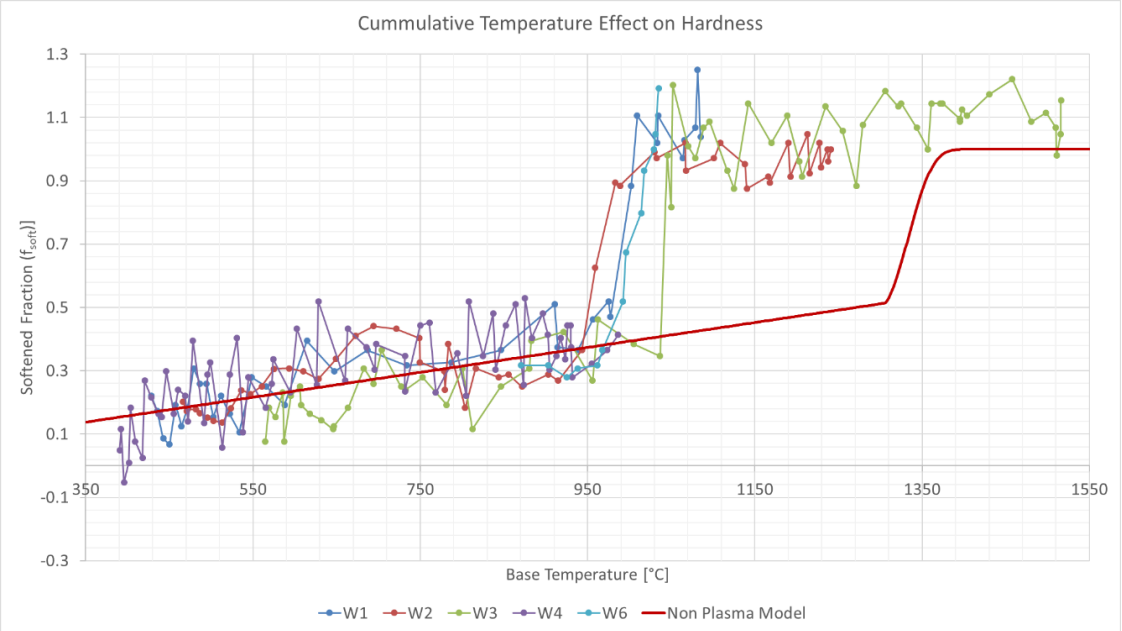

Figure 91. Tungsten experimental vs. predicted softening behavior

Recovery kinetics appear to follow the expected behavior, but the scattering of the hardness data is too large to make any conclusive remarks about it. On the other hand, recrystallization behavior contradicts the starting hypothesis that originated this project, which was that plasma loading the material would show retarded recrystallization behavior. Nevertheless, the hypothesis did call for a deviation in expected recrystallization behavior, so the planned next step was to model the observed behavior to extract meaningful information from the experiments. Based on the above and the scope of this project, the following development centers solely in the recrystallization model redevelopment.

First, the fitted model described in equation 7.16 is simplified to be able to find the parameters that best describe the experimental data. This is done, because the time dependent fitted parameters cannot be directly recalculated since the experiments for this work were done under isochronal conditions. Table 9 and Figure 87 show that the different activation energies calculated using the Arrhenius relation in equation 7.14 have activation energies and *A* coefficients in the same range. This has been corroborated on different tungsten grades, other materials and under different conditions in previous studies [17] [45][47][46][48] [49]. By replacing the energy terms in Equation 7.16 (b and t_{inc}) a similar model can be used, which only depends on three coefficients to be determined: Q_z, A and n.

$$X(T,t) = 1 - \exp\left(-\left[\left(\exp\left[\frac{Q_z}{R}\frac{1}{T} - \ln(A)\right]\right)^{-1}\right]^{n} \cdot \left(t - \exp\left[\frac{Q_z}{R}\frac{1}{T} - \ln(A)\right]\right)^{n}\right) \qquad (7.19)$$

For the Avrami exponent n, it has been reported in the literature that it is weakly dependent on temperature and that its value oscillates between 1 and 2. During the building of this model, *n* was varied from 1 to 2 and this trend was confirmed, thus for simplicity, *n* will be kept at its originally calculated value of $n = 1.45$ [17][49].

To corroborate the validity of this approach, the "simplified" model from equation 7.19 was compared to the original from equation 7.17. Q_z and $ln(A)$ were taken as the average of the calculated ones for Q_b^{-1} and Q_t_{inc} from Table 7 so that $Q_z/R = 44290$ K ($Q_z = 368$ kJ mol^{-1}) and $ln(A) = 19.88$. Both models agree well as evidenced in figure 92.

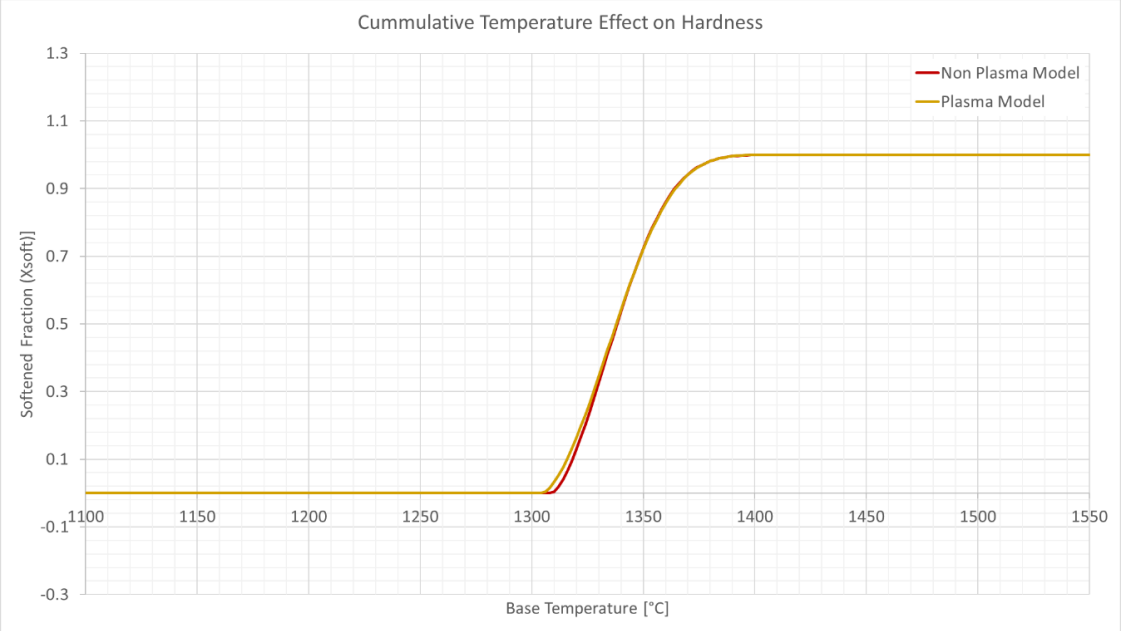

Figure 92. Original and simplified recrystallization model comparison

In the literature, it is evidenced that Q_z and *ln(A)*, are very strongly dependent with temperature, and the recrystallization fraction predicted by the model is very sensitive to them. Given that the frequency factor *A* is dependent on the material properties as determined by the manufacture process, and that as seen earlier *ln(A)* is mostly constrained by a small variation between 18 and 21, for the completion of this model it will be assumed that the variation of this parameter will not exceed 100% of its original range (~ ±3) as seen in Table 9 earlier. Starting with the lower end of the *ln(A)* threshold, the parameters that were found to match the observed recrystallization behavior are shown in Table 10.

ln(A) [ln(s)]	**Arrhenius Slope (Q/R) [K]**	**Q [kJ mol^{-1}]**
15	28400	236.13
17	30900	256.91
19	33400	277.70
21	35900	298.49
23	38400	319.27

Table 10. Proposed recrystallization kinetics parameters

This behavior is described by the Meyer – Neldel isokinetic or compensation rule (equation 7.20 where *c* and *d* are the linear fitting parameters for the data) which implies that the material has a mechanism to compensate having to overcome large activation energies during thermally activated processes by concurrently increasing the jumping frequency. Although there is no consensus on the physical explanation for the phenomena (phonon absorption and reemission by diffusing atoms has been proposed as its origin), it has been widely documented in several Arrhenius-like processes, like diffusion and electrical conductivity of bcc metals [50][51]. Tungsten has been observed to follow the Meyer – Neldel compensation rule for other thermally activated process like melting and dissociation [52]. Based on this observed

behavior, the resulting proposed kinetics from the data in table 10 are shown in Figures 93 and 94.

$$\ln(A) = c + d \cdot Q_z \tag{7.20}$$

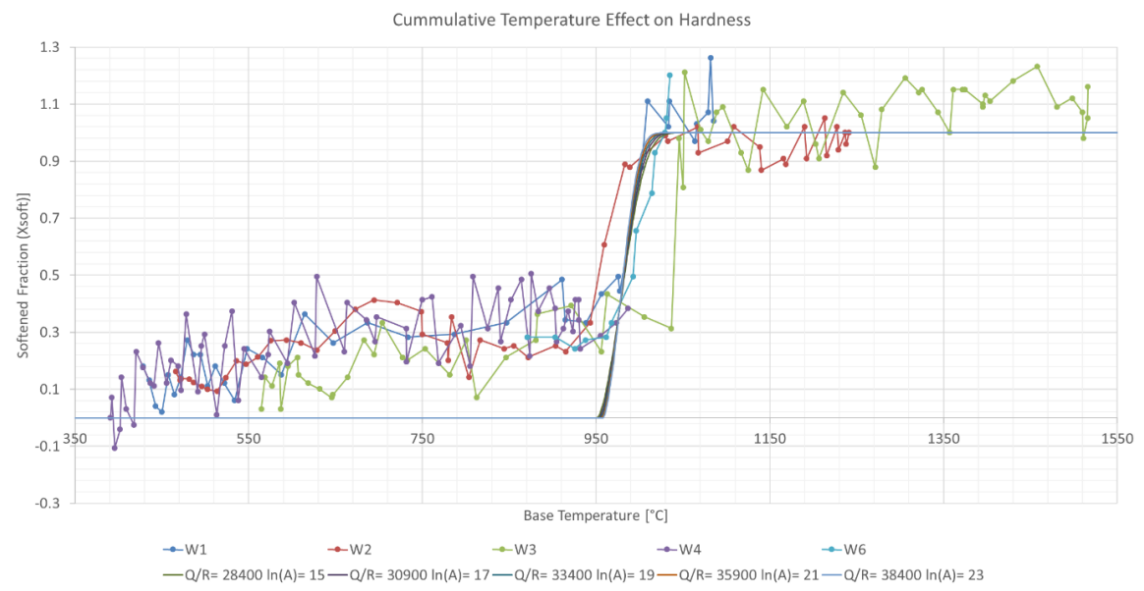

Figure 93. Measured softening fraction versus proposed recrystallization models (values based on Table 10)

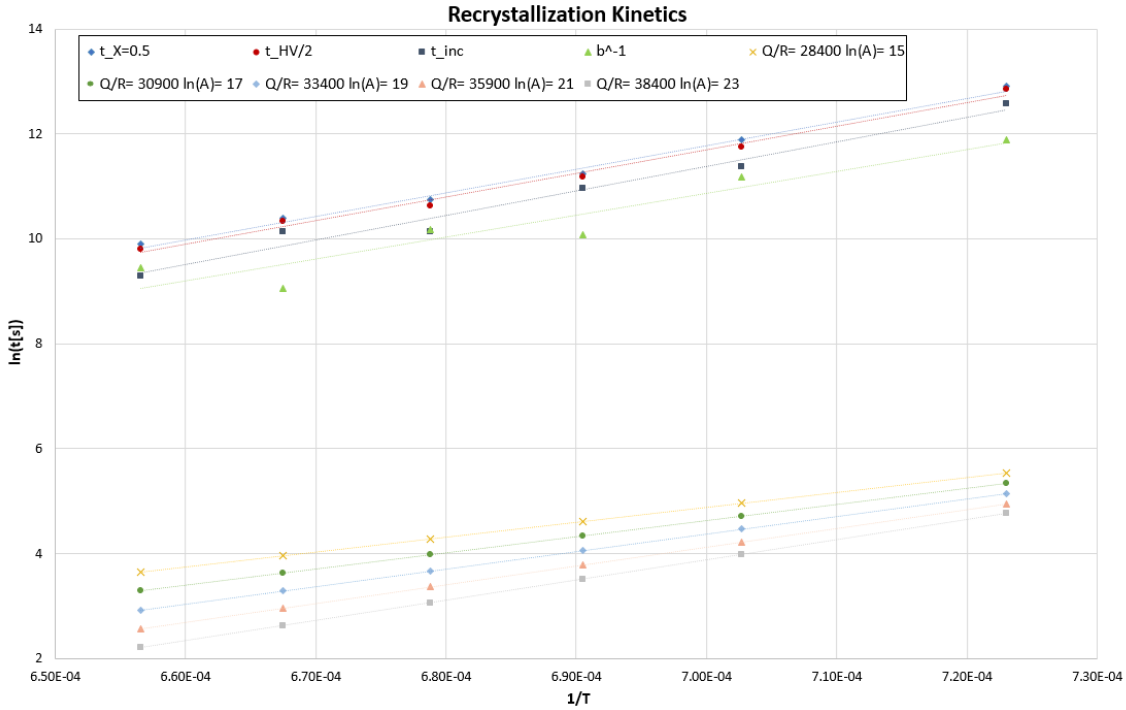

Figure 94. Calculated recrystallization kinetics for H loaded W versus furnace annealed W (values based on Table 10)

The model illustrated in Figures 92 – 94 satisfactorily follows the observed recrystallization behavior, and shows that after 1 hour of exposure tungsten should be half recrystallized at ~980 °C, with noticeable recrystallization appearing at ~960 °C and the process noticeably being complete at ~1020°C. Adding the recovery model back and using the calculated values in this section and equation 7.19 instead of equation 7.17 shows that the new predicted behavior matches the measured tungsten softening from the 1 hour plasma exposure. The new model along with the measured fraction are shown in Figure 95.

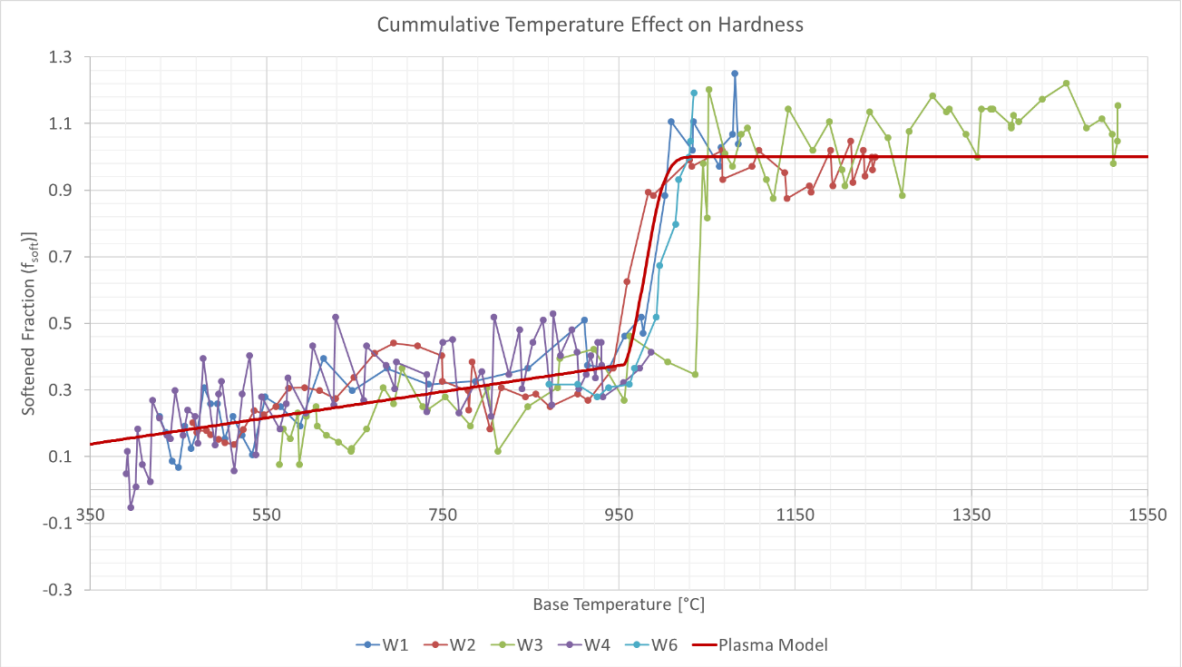

Figure 95. Tungsten experimental vs. updated model's predicted softening behavior

To analyze the recrystallization behavior of sample W5, which was exposed to 1500 °C plasma at the strike point, the same analysis was performed for 4 hours of annealing. Based on the devised recrystallization model from the furnace annealing data, the half recrystallization threshold should be at ~1260 °C, with noticeable recrystallization appearing at ~1240 °C and the process noticeably being complete at ~1300 °C. Likewise, based on the recrystallization kinetics calculated for 1 hour of H plasma exposure, the new model was applied and yielded a recrystallization threshold of ~920 °C. When compared to the measurements taken on W5, the data shows that there appears to be full recrystallization in all of the measured range of ~700 – 1200 °C. These data measurements were taken both at the exposed surface and close to the surface opposite of the exposure.

At first glance this decrease in recrystallization temperature seems too extreme. To confirm that there was no missed lack of contact (as is hypothesized in W3) a sensitivity analysis was done on the FEM simulation for W5. Since tungsten and copper's thermal properties are well known and characterized [41] the thermal contact variation was done on the grafoil properties. Contrary to the W3 case, W5 has no obvious changes in the bulk morphology to guide the analysis. To get around this, and to make a more robust assessment, this analysis was done also

for sample W1 since in this sample there is a clear visual isothermal line that coincides with the visually identified recrystallization line shown in Figure 56. The overall grafoil conductivity was decreased by a factor of 3, 6, 20 and 100 and the FEM simulation rerun to simulate different severities of decreased thermal contact. The points chosen for each sample were:

- W5: lowest temperature-hardness pair recording
  x: -14mm y: -3mm T_{orig}: 667.5 °C

- W1: deepest point of the identified recrystallization line
  x: 0mm y: -1.9mm T_{orig}: 982.3 °C

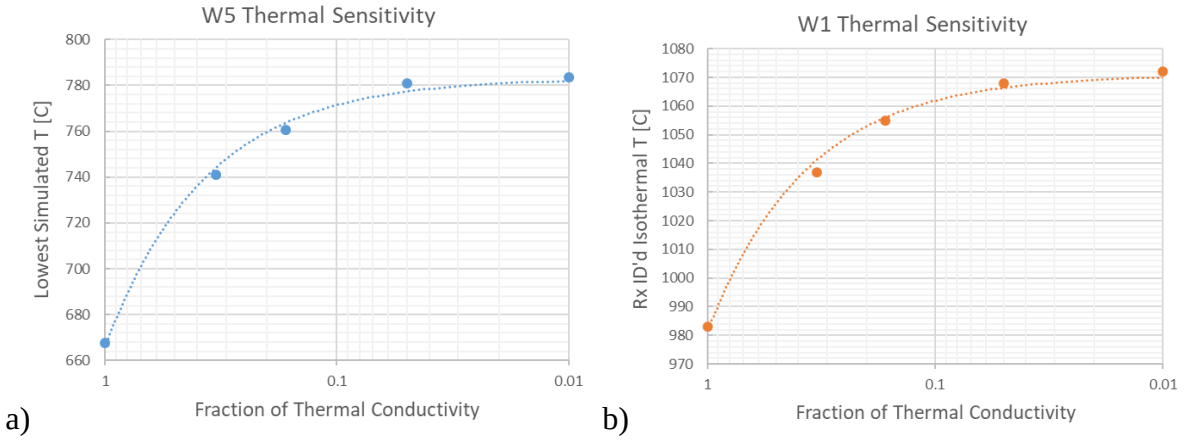

Figure 96. Thermal contact sensitivity analysis showing the increase of the recorded temperatures as thermal conductivity is reduced for a) W5 and b) W1

Unsurprisingly, hindering the thermal conductivity increases the temperature, but this effect plateaus quickly, with a maximum temperature increase of ~100 °C on both samples for the most extreme case tested (see Figure 96). Thermal isolation between the tungsten and the grafoil would approach total detachment for the temperature to shift enough in W5 so that the recrystallization kinetics match the behavior of the 1h plasma exposed samples, so, it can be concluded that the FEM calculated temperatures are accurately representing the bulk section of the samples. Since W5 was the only sample exposed for 4 hours, there is not enough data to properly fit the recrystallization behavior. Nonetheless, based on the minimum measured temperature at which full recrystallization was detected, the process described through section 7.2 can be used to estimate the maximum activation energy of the material under these conditions. The results show that, using the same calculation methods, the activation energy cannot be higher than ~212 kJ mol^{-1} (Q/R = 25500 K). The three models versus the measured recrystallization fraction for W5 are shown in Figure 97:

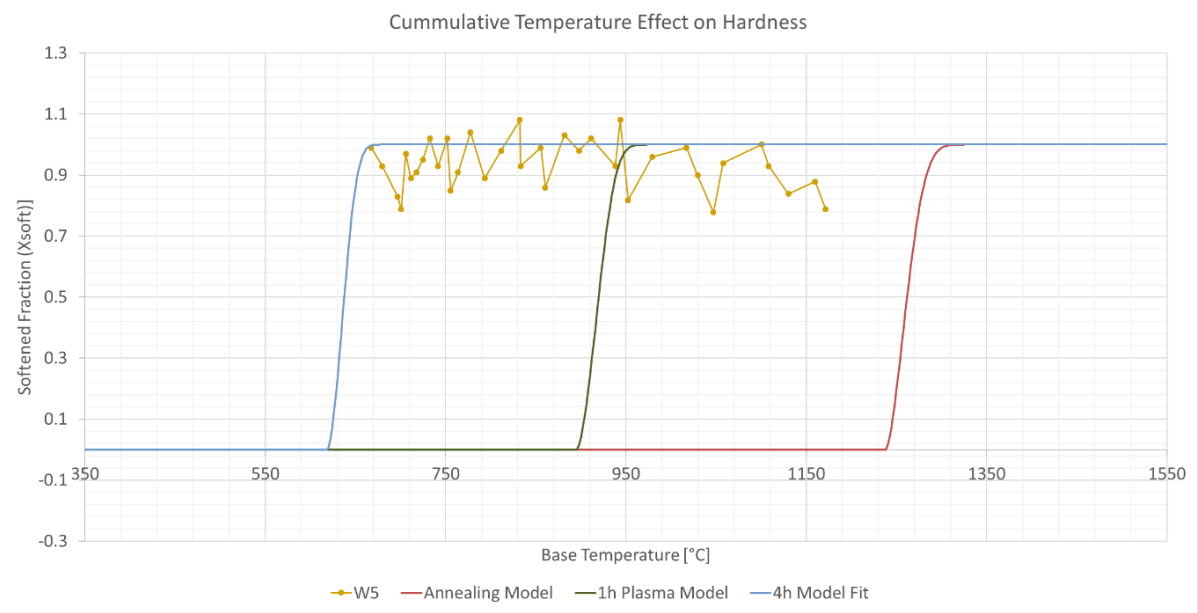

Figure 97. W5 Measured softening fraction versus different calculated recrystallization models: furnace annealing, 1h plasma exposure and 4h plasma exposure

To confirm if what is observed from these calculations is in fact a change in the recrystallization kinetics for each set of samples, the calculated recrystallization kinetics were analyzed using the Meyer – Neldel rule described earlier in equation 7.18. The results show that as described previously, the 1 hour plasma exposure samples obey the Meyer – Neldel rule, the 4 hour exposure proposed parameters do as well (unsurprisingly as the method used was the same as for the 1 hour exposure), and the furnace annealed measurements also show a Meyer – Neldel relationships. These relationships are plotted in Figure 98.

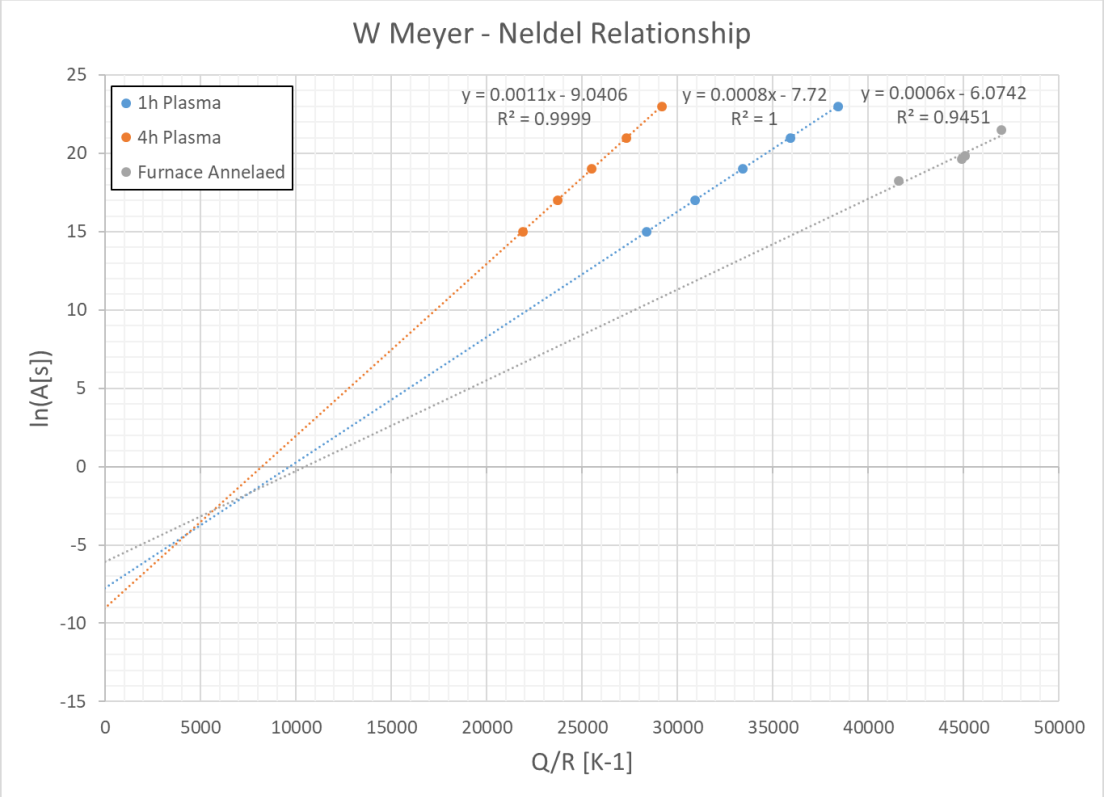

Figure 98. Recrystallization Meyer Neldel relationships for of W under different loading conditions

The Meyer – Neldel plot shows that the recrystallization behavior of tungsten proposed in this work obeys the Meyer – Neldel rule under the different loading regimes, but this relationship changes for each type of loading / exposure regime. As hydrogen loading time increases, the kinetics noticeably accelerate, as evidenced by the steepening of the slope on each regime.

Based on the above analysis and contextualizing the Meyer – Neldel behavior, it can confidently be asserted that the activation energy of recrystallization for tungsten under hydrogen plasma loading for one hour is 280 ± 40 kJ mol^{-1}, and for 4 hours plasma loading, cannot be above the 210 ± 30 kJ mol^{-1} range. These values are much lower than the 345 – 373 kJ mol^{-1} that were calculated from annealed W under furnace conditions [17]. The result of these calculations show that the activation energy clearly decreases substantially with hydrogen plasma exposure from furnace annealing behavior. Additionally, increasing the time of hydrogen exposure from 1 hour to four lowers the activation energy by 23 – 24%.

Moreover, bulk self-diffusion in tungsten is reported to be in the 526 – 628 kJ mol^{-1} range [53] and would not explain the atomic jumping mechanism. Grain boundary diffusion in tungsten is reported to have an activation energy of 377 – 460 kJ mol^{-1} [53], which would explain the atomic jumping mechanism of the furnace annealed material as being GB-diffusion dominated, but it is at least 1.5 times larger than the activation energy calculated for the plasma loading. Other sources show a GB activation energy of 210 ± 13 kJ mol^{-1} calculated via recrystallization kinetics based on grain size [54], and of 234 – 294 kJ mol^{-1} measuring the diffusion of tracer radioactive isotopes of ^{185}W [55]. These last measurements were done on fully recrystallized and highly deformed tungsten respectively (both with similar purity to the samples in this

work), and both better agree with the measured recrystallization activation energy from this work.

It can be inferred from the above that during furnace annealing in the studied regimes, recrystallization occurs via a mixed process of bulk and grain boundary diffusion, and that the measured activation energy of 377 – 460 kJ mol^{-1} [53] corresponds to this mixed regime. The conditions of the hydrogen plasma loading experiment, on the other hand, are suppressing the bulk diffusion mechanism and accelerating the grain boundary diffusion. Figure 99 shows how the measured plasma kinetics fall between the reported bounds for W GB diffusion.

Even if the preferred diffusion mechanism changes from the established one (be it bulk, diffusion or mixed) when in the presence of hydrogen plasma, which can be seen comparing the furnace annealed with the 1 hour plasma samples, this alone would not explain the dip in activation energy / accelerated recrystallization kinetics evidenced by the four hour exposure. This result points to the hydrogen actively lowering the activation energy for grain boundary diffusion and thus recrystallization independently of the jumping rates with the constraints described in this section.

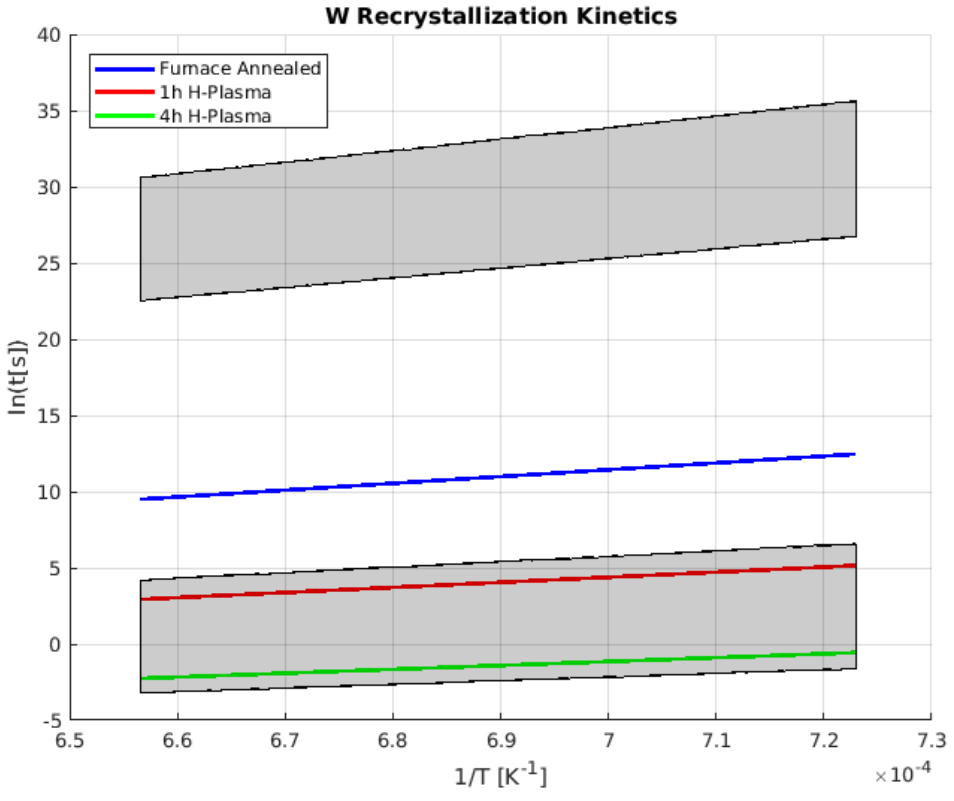

a)

b)

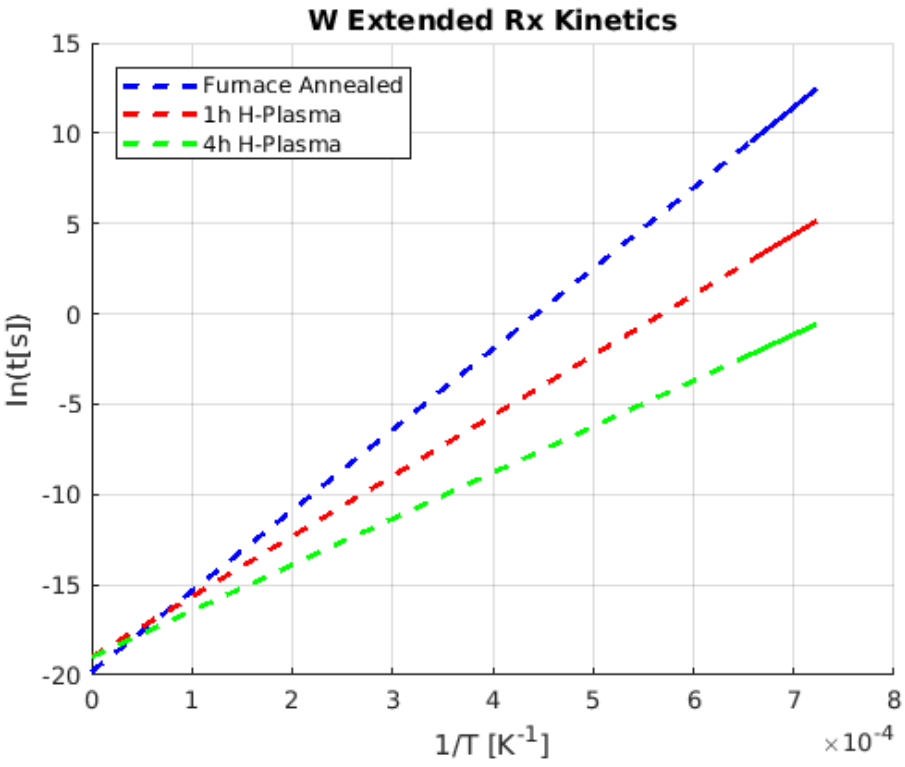

Figure 99. a) Recrystallization kinetics of W under different loading conditions showing how plasma exposed samples' behavior fall within the reported GB diffusion kinetics range and b) extended plot better showing slope change (solid lines: measured range from (a), dashed lines: extrapolated values) [53][54][55]

7.3 Hydrogen concentration and diffusion

As seen in section 6, hydrogen concentration ranges from ~10^{-8} to 10^{-7} across the bulk after quickly saturating. These saturated levels were kept for about an hour (four hours in the case of W5), so it is reasonable to assume them as the dominating levels on any analysis regarding the concentration. Following the hypothesis, that H from the plasma interacts with the tungsten in such a way that recrystallization kinetics are affected, the H concentration was simulated on the plasma beam's strike point across the bulk. The surface temperature across this area on the different targets ranges from ~1000 to 1500 °C (~1300 – 1800 K). The final saturation values from Figure 79, section 6.4.3 show that for the same exposure time there is no clear temperature dependence on the concentration profiles.

By going a step further and plotting the exposed temperature and particle flux (Figure 100) it is clear that the particle flux exposure was not uniform or consistent. It is the case that at higher particle flux, the concentration will generally be higher (higher initial concentration). Also higher temperatures enable the hydrogen atoms to diffuse out of the material more quickly, which causes the decay of concentration across the depth to be steeper. All this is consistent with the expected qualitative behavior under equations (3.13 – 3.15).

For a better understanding of the role of hydrogen in the tungsten bulk, it would be beneficial to be able to fix the particle flux at the desired temperatures, or vary this parameter in a consistent way to be able to filter out the effect of the combination of these factors. In practice,

maintaining the surface temperature stable in Magnum-PSI required constant modification of parameters such as gas flow, current and electric field; so in reality this ideal experiment setup might be impractical to implement.

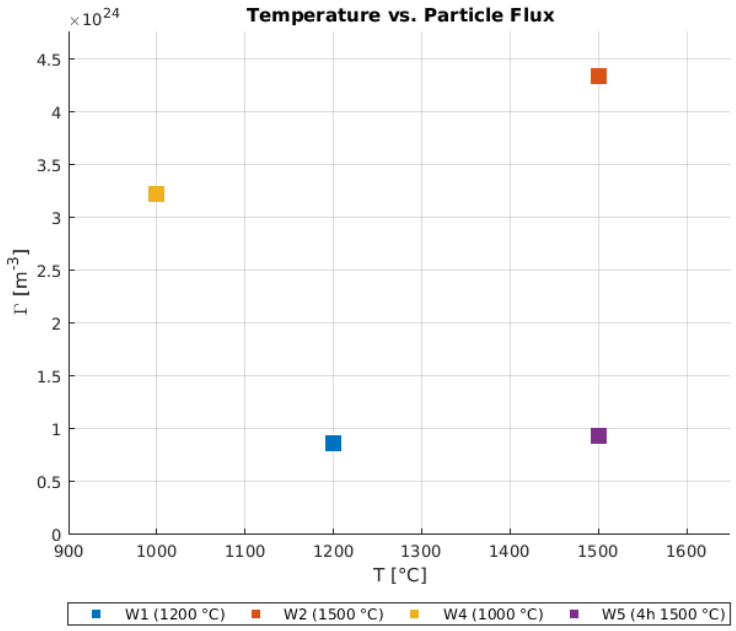

Figure 100. Surface temperature vs. surface particle flux on exposed samples

Correlating these results with recent studies by Schmidt et al. [44] and Hendrika et al. [30] it appears that there is no substantial hydrogen trapping in the regions where we see accelerated recrystallization. As mentioned in section 3, the effect of traps on the diffusion (D_{eff}) of H is dependent on the temperature of the matrix. Equation 3.9 can thus be rewritten as [44]:

$$\frac{D_{eff}}{D_{perf}} = \frac{1}{1+c_{trap}\exp\left(\frac{E_{trap}}{k_B T}\right)} = \frac{1}{1+\Omega} \tag{7.19}$$

This lets show the effectiveness of the H concentration in affecting the diffusion in the material. Diffusive transport is substantially affected or even dominated by trapping mechanisms when $\Omega >> 1$, which would lead to a small D_{eff} / D_{perf} ratio. As seen in Figure 101, the temperature ranges and calculated hydrogen concentrations where the accelerated recrystallization was observed, bulk fall mostly in the $1/(1+\Omega) \approx 1$ [44].

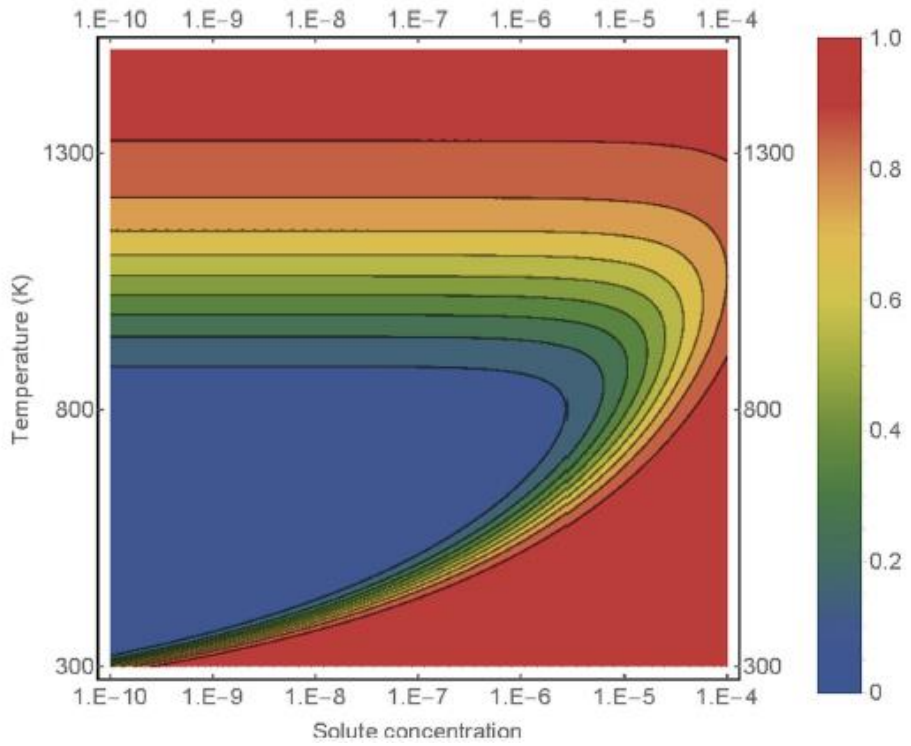

Figure 101. Effective diffusion coefficient 1/(1+Ω) of H in W for different concentration vs. temperature regimes [44]

The above entails that actually, for the regimes in the strike point $\Omega << 1$, which means that since $D_{eff} \approx D_{perf}$, it is only depending on the Temperature and not the hydrogen concentration. This also signifies that all traps are effectively empty during the exposure, and that the hydrogen is diffusing through the material virtually unimpeded until the bulk reaches ~900 °C [44]. This points towards the hydrogen that is present in the bulk, not acting as solute drag, due to its inability to be captured by the material's traps, at least in the areas where accelerated recrystallization was observed.

7.4 Hypothesis Rejection

The initial goal of this project was to understand and characterize the observed higher recrystallization resistance of tungsten when loaded with Plasma compared to other methods such as electron beam and annealing. Going back to the initial research that originated this investigation, Loewenhoff et al. [1] exposed W samples to H plasma for ~2000 seconds at a T_{base} of ~1200 °C and ~1500 °C and expected half recrystallization to occur at ~1300 °C. Using the model devised in section 7.1, the expected recrystallization temperature should be ~1370 °C, so their assumptions were reasonable. The results showed that there was no change in the microstructure of either sample, which led to the conclusion that the hydrogen plasma had retardation effects on the recrystallization mechanics and should be studied further [1].

Cheng et al. [36] found a similar behavior when exposing tungsten samples to Helium plasma for 1 hour at different temperatures in the range of 1000 – 1700 °C and found a half recrystallization temperature of ~1370 °C on their exposed samples versus ~1200 °C on their unexposed (furnace heated) samples. On this study the difference was not overwhelming, but the trend showing recrystallization enhanced behavior was clear. Their findings were further

confirmed by trapped Helium bubbles in the grain boundaries leading to their hypothesis that Helium acting as Zener pins were the cause of this phenomenon.

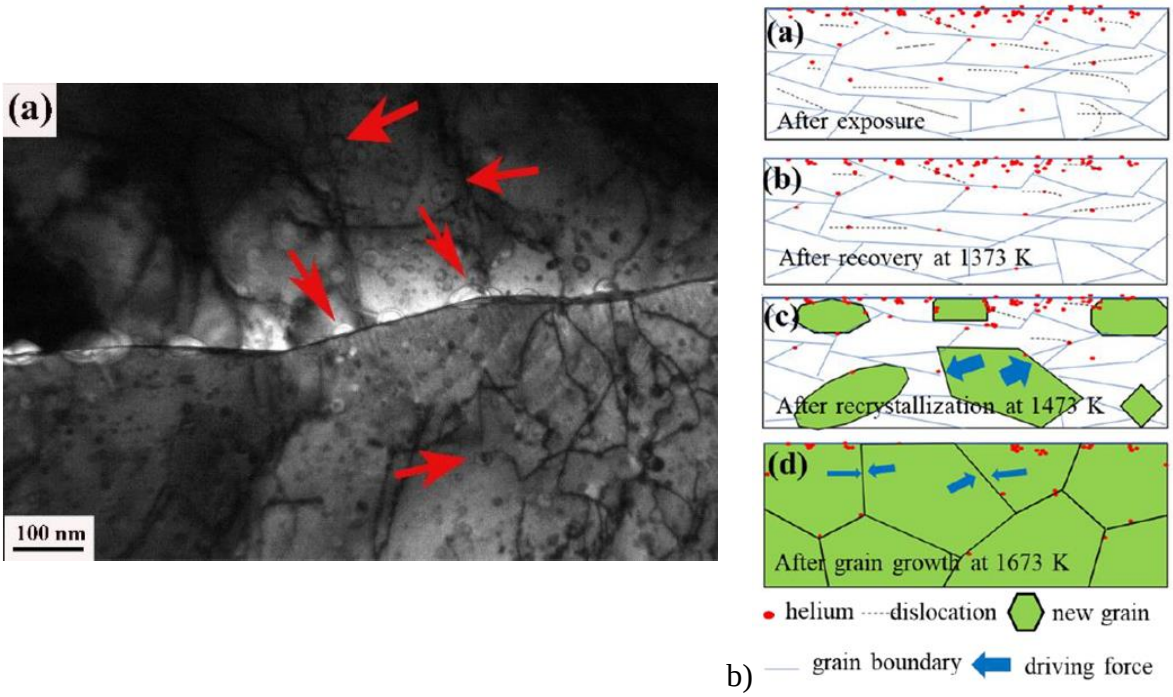

Figure 102. a) Trapped Helium bubbles in tungsten grain boundary and b) schematic of He as Zener pins mechanism proposal [36]

Because of this motivation, the initial work done was expected to find similar behavior, and concurrently explain the mechanisms that were retarding the onset of recrystallization, mainly a way to apply Zener solute drag relating to H concentration in the bulk. Solute atoms, in metallic matrixes tend to have a drag effect on the grain boundaries' mobility and thus impeding recrystallization. However, as the results started to appear, it was clear that the focus had to shift. As demonstrated throughout this thesis, another behavior for tungsten under plasma loading was encountered. The results presented show that, for the regimes tested Recrystallization was not slowed down, but actually enhanced.

This behavior was consistent on all 6 individually plasma exposed samples. Additionally, it was also thought at the beginning of this task that the pulsed plasma, may somehow be the cause of this enhanced recrystallization behavior. As the results show, the plasma pulses made no difference on the observed recrystallization behavior. This is likely to the high thermal dissipation of the samples because of the active water cooling. As demonstrated with the FEM analyses, these pulses barely changed the temperature 200 °C above the base temp on a sliver of ~0.2 – 0.3 mm below the surface. This FEM calculations, also permitted the characterization of the bulk of the sample by taking measurements in the cross-section, and the results were consistent among the 6 samples, as well as with the surface. Since all samples were cut from the same original bar of ITER grade tungsten, difference in the materials used was also ruled out as an explanation for this behavior. To be thorough though, two samples were annealed in a furnace at 1200 °C and 1000 °C, temperatures which were in the range and above the observed recrystallization. This results yielded recrystallization measurements consistent with literature data confirming that indeed the work was being done with the assumed material.

Logically, since the substantial difference between furnace annealed and hydrogen loaded samples was the hydrogen plasma, the penetration of the latter in the bulk should explain the recrystallization behavior. The TMAP7 simulations show that the hydrogen concentration at the operational temperatures and plasma flux were too high to permit any hydrogen from being captured by traps in the bulk and pinning the grain boundaries during recrystallization. Recalling equation 3.2, the drag force on the grain boundary is proportional to the concentration of hydrogen in the bulk (10^{-7}) and the force per pinning solute particle which is proportional to the particles diameter (hydrogen atoms with 25 picometers atomic radius). This last set of results rules out an effect of the H atoms being pinned on defects and affecting the grain boundary motion.

7.5 Alternative Hypothesis Proposals

Although contrary to most of the well-established theories of solute effects on recrystallization and grain growth, accelerated restoring kinetics in the presence of hydrogen are not unheard of. Recent research by Martin, et al. [56] show significantly increased grain growth kinetics of vanadium in the presence of a hydrogen atmosphere. During the course of this study, the presence of hydrogen increased the grain sizes after annealing threefold, compared to annealing in a vacuum. Vanadium being a bcc metal shares some of the same diffusion behaviors as tungsten, specifically for this case, the diffusion paths through interstitial sites.

According to the authors [56], the diffusion behavior of hydrogen must at least on some level act according to the established theories. Thus, the thermodynamic driving force coming from the reduction of grain boundary area has to be reduced by the excess hydrogen entering the grain boundary, leading to a reduction of the grain boundary energy. Since accelerated, instead of slowed grain growth was observed, it is proposed that the grain boundary mobility itself is increased by the hydrogen, and thus, in their words, “overcompensates” the reduction in the driving force. The proposed mechanism for this to occur is by hydrogen promoting the creation of grain boundary ledges, which are step-shaped defects in the grain boundary interface, that locally increase the mobility of the grain boundary (see Figure 103). The formation of steps necessitates of new grain boundary area, and so, the hydrogen may be lowering their formation energy by acting as a defect acting agent (defactant). Solute atoms act as defactants when they segregate to an area prone to defect formation, like a grain boundary, and locally decrease the defects formation energy of part of that region. This localized reduction in defect formation energy results in an overall free energy reduction of the whole neighborhood (i.e. grain boundary). Thus, even if hydrogen lessens the driving force for grain boundary motion according to traditional solute drag theories, the overall energy reduction increases the frequency of ledge formation, and thus an increased grain boundary mobility mechanism will dominate [56].

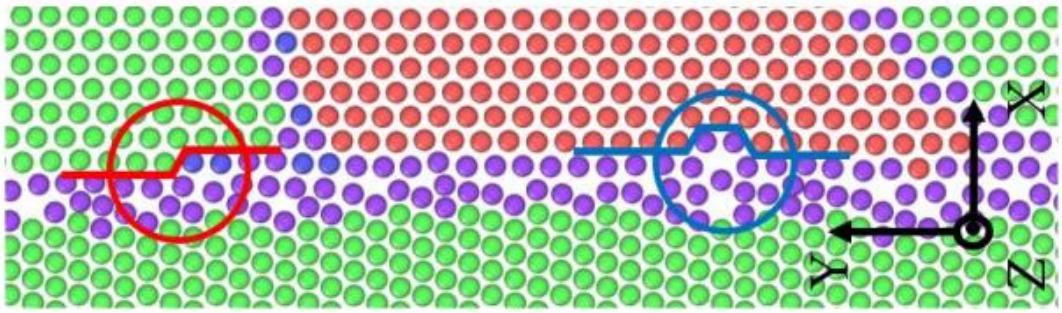

Figure 103. Examples of grain boundary ledges circled [57]

The process described above is similar to the nucleation of kink-pairs in dislocations, where they experience an enhanced dislocation mobility and overall material softening due to the presence of hydrogen [58]. Since ledges are small compared to the grain boundary, a lower concentration of hydrogen than that of the H atoms affecting the GB as a whole (i.e. Zener drag) would be needed for their formation. The "nucleation" of ledges along the grain boundary, increasing the mobility of the grain boundary as a whole, and thus accelerating the apparent self-diffusion rate, might be mechanism showing the increased recrystallization rate observed in the plasma exposed tungsten samples of this work. Hydrogen diffusion in bcc metals follows a similar trend regardless of the matrix element [50], and so it is reasonable to think that under certain conditions, it would have a similar effect on tungsten as the one seen in vanadium. If this is the case, this mechanism might explain the abnormal grain growth seen in sample W3. This is because, assuming that indeed there was loss of thermal contact as hypothesized in section 6.4.2, the hydrogen in this area of the bulk might have "lingered" longer than in the rest of the sample and thus the effect of the hydrogen on the grain boundaries would be higher.

Wirtz et al. [23] also noticed that tungsten samples loaded with plasma and then under electron beam showed increased crack growth compared to samples which were only subjected to equivalent e-beam loads. It was hypothesized that this was due to hydrogen trapped in the lattice inside vacancy clusters or dislocations during the plasma exposure distorted the lattice enough for stresses to build up and thus lower the effective stress for crack formation and propagation. This stressing of the lattice is supported by the fact that the hydrogen atom is ~30% bigger than the tetrahedral site it occupies during solution [59]. Cotterill [59] also found that tungsten shows signs of hydrogen embrittlement at room temperature during tensile testing of tungsten, vanadium, molybdenum and other bcc metals. They propose that the underlying mechanisms for this behavior involves the supersaturation of the lattice by the hydrogen atoms, which precipitate from interstitial solution into nearby voids (vacancies or other imperfections large enough to accommodate the solute atom) increasing the strain in the lattice. This localized accumulated strain is proposed to be the nucleation point of a cleavage fracture which then propagates in the material, and so being the cause of the embrittlement.

Adding to the above, Zhou et al. [60][61] investigated the effects of a hydrogen atom in a tungsten grain boundary using first-principles DFT calculations. In these studies, the grain boundary was simulated by a supercell with repeating boundary conditions and an inclusion of one hydrogen atom on its most stable tetrahedral site. The authors found that hydrogen tends to prefer segregating to grain boundaries, rather than staying in the bulk, and also calculated that a single hydrogen atom in a tilt grain boundary can reduce the GB's tensile strength and

its fracture energy by 9% and 4% respectively. This confirms the notion that hydrogen embrittles tungsten when it segregates to the grain boundaries. Liu et al. [62] complement this information, by providing molecular dynamics calculations of preferential vacancy formation induced by the presence of hydrogen atoms. Hydrogen induced vacancies seem to be formed by hydrogen atoms, driving W atoms from the lattice out of their crystal equilibrium positions, and clustering in stable hexagonal self-interstitial atom structures. These structures are stable enough that they are not annihilated in the matrix, so the vacancies left behind in the atoms' original positions are stable as well. These stable vacancies, if formed near grain boundaries or, if displaced to those locations, may be the origin of the accelerated ledge formation in the grain boundaries that promote accelerated recrystallization.

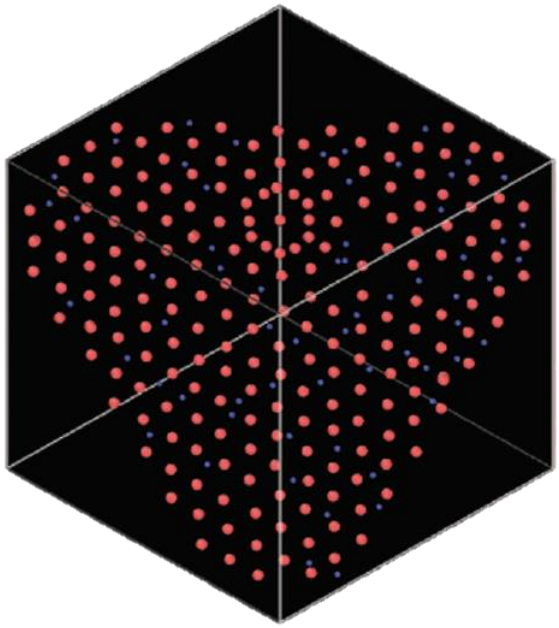

Figure 104. Calculated hydrogen induced hexagonal SIA structure in tungsten seen on (111) plane from [111] direction. [62]

The above studies point to the same type mechanism taking place: interstitially diffused hydrogen segregating to voids or grain boundaries, and modifying the behavior of the matrix nearby. Given that the mentioned effects are highly localized, the overall hydrogen concentration need not be exceedingly high for the phenomena described to have a macroscopic influence, say as embrittlement or recrystallization and grain growth. Moreover, with the available information, these effects may actually exist independently and complement each other. As grain boundaries move during the accelerated recrystallization, the material loses its strength which lowers the threshold for crack propagation. These same atoms may diffuse into the mentioned voids and strain the matrix enough for catastrophic failure to occur. Because of the above, this mechanism should be researched further, especially in the context of plasma loading, not only because of the ITER implications, but because hydrogen plasma exposure is an extreme enough version of hydrogen presence that may give the best yet picture of the behavior of interstitial hydrogen in tungsten, and gives insight to the general behavior in bcc metals.

7.6 Further Research

The analysis presented in this work, and the previous studies that prompted it, clearly show that the behavior of tungsten in the presence of hydrogen plasma is not fully understood. Recrystallization kinetics, especially, do not conform to the expected behavior consistent with solute drag. On the contrary, there is very little literature describing the accelerated recrystallization phenomena observed. Therefore, the main item to improve our understanding of this phenomenon is to gather a comprehensive dataset of tungsten under hydrogen plasma similar to the one obtained by Alfonso et al. [17]. The proposal put forward here is to take advantage of the Gaussian nature of the plasma beam to build a set of isothermal curves that would complement the 1 hour isochronal curves calculated in this project. By subjecting a series of water cooled samples to a hydrogen plasma exposure of ~1500 °C at the strike point, a range of temperatures from ~700 °C to the mentioned maximum can be obtained as shown in chapters 6 and 7 of this work. If these samples are separately subjected to different time interval exposures, (i.e. ½, 1, 2, 3, 4 and 5 hours) a robust family of isothermal and isochronal curves can be built. This also comes with the advantage of ideally setting the plasma source with the same parameters every time and thus be able to properly account for the hydrogen concentration via a controlled particle flux. In the earlier stages of this project, it was proposed to do a set of companion experiments at FZJ's JUDTIH II electron beam facility. By using the e-beam to recreate an equivalent surface temperature profile to the one from Magnum-PSI the results could be contrasted to isolate the effects of the hydrogen plasma. Although this plan was not able to be implemented during the duration of this work, this proposal should be reevaluated and rescheduled to complement and serve as control for the plasma exposed samples. If JUDTIH II can replicate the surface temperature diametral profile from the plasma exposures, a set of time interval exposures equivalent to the ones proposed for the plasma experiments above should be made.

The recrystallization analysis in this work was done primarily on the effects of recrystallization on the tungsten's hardness. Although this relationship is real, there exist more accurate ways to measure recrystallization like the grain orientation mapping and HAGB measurements that can be obtained with substantial EBSD measurements. During this thesis, unfortunately access to the needed EBSD microscopes was severely reduced from the intended availability due to factors out of our control. Nevertheless it would still be beneficial to complement this research's result with this type of measurements as they can provide more insight into the extent of nucleation and growth of the grain boundaries, as well as the motion of the grain boundaries and dislocations at the different stages of the recrystallization process. Also, as part of the original plan for this project, samples were going to be subjected to electron beam loading replicating the temperature profile from the plasma beam, but again, due to unforeseen circumstances this was not possible. This direct comparison would add to the current body of work on the study of tungsten recrystallization with no hydrogen presence which is not comprehensive, and may provide more insight into the effective recrystallization activation energy and how it changes with the presence of hydrogen.

Regarding the simulation of the concentration of hydrogen from the plasma, there is room to improve on the understanding of its behavior inside the bulk. Figure 101 in section 7 shows that there is a strong dependence on hydrogen trapping at low temperatures and at low solute concentrations. This falls in the regime where no recrystallization was observed during these experiments, but nonetheless, the samples were exposed partly to it, so according to the research, some hydrogen should have been trapped in these regions of the samples. More simulations should be run not only at the strike point but at points along the diameter where

recrystallization was less prevalent. This also raises the question of how is the 2D hydrogen diffusion behavior in non-uniform temperature regions might manifest itself, since the TMAP7 simulations treat the problem in a 1D manner. This can also help understand better the hydrogen flow in W3 where the heat flux was not uniform going from the top to the bottom of the sample.

Other mechanisms not directly relating to hydrogen being the root cause of the increased recrystallization rate and that might explain the observed phenomena should be also considered or at least be conclusively ruled out. For instance, Suslova et al. [63] propose that during laser beam loading the stress and thermal gradients might be high enough to induce dynamic recrystallization (recrystallization caused by deformation) in the tungsten. This process aides in arranging and accumulating dislocations into cells, which as the dislocations accumulate, increase the misorientation angle resulting in a recrystallized grain structure. Dynamic recrystallization habitually appears in scenarios of high strain rate which a priori is not the case for the Magnum-PSI experimental setup, but it cannot be ruled out without a proper analysis. Stress and strain field calculations due to the thermal load and experimental constraints should be performed on the samples from these and further experiments to understand if the stress and strain fields arising from the Gaussian plasma beam are high enough to indeed cause dynamic deformation in the material.

8. Summary and Conclusions

The effects of steady-state and transient hydrogen plasma loading on ITER grade deformed tungsten were the main research points of this investigation. The project centered on the surface thermal shock response of tungsten under simulated ELMs and the surface and bulk recrystallization behavior under plasma loading conditions. Six polished tungsten samples were subjected to a hydrogen plasma beam at DIFFER's Magnum-PSI with a Gaussian heat flux distribution that yielded temperatures at the strike point ranging from ~1000 to ~1500 °C. Three of these samples were subjected to high frequency (5 Hz) pulses that ranged from ~200 to ~300 °C. Of these six samples, five of them experienced plasma loading for one hour and one of them experienced plasma loading for four hours with no pulses. Of the remaining three samples, two were used as control during furnace annealing and one was used as a "dummy" to test the plasma beam parameters before the exposures proper.

The surface temperature was characterized by means of processing the signals from the IR camera, calibrating it with the spectro-pyrometer, and the plasma parameters striking the surface were collected by means of Thompson Scattering. Based on the collected surface data, the bulk temperature profiles (both in steady state and during pulsed transient regimes) of the samples were simulated using FEM to give a full portrayal of the behavior of the sample as a whole. Similarly simulations of the hydrogen concentration across the bulk due to the plasma were calculated using the collected Thompson Scattering data.

For the thermal shock response the diametral profile of the base and pulsed temperatures of the samples subjected to the pulses were characterized, as well as the power density deposited by the plasma pulses. These calculations were correlated with the damage morphologies identified on the targets and a damage map akin to those by Wirtz, Hirai, and Linke [23][24][42] was elaborated to compare the experimental results with the established body of knowledge. The effects of the plasma on the restoration kinetics were characterized mechanically by means of Vickers hardness measurements taken both on the samples' surface and through the cross-sectional bulk. These kinetics were modelled and compared to the expected recrystallization kinetics based on the work done by Alfonso et al. [17]. The conclusions from the discussion of this work are presented below.

Most of the research comprising the current body of work on the thermal response of tungsten under transient loads compromises a range of low temperatures (RT – 800 °C) and a wide range of power densities (200 – 1400 MW m^{-2}) with samples exposed under electron beam loading. This thesis studied a high temperature (500 °C – 1500 °C) and low power density (10 – 180 MW m^{-2}) regime. The damage map elaborated showed that the plasma loaded samples seemed to show a correlation between where the most severe damage (cracks and crack networks) occurs and the onset of the measured recrystallization temperature of the samples which was in principle, lower than expected.

This lower recrystallization temperature was determined by comparing the surface temperature measurements collected from the IR camera and the FEM bulk thermal maps to the micro hardness measurements taken from the surface and the bulk. These measurements showed that recrystallization could be identified to occur between ~960 °C and ~990 °C after one hour of plasma exposure and, for four hours of plasma exposure, full recrystallization took place at least ~700 °C. By modelling the recovery and recrystallization kinetics of the material based on the JMAK kinetics version put forward by Alfonso et al. [17] it was found that instead of the expected recrystallization activation energy of ~365 kJ mol^{-1} (calculated from furnace

annealed samples), after one hour plasma exposure the activation energy was found to be ~277 kJ mol^{-1} , and after four hours of plasma exposure the activation energy was reduced to at least ~212 kJ mol^{-1} which points to the presence of hydrogen actively reducing the activation energy for self-diffusion. This accelerated self-diffusion seems to occur at the grain boundaries as it intensely affects recrystallization and the calculated values after one hour seem to correlate better with reported literature data on grain boundary diffusion than with bulk diffusion, the latter being substantially higher. The furnace annealed samples on this work showed no signs of recrystallization and seem to agree with the initial proposed model. This model and the model proposed for accelerated recrystallization kinetics were both corroborated using the Meyer – Neldel isokinetic rule. These last points strengthen the claim that the presence of hydrogen from the plasma is indeed actively affecting the recrystallization behavior of the tungsten.

Hydrogen concentration simulations were ran using TMAP7 to determine the amount of hydrogen present in the material during exposure. These simulations were done at the point of maximum particle flux. The outcome was that hydrogen concentration, both mobile and trapped, was very low ($\sim 10^{-7}$) and that at the sites where recrystallization was identified, no hydrogen should be trapped in vacancies or grain boundaries due to the high temperatures. This point, combined with the rest of the collected data led to the rejection of the original project's hypothesis that trapped hydrogen would act as solute drag at the grain boundaries and slow the recrystallization process. Since the recrystallization was accelerated, other mechanisms that explain this behavior were put forward.

Accelerated grain growth kinetics in the presence of hydrogen have been recently observed in vanadium [56] where it is posed that the traditional drag effects of the hydrogen as a solute are overcompensated by the mobility of the grain boundaries increasing because of the hydrogen presence. This may happen through the hydrogen acting as a defactant and promoting the creation of grain boundary ledges, in the grain boundary interfaces resulting in an overall free energy reduction of the whole affected region. This localized defect formation would need a lower concentration of hydrogen than that needed for Zener drag, thus increasing the mobility of the grain boundary as a whole and accelerating the apparent self-diffusion rate. Wirtz et al. [23] and Cotterill [59] also proposed that hydrogen trapped in the lattice inside voids during the plasma exposure build up stress by deforming the lattice and would lower the effective stress for crack formation which would also be the cause for hydrogen embrittlement of tungsten. These assertions about embrittlement appear to be corroborated by the DFT simulations by Zhou et al. [60][61] where interstitially diffused hydrogen was simulated in a tungsten grain boundary, and the results showed that this arrangement reduces the grain boundary's tensile strength and fracture energy by 9% and 4% respectively.

Based on the results and analysis of this thesis, it is recommended that further research centers in gathering experimental data on the behavior of tungsten under hydrogen plasma. A full set of isothermal curves under equivalent plasma loading conditions would provide a more complete picture following this thesis's results, and would more consistently account for the effects of the hydrogen plasma. Additional and extensive EBSD measurements should also be taken to complement the collected data. This extended data set should be able to provide enough information to accurately describe the accelerating recrystallization kinetics due to the presence of hydrogen, and a forward model dependent on temperature, time and hydrogen concentration could be designed. Other mechanisms other than the ones proposed, such as the dynamic recrystallization proposed by Suslova et al. [63] should be also studied and either incorporated or ruled out.

The results presented in this document should raise questions regarding the expected lifespan of the ITER divertor. Previous research sets the divertor lifespan's lowest threshold for steady state operation at 800 – 900 °C at around 2 years before half of the recrystallization (defined as the component's recrystallization operational budget) has taken place.[17][64]. Given that there was at least one sample that in that temperature range that fully recrystallized after 4 hours of plasma exposure, and that for the samples that were exposed for 1 hour the recrystallization threshold was measured to be within 100 °C of that operation temperature, these estimates should be revised and more experimental data collected to properly assess the lifespan of the components. The experimental conditions during this thesis simulated ITER conditions as closely as possible, and based on the results, there is at least some mixed range of operational temperature, heat and particle flux that promote undesired accelerated recrystallization. Failing to address these concerns may result in premature failure of the components during operation.

Although peculiar, the identified accelerated recrystallization behavior observed during the course of these experiments is by no means unique as demonstrated by Martin, et al. [56]. More research into understanding these mechanisms will provide a safer framework for the continuous development of fusion reactors and their components. Traditional models of material behavior (i.e. hydrogen acts as solute drag in bcc metals) may fail to describe the outcomes of the complex interactions that arise when subjecting the divertor's material to the plasma, which should be taken as an opportunity to expand the understanding of the field of plasma material interactions. The bulk of this work describes such an atypical behavior reflected in enhanced recrystallization, but there is still much room to improve in proposing and verifying a robust model that can explain and predict the observed phenomenon. Ideally this will help provide a more detailed description of reliable operational parameters for the ITER divertor, and offer enough perspective to plan and design around this type of contingency.

As the ITER reactor comes to completion, the scientific and engineering challenges regarding the successful implementation of fusion as a viable energy source need to be overcome. The extreme conditions inside the reactor have led to new understanding on the science and behavior of the selected materials for the project, with the tungsten of the divertor being no exception. The results of this work should complement the current body of literature on which it was built upon with the aim of robustly identifying the different regimes of operation and material behavior. As this understanding matures, and all the scientific and engineering hurdles are progressively overcome, the goal of a world were nuclear fusion can sustainably provide for our energy needs comes closer to be a reality.

References

[1] G. Pintsuk and T. Loewenhoff, “Impact of microstructure on the plasma performance of industrial and high-end tungsten grades,” *J. Nucl. Mater.*, vol. 438, no. SUPPL, pp. S945–S948, 2013.

[2] M. Kikuchi, K. Lackner, and M. Quang, “Fusion Physics,” *Iaea*, pp. 24–26, 2012.

[3] G. Nicoletti, N. Arcuri, G. Nicoletti, and R. Bruno, “A technical and environmental comparison between hydrogen and some fossil fuels,” vol. 89, pp. 205–213, 2015.

[4] EIA, “International Energy Outlook 2017 Overview,” 2017.

[5] J. D. Jenkins and S. Thernstrom, “DEEP DECARBONIZATION OF THE ELECTRIC POWER SECTOR INSIGHTS FROM RECENT LITERATURE,” no. March, 2017.

[6] ITER Organization, “What is ITER?,” *ITER*. [Online]. Available: https://www.iter.org/proj/inafewlines. [Accessed: 31-Oct-2017].

[7] IAEA, “ITER Final Design Report,” *ITER Doc. Ser. No 22*, vol. 4, p. 88, 2001.

[8] K. Miyamoto, *Plasma Physics and Controlled Nuclear Fusion*. Springer, 2004.

[9] A. J. Garrido *et al.*, “Linear models for plasma current control in tokamak reactors,” *11th Int. Conf. Control. Autom. Robot. Vision, ICARCV 2010*, no. May 2014, pp. 78–84, 2010.

[10] V. Barabash *et al.*, “Materials challenges for ITER - Current status and future activities,” *J. Nucl. Mater.*, vol. 367–370 A, no. SPEC. ISS., pp. 21–32, 2007.

[11] H. J. N. Van Eck *et al.*, “Divertor conditions relevant for fusion reactors achieved with linear plasma generator,” *Appl. Phys. Lett.*, vol. 101, no. 22, 2012.

[12] P. Majerus, “The new electron beam test facility JUDITH II for high heat flux experiments on plasma facing components.” Elsevier, Julich, Germany, 2005.

[13] G. Van Rooij, N. L. Cardozo, and H. De Blank, *Fusion reactors : extreme materials , intense plasma-wall interaction*. TU/e Fusion, 2016.

[14] Steven J. Zinkle, “Challenges in Developing Materials for Fusion Technology - Past, Present and Future,” *Fusion Sci. Technol.*, vol. 64, no. 2, pp. 65–75, 2013.

[15] J. Wesson and D. J. Campbell, *Tokamaks*. Oxford: OUP Oxford, 2011.

[16] G. Pintsuk, *Tungsten as a plasma-facing material*, vol. 4. Elsevier Inc., 2012.

[17] A. Lopez, J. Jensen, D. Version, A. Lopez, and J. Jensen, “Thermal stability of warm-rolled tungsten,” 2015.

[18] V. A. Makhlai *et al.*, “Damaging of tungsten and tungsten – tantalum alloy exposed in ITER ELM-like conditions,” vol. 9, pp. 116–122, 2016.

[19] F. J. Humphreys and M. Hatherly, *Recrystallization and Related Annealing Phenomena*, 2nd ed. 2004.

[20] W. Callister and D. Rethwisch, *Materials science and engineering: an introduction*, vol. 94. 2007.

[21] D. Raabe, “Recovery and Recrystallization: Phenomena, Physics, Models, Simulation,” in *Physical Metallurgy*, Dusseldorf, DE: Elsevier B.V., 2014, p. 107.

[22] G. Gottstein, *Grain boundary migration in Metals*, vol. 31, no. C. 2010.

[23] O. M. Wirtz, “Thermal Shock Behaviour of Different Tungsten Grades under Varying Conditions,” p. 130, 2013.

[24] T. Hirai, G. Pintsuk, J. Linke, and M. Batilliot, “Cracking failure study of ITER-reference tungsten grade under single pulse thermal shock loads at elevated temperatures,” *J. Nucl. Mater.*, vol. 390–391, no. 1, pp. 751–754, 2009.

[25] M. Janssen, “Mechanical Behaviour of Materials at High Temperature.” p. 77, 2017.

[26] M. Li and J. H. You, “Interpretation of the deep cracking phenomenon of tungsten monoblock targets observed in high-heat-flux fatigue tests at 20 MW/m2,” *Fusion Eng. Des.*, vol. 101, no. 633053, pp. 1–8, 2015.

[27] G.-N. L. Xiang-Shan Kong, Sheng Wang, Xuebang Wu, Yu-Wei You, C.S. Liu, Q.F. Fang, Ling Chenb, "First-principles calculations of hydrogen solution and diffusion in tungsten: Temperature and defect-trapping effects," *Acta Mater.*, vol. 84, pp. 426–435, 2015.
[28] K. Heinola and T. Ahlgren, "Diffusion of hydrogen in bcc tungsten studied with first principle calculations," *J. Appl. Phys.*, vol. 107, no. 11, 2010.
[29] N. Fernandez, Y. Ferro, and D. Kato, "Hydrogen diffusion and vacancies formation in tungsten: Density Functional Theory calculations and statistical models," *Acta Mater.*, vol. 94, pp. 307–318, 2015.
[30] M. Hendrika, "Deuterium retention in radiation damaged tungsten exposed to high-flux plasmas door," 2014.
[31] F. Sefta, "Surface Response of Tungsten to Helium and Hydrogen Plasma Flux as a Function of Temperature and Incident Kinetic Energy," *J. Chem. Inf. Model.*, vol. 53, p. 160, 1989.
[32] M. S. David Porter, Kenneth Eastrling, *Phase Transformations in Metals*. 2009.
[33] J. Roth, K. Schmid, R. A. Causey, and T. J. Venhaus, "The Use of T ungsten in Fusion Reactors : A Review of the Hydrogen Retention and Migration Properties," 2001.
[34] J. Roth and K. Schmid, "Hydrogen in Tungsten as Plasma-facing Material Abstract :," *Phys. Scr.*, 2011.
[35] T. Loewenhoff *et al.*, "Impact of combined transient plasma/heat loads on tungsten performance below and above recrystallization temperature," *Nucl. Fusion*, vol. 55, no. 12, p. 123004, 2015.
[36] L. Cheng, W. Guo, G. De Temmerman, Y. Yuan, and G. Lu, "Retarded Recrystallization of Helium-exposed Tungsten," in *25th ITPA meeting on SOL/divertor physics*, 2018.
[37] S. Bardin, T. W. Morgan, X. Glad, R. A. Pitts, and G. De Temmerman, "Evolution of transiently melt damaged tungsten under ITER-relevant divertor plasma heat loading," *J. Nucl. Mater.*, vol. 463, pp. 193–197, 2015.
[38] G. G. Van Eden *et al.*, "The effect of high-flux H plasma exposure with simultaneous transient heat loads on tungsten surface damage and power handling," *Nucl. Fusion*, vol. 54, no. 12, 2014.
[39] Plasee SE, "Werkszeugnis M210.pdf." 2014.
[40] T. Loewenhoff, "Plansee pure tungsten according to ITER specifications ("IGP")," in *Plansee pure tungsten according to ITER specifications ("IGP")*, 2017.
[41] ITER Organization, "Materials Design Limit Data Handbook." 2013.
[42] J. Linke, "Performance of different tungsten grades under transient thermal loads," 2011.
[43] J. H. Yu *et al.*, "The effect of transient temporal pulse shape on surface temperature and tungsten damage," 2015.
[44] K. Schmid, J. Bauer, S. Markelj, U. Toussaint, A. Manhard, and W. Jacob, "Recent progress in the understanding of H transport and trapping in W," *Phys. Scr.*, vol. T170, no. 1, p. 14037, 2017.
[45] A. Farzadi, "Modeling of isothermal recovery and recrystallization kinetics by means of hardness measurements," no. 12, pp. 1218–1226, 2015.
[46] L. S. E. A. A. Cabral, "Determining the Kinetic Parameters for Isothermal Crystallization in a Lithium Disilicate (Ls 2) Glass by OM and DSC," vol. 162, no. 33268, pp. 157–162, 2014.
[47] A. M. Trump, "Recrystallization and Grain Growth Kinetics in Binary Alpha Titanium-Aluminum Alloys," University of Michigan, 2017.
[48] F. Liu, F. Sommer, C. Bos, and E. J. Mittemeijer, "Analysis of solid state phase

transformation kinetics : models and recipes," vol. 52, no. 4, pp. 193–212, 2007.
[49] L. BŁAZ and P. KWAPISINSKI, "SIMPLE MATEMATICAL MODEL FOR PREDICTION OF RECRYSTALLIZATION IN COPPER," *Arch. Metall. Mater.*, vol. 54, no. I, 2009.
[50] A. Jones, "Compensation of the Meyer-Neldel Compensation Law for H diffusion in minerals," *Geochem. Geophys. Geosyst.*, vol. 15, pp. 2616–2631, 2014.
[51] G. Boisvert, L. J. Lewis, and A. Yelon, "Many-Body Nature of the Meyer-Neldel Compensation Law for Diffusion," vol. 75, no. 3, 1995.
[52] M. Li *et al.*, "A molecular dynamics study of melting and dissociation of tungsten nanoparticles," vol. 127131, 2015.
[53] E. Lassner and W. Schubert, *Tungsten: Properties, Chemistry, Technology of the Element, Alloys, and Chemical Compounds*. Vienna, Austria: Kluwer Academic / Plenum Publishers, 1997.
[54] M. Riihleb, O. Gmbh, M. Weg, M. Planck, and I. Werkstoffwissenschaft, "Grain Growth Phenomena in Tungsten Wire," vol. 15, pp. 295–300, 1997.
[55] C. H. J. S. Lee, C. Minkwitz, "Grain Boundary Self-Diffusion in Polycrystalline Tungsten at Low Temperatures," *phys. stat. sol.*, vol. 202, 1997.
[56] M. L. Martin, A. Pundt, and R. Kirchheim, "Hydrogen-induced accelerated grain growth in vanadium," *Acta Mater.*, vol. 155, pp. 262–267, 2018.
[57] V. Turlo and T. J. Rupert, "Grain boundary complexions and the strength of nanocrystalline metals : Dislocation emission and propagation," pp. 1–36, 2017.
[58] M. Deutges, H. P. Barth, Y. Chen, and R. Kirchheim, "Hydrogen diffusivities as a measure of relative dislocation densities in palladium and increase of the density by plastic deformation in the presence of dissolved hydrogen," *Acta Mater.*, vol. 82, pp. 266–274, 2015.
[59] P. Cotterill, "THE HYDROGEN EMBRITTLEMENT OF METALS," *Prog. Mater. Sci.*, vol. 9, no. 4, pp. 205–250, 1961.
[60] H. Zhou, Y.-L. Liu, S. Jin, and Y. Zhang, "Investigating behaviours of hydrogen in a tungsten grain boundary by first principles : from dissolution and diffusion," *Nucl. Fusion*, vol. 25016, 2009.
[61] H. Zhou, S. Jin, Y. Zhang, and G. Lu, "Effects of hydrogen on a tungsten grain boundary : A first-principles computational tensile test," *Prog. Nat. Sci. Mater. Int.*, vol. 21, no. 3, pp. 240–245, 2011.
[62] Y. Liu *et al.*, "Mechanism of vacancy formation induced by hydrogen in tungsten," vol. 122111, 2013.
[63] A. Suslova, D. Sagapuram, S. S. Harilal, and A. Hassanein, "Recrystallization and grain growth induced by ELMs-like transient heat loads in deformed tungsten samples," pp. 1–11, 2014.
[64] G. De Temmerman, T. Hirai, and R. A. Pitts, "The influence of plasma-surface interaction on the The in fl uence of plasma-surface interaction on the performance of tungsten at the ITER divertor vertical targets," 2018.